

# Monitoring and Assessment of Geomagnetically Induced Currents in Alberta's High Voltage Network

by

Hannah Parry

A thesis submitted in partial fulfillment of the requirements for the degree of

Master of Science

Department of Physics

University of Alberta

© Hannah Parry, 2022

# Abstract

Geoelectric fields produced by time-varying magnetic fields associated with geomagnetic storms can result in potentially damaging geomagnetically induced currents (GICs) in long conductors at Earth's surface. GICs are quasi-direct currents which have been demonstrated to pose a significant risk to the integrity of grounded electrical infrastructure, particularly to transformers in the electrical power grid. In this study, an inferred GIC is calculated using a novel configuration of the differential magnetometer measurement (DMM) method on a 500 kV transmission line in central Alberta and is validated using a traditional neutral-to-ground current measurement at a transformer substation near Edmonton, Alberta. This thesis outlines a custom-built and innovative DMM design by which both DMM sensors deployed around a power line measure the background geomagnetic disturbance (GMD) and the magnetic field generated by the GIC. This approach provides two independent calculations of GIC which are compared against the transformer neutral current measured by AltaLink L.P, one of Alberta's largest utility companies. A developing partnership between the University of Alberta and companies within Alberta's power industry is leveraged to validate the augmented DMM method by directly comparing the two independent DMM inferred GIC measurements to the industry GIC measurement recorded using a Hall effect sensor. Results from a moderate geomagnetic storm on October 12th, 2021 show excellent temporal correspondence and contemporaneous peaks in both GIC measurements at 6:42:49 UT and 10:54:21 UT. This exercise was successful in demonstrating

a prototype for temporary deployment of the new DMM method to measure local GIC on the electrical power grid for use by industry.

Further, we examine the role of the Earth’s conductivity structure in driving GIC as described by the local impedance tensor. The geoelectric field is calculated through a convolution between the measured frequency-dependent impedance tensor and the magnetic field measured by the CARISMA (Canadian Array for Real-time Investigations of Magnetic Activity) magnetometer at Ministik Lake, 33 km from the transformer substation. A comparative analysis demonstrates excellent linear correlation between the calculated geoelectric field and the GIC response measured by AltaLink for three GMD events during the past year, particularly during a moderate geomagnetic storm on November 4th, 2021,  $R > 0.7$  from 2:00 to 8:00 UT. We demonstrate that the estimated geoelectric field is associated with the observed neutral-to-ground current, confirming that the GIC is driven in the electrical power network in Alberta by small and moderate GMD events. These results also prove an accurate measurement of the impedance can be utilized to diagnose the waveform of the geoelectric fields in central Alberta which are in good agreement with the GIC response in the power network. In the future, continued collaboration with industry partners will be leveraged to further examine the grid response in other segments of the Alberta electrical power grid, investigate the regional variability of the geoelectric field due to Earth’s conductivity structure and its impact on the power grid GIC response, and provide a comprehensive assessment and model for the whole of the Alberta electrical transmission system.

# Preface

The research in this thesis was conducted by the author.

Chapter 4 describes the validation of a new approach to a remote monitoring technique of GICs using transformer neutral-to-ground data provided by AltaLink. This chapter is currently being prepared for publication.

Chapter 5 also presents data collected by AltaLink during recent geomagnetic events for use in a comparative analysis between the power line GIC and the geoelectric field. Impedance tensor data was provided by Professor Martyn Unsworth and Darcy Cordell. Darcy Cordell wrote the code used to determine the geoelectric field and provided figure contributions on the 3-D surface impedance in Alberta, Canada (Figure 5.3).

Ian Mann supervised the whole of this research.

*To my Bamps*

# Acknowledgements

Foremost, I want to thank my supervisor, Prof. Ian Mann for his enthusiasm, encouragement and guidance through my research. I also extend my gratitude to members of my supervisory committee, Martyn Unsworth and Richard Sydora, for their feedback and support.

I sincerely thank David Milling and Andy Kale for their time and invaluable contribution to this project without whom the success of the research would not have been possible. I also acknowledge the loan of spare CARISMA equipment used during field deployment of our DMM system.

Thank you to Prof. Martyn Unsworth and Darcy Cordell for providing MT data and helping me understand the scientific principles of MT surveys.

Thank you to Colin Clark and others at AltaLink for providing data and knowledge about electrical transmission systems in Alberta. I am also thankful to Mark Hoover and others at ATCO Electric for the enlightening discussions and to Robert Baker for sharing his expertise on the electrical power industry in the province and beyond.

A special thank you is extended to Kurtis Fleet for allowing us to deploy our DMM system and take data on his property.

Many thanks to my family and friends for their ongoing support and patience. Finally, I thank Sebastian for always bringing me laughter and love when I need it most.

# Table of Contents

<b>1</b>	<b>Introduction</b>	<b>1</b>
1.1	Thesis Overview . . . . .	1
1.2	Space Weather . . . . .	3
1.2.1	The Sun . . . . .	4
1.2.2	Earth’s Magnetic Environment . . . . .	8
1.3	Induced Geoelectric Field . . . . .	14
1.3.1	A Simple Geoelectric Field Model . . . . .	16
1.3.2	Magnetotelluric Method . . . . .	18
<b>2</b>	<b>Geomagnetically Induced Currents</b>	<b>20</b>
2.1	Effects of GIC in Power Systems . . . . .	21
2.2	Examples of Historical GIC Events and Outcomes . . . . .	23
2.3	Measuring GIC . . . . .	25
2.3.1	Differential Magnetometer Measurement . . . . .	26
<b>3</b>	<b>Instrumentation of Differential Magnetometer Method</b>	<b>28</b>
3.1	Benefits of the Augmented DMM Method . . . . .	28
3.2	Development of a Novel DMM Approach . . . . .	30
3.3	Deriving GIC from the New DMM Method . . . . .	31
3.4	Instrumentation, Deployment, and Operation . . . . .	34
3.4.1	DMM Equipment and Design . . . . .	34
3.4.2	Deployment and Operation . . . . .	36
3.4.3	Uncertainties in DMM Derived GIC . . . . .	38
3.5	Upgrades for Future Deployments . . . . .	41
3.6	Summary . . . . .	42
<b>4</b>	<b>Validating the Novel DMM Approach for GIC Analysis on Alberta’s High Voltage Network</b>	<b>44</b>
4.1	Introduction . . . . .	44
4.2	Data and Methodology . . . . .	46
4.3	Results . . . . .	48
4.3.1	Geomagnetically Quiet Day . . . . .	48
4.3.2	DMM Inferred GIC: October 12th, 2021 . . . . .	50
4.4	Discussion and Conclusions . . . . .	60
<b>5</b>	<b>Direct Comparisons Between an Estimated Geoelectric Field and the Power Grid Response during Recent Geomagnetic Events</b>	<b>65</b>
5.1	Introduction . . . . .	65
5.2	Data and Methodology . . . . .	68
5.3	Results and Discussion . . . . .	71
5.3.1	Spatial and Frequency Dependence of MT Transfer Functions . . . . .	71

5.3.2	Derived Geoelectric Field Comparison to GIC . . . . .	78
5.3.3	Linear Correlation Comparison Between Geoelectric Field and GIC . . . . .	82
5.4	Conclusions . . . . .	84
<b>6</b>	<b>Conclusions and Future Work</b>	<b>88</b>
6.1	Summary and Conclusions . . . . .	88
6.2	Future Work with Industry Partners . . . . .	91
	<b>Bibliography</b>	<b>93</b>

# List of Figures

1.1	Flowchart of the space weather chain . . . . .	4
1.2	Parker spiral . . . . .	6
1.3	An example of solar activity associated with a sunspot on October 9th, 2021 . . . . .	7
1.4	The solar cycle . . . . .	7
1.5	Schematic of the Earth’s magnetosphere . . . . .	10
1.6	Ionospheric current systems at high altitude . . . . .	12
1.7	Schematic of GIC flowing through a power line . . . . .	15
1.8	Schematic of geoelectric field induction in a loop . . . . .	17
3.1	Schematic of DMM deployment . . . . .	30
3.2	An image of the deployed DMM equipment . . . . .	36
3.3	Top view of the secured fluxgate magnetometer . . . . .	36
3.4	A map of Edmonton and the surrounding area shows the locations of major power lines, the DMM deployment and the MSTK CARISMA station . . . . .	38
3.5	Images of the magnetometer setup deployed near a 500 kV power line . . . . .	39
4.1	Magnetic field on September 26th, 2021 . . . . .	49
4.2	DMM on September 26th, 2021 . . . . .	51
4.3	Magnetic field on October 12th, 2021 . . . . .	52
4.4	DMM on Oct 12th, 2021 . . . . .	54
4.5	Neutral-to-ground current measured on each circuit . . . . .	55
4.6	DMM inferred GIC and transformer neutral-to-ground current on Oct 12th, 2012 . . . . .	56
4.7	Direct comparison between the DMM inferred GIC and the transformer neutral-to-ground current . . . . .	58
4.8	Background magnetic field measured by DMM method . . . . .	60
5.1	Map of the major power lines around Edmonton and surrounding areas . . . . .	72
5.2	Map of transfer-function amplitude across the continental United States at two discrete periods: 120 s and 1200 s. . . . .	73
5.3	Map of transfer-function amplitude across Alberta at two discrete periods: 130 s and 1300 s. . . . .	75
5.4	Frequency dependent 3-D surface impedance in each real and imaginary tensor component . . . . .	76
5.5	$B(\omega)$ and the calculated $E(\omega)$ in the frequency band $10^{-4}$ to $10^{-1}$ Hz. . . . .	77
5.6	Comparison between geoelectric field and the transformer neutral-to-ground current on October 12th, 2021 . . . . .	79
5.7	Comparison between geoelectric field and the transformer neutral-to-ground current on November 4th, 2021 . . . . .	80

5.8	Comparison between geoelectric field and the transformer neutral-to-ground current on February 3rd, 2022 . . . . .	80
5.9	Linear correlation between geoelectric field and the neutral current on November 4th, 2021 in two hour intervals . . . . .	83

# Chapter 1

## Introduction

### 1.1 Thesis Overview

The continuous and growing reliance on electricity generation and distribution for basic health and safety requirements and economic development and success, exposes society to risks associated with any damage or interruption to electricity supply. A number of hazards in this regard can be electromagnetic events including lightning (e.g., *Chisholm*, 2018), electromagnetic pulses (e.g., *Wang et al.*, 2019), and space weather (e.g., *Kappenman*, 2012; *Molinski*, 2002; *Boteler*, 2001; *Boteler et al.*, 1998). Space weather events in particular have the potential to also damage satellites, disrupt radio communications and Global Navigation Satellite Systems (GNSS), but the threat to electricity distribution by driving geomagnetic induced currents (GICs) is considered the most threatening and impactful (e.g., *Molinski*, 2002; *Rajput et al.*, 2021, and references therein).

GICs caused by geomagnetic disturbances (GMD) are quasi-direct currents induced in power systems between grounding points in the network. GICs are a constant threat to the integrity of electrical infrastructure and can result in transformer damage and misoperation leading to voltage collapse and, in the most extreme cases, electrical blackouts. This thesis outlines and validates a measurement of GIC on the Alberta power network using a new

and novel, custom-built differential magnetometer measurement (DMM) technique to characterize the GIC flow through a segment of the power grid. We also studied the relationship between the driving geoelectric field and the responding GIC measured at the neutral-to-ground connection at a transformer substation within the Alberta electrical distribution system. The following sections in this chapter present an overview of space weather as a driver of GIC, and provide essential background and review of the solar-terrestrial connection, geomagnetic environment, and the induction of geoelectric fields in the conductive Earth. The thesis is then organized as follows.

Chapter 2 presents background on the resulting GIC phenomena and the effects of GIC on power systems and power system technologies including transformers. An introduction to GIC measurement methods, including the DMM method is provided.

Chapter 3 outlines the instrumentation, design and set up of our custom DMM system and its deployment strategy in a temporary campaign in the summer and fall of 2021. Specifically, a discussion is provided on how we addressed issues raised by previous DMM studies and approaches (e.g., *Hübner et al.*, 2020; *Matandirotya et al.*, 2016), particularly the unexpected difference of inferred GIC magnitudes as compared to neutral-to-ground currents measured by the power transmission industry. Upgrades to the design of the DMM system in a future field deployment is also discussed.

Chapter 4 analyzes data which validates the new DMM method and demonstrates a simple, cost-effective, remote, and completely non-invasive technique to measure and characterize the GIC flowing through power lines in central Alberta's high voltage electrical network using data from a GMD event on October 12th, 2021. The DMM inferred GIC is validated against transformer neutral-to-ground data measured by a Hall effect current sensor deployed by AltaLink at a nearby transformer substation and the end of the power line seg-

ment. A comparison of the background GMD derived from the DMM method is compared to the magnetic field measured by a magnetometer from the Canadian Array for Real time Investigations of Magnetic Activity (CARISMA; *Mann et al.*, 2008)) at Ministik lake (MSTK) station.

Chapter 5 presents a direct comparison of measured GIC in the form of the neutral-to-ground current at the transformer substation and the calculated geoelectric field. We examine the hypothesis that the magnetotelluric (MT) impedance, defined as an impedance tensor which characterizes the ground conductivity structure using MT measurements, could be dominant in estimates of the inductive geoelectric fields responsible driving GIC under the action of GMD.

Finally, Chapter 6 summarizes the thesis and discusses the impacts of the results discussed in previous chapters in the context of future assessments of GIC and their impacts on the power grid in Alberta. Plans for future work involving close industry collaboration is also outlined.

## 1.2 Space Weather

Space weather refers to the variable physical conditions of the interplanetary magnetic field (IMF) and the solar-terrestrial connection, which encompasses the state of the magnetic environment of Earth - including the magnetosphere and ionosphere - in response to solar forcing. The solar-terrestrial connection is an essential element for understanding the processes which produce GIC and cause subsequent potential damage to electrical power distribution infrastructure, particularly transformers. The physical processes responsible for generating GIC, illustrated in Figure 1.1, begins at the sun when high-energy particles are expelled in the form of solar wind or during coronal mass ejections (CMEs). If directed toward Earth, the energetic particles transported by the solar wind will interact with and cause fast changes in the Earth's magnetic

field, inducing electric fields in the near-Earth space and in the Earth's crust and ultimately driving currents through a grounded conductive infrastructure in an electric power network. This is particularly dangerous for reliable power grid operation. The remainder of this chapter will provide an overview of the progression of events that lead to GIC, often described as the space weather chain.

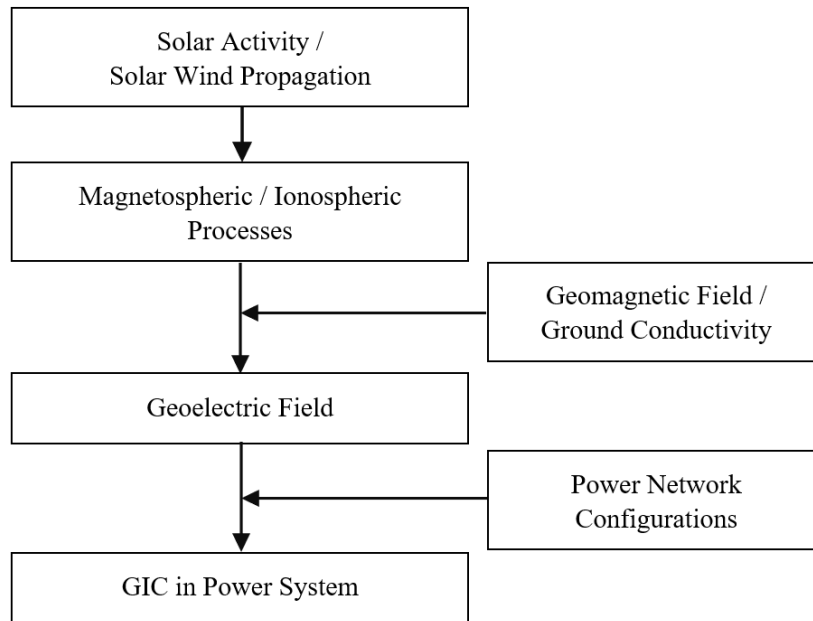


Figure 1.1: Chain of events leading to GIC in an electrical power system (adapted from *Pirjola (2000)*).

### 1.2.1 The Sun

The sun is a main-sequence star in the middle of our solar system responsible for producing the energy required for life on Earth; however, it is also the starting point of the space weather chain which describes the processes leading to potential space weather hazards like GIC.

## Solar Wind

The solar wind, first described by *Parker* (1959), is the continuous stream of plasma emitted from the sun. Mostly composed of electrons and protons, the expanding plasma is ejected from the sun's atmosphere since the thermal energy and pressure allow the particles to escape the gravitational potential of the sun. Due to solar variability, the solar wind velocity in near-Earth space can reach speeds between the order of 300-1500 km/sec. The high conductivity of the plasma, the hot ionized gas in the solar wind, traps the solar magnetic field into the solar wind which arises from the frozen-in magnetic field condition (e.g., *Kivelson and Russell*, 1995). This requires that the particles existing on a field line will remain on the the same field line as the solar material is carried radially outward in the heliospace towards the near-Earth space environment (*Campbell*, 2018). The magnetic structure in the solar wind is known as the interplanetary magnetic field (IMF). Due to the rotation of the sun, approximately a 27 day period, and the frozen-in magnetic flux condition, the ambient IMF is dragged to form a large scale Archimedean spiral, as seen in Figure 1.2. The structure of the ambient IMF is also disrupted by solar eruptions. Extremes in the solar wind speed are sporadic, only occurring during solar eruption events, including CMEs or during intervals of magnetic connectivity to the poles of the sun (e.g., *Baumjohann and Treumann*, 2012).

## Solar Cycle

The magnetically dynamic sun follows an approximate 11 year cycle of activity which can be measured by the observed number of sunspots. In the photosphere, the visible surface of the sun, sunspots appear as dark regions resulting from strong magnetic flux emerging from the solar interior and inhibiting convection thereby reducing temperatures relative to the surrounding areas (e.g., *Parker*, 1979). The intense magnetic fields associated with groups

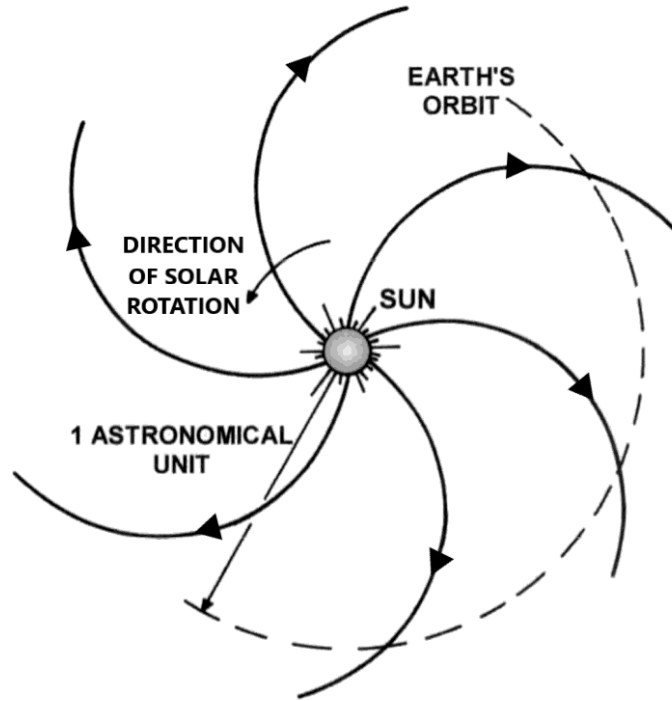


Figure 1.2: A schematic representation of the Parker spiral structure of the magnetic field in the solar wind. The Parker spiral describes the radially emitted solar wind which carries the embedded solar magnetic field into the solar system. The spiral formation is a consequence of the rotation of the sun (adapted from *Bittencourt* (2004)).

of sunspot and solar active regions are the source of solar flares and CMEs. An example of the release of an Earth-directed CME captured by the Solar Dynamic Observatory (SDO) and the Large Angle and Spectrometric Coronagraph (LASCO) on the Solar and Heliospheric Observatory (SOHO) satellite is shown in Figure 1.3.

Currently in 2022, we are approaching a solar maximum expected to peak in 2025 (see Figure 1.4). The number of sunspots is currently increasing, and thus we can anticipate the frequency of CMEs with the potential to cause active space weather at the Earth in the form of geomagnetic storms will increase. It is important to note that sunspot number is not a direct metric for determining the short-term likelihood of a geomagnetic storm event despite

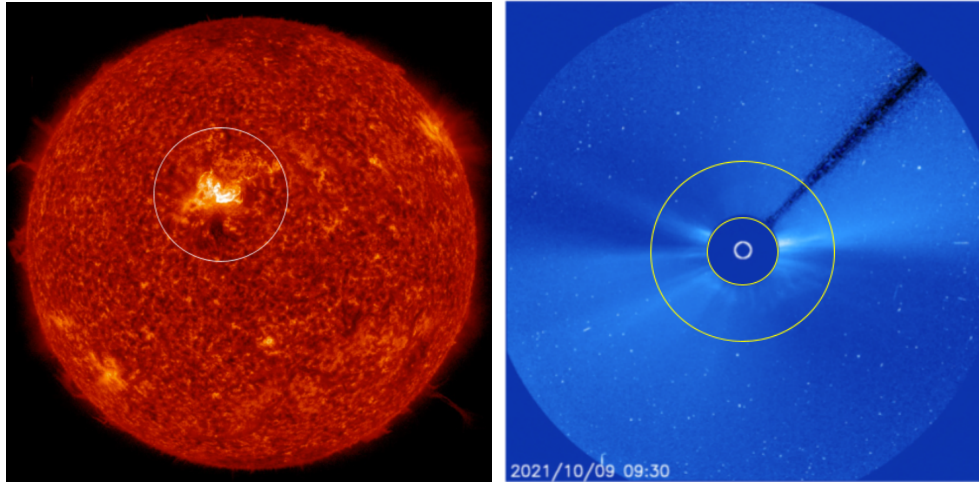


Figure 1.3: a) An (304 Å) image captured by SDO on Oct 9th, 2021 shows an active region which brightened, associated with a solar flare and CME. b) Outlined in yellow, the “Halo CME” ejected from this region was captured by the LASCO instrument on the SOHO satellite on Oct 9th, 2021. (Images retrieved from SpaceWeather.com)

the fact that, on the timescale of the solar cycle, the sunspot number traces the level of the solar activity. Individual bursts of geomagnetic activity are caused by episodic CMEs which remain challenging to predict. The impact on power systems necessitates robust systems for measuring and monitoring the GMDs in response to individual magnetic storms.

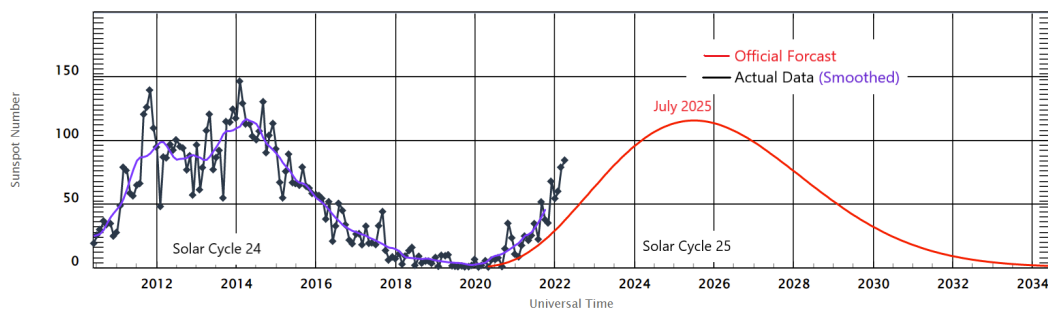


Figure 1.4: Predicted versus observed sunspot number shows we are currently approaching a solar maximum predicted to peak in 2025. (Retrieved from [www.swpc.noaa.gov/products/solar-cycle-progression](http://www.swpc.noaa.gov/products/solar-cycle-progression) on May 4th, 2022 )

## 1.2.2 Earth's Magnetic Environment

To first approximation, the Earth's magnetic field is a magnetic dipole tilted  $11^\circ$  from the Earth's rotational axis. The dynamo theory describes the mechanisms of churning liquid nickel and iron in the Earth's core which generate the Earth's magnetic field with a magnetic moment of  $8.07 \times 10^{22} \text{ Am}^2$ . The magnetic dipole is slightly displaced from the center of the Earth due to an inhomogenous distribution of magnetic matter above the core giving rise to large deviations in the dipole field at the surface (e.g., *Koskinen and Kilpua, 2022*). The active dynamo causes the magnetic variations of the Earth's dipole field including the drifting of magnetic poles and the polarity reversal. Geomagnetic observations from the last 400 years show a northward displacement of the dipole on the order of 2 km per year and a westward precession of the dipole axis of  $0.08^\circ$  per year. Paleomagnetism studies have shown evidence for the polarity reversal of Earth's magnetic field, in which the North and South magnetic poles exchange positions seemingly at random every 100 thousand to 1 million years, approximately (e.g., *Lanza and Meloni, 2006*, see Chapter 1 and 7). Faster changes on timescales of minutes to hours and days that are of concern for potential space weather hazards are due to the interaction between the magnetic fields of the Earth and the solar wind. Such coupling can cause distortion of the field far from the Earth's surface while generally maintaining a near-dipole resemblance near Earth's surface. An outline of the Earth's magnetosphere and ionosphere, and the geomagnetic storms and substorms with the potential to cause GIC-producing GMD, are outlined in the following subsections.

### **Magnetosphere**

The Earth's magnetosphere extends from the lower boundary at the top of the ionosphere to many Earth radii where the combination of the Earth's mag-

netic field and the magnetic effects from solar terrestrial coupling define the magnetic field and therefore impact the motion of particles. A schematic representation of the magnetic field in Earth's magnetosphere is shown in Figure 1.5. The incoming solar wind first reaches the bow-shock, a collisionless shock front upstream from the magnetosphere that slows the solar wind and converts a large proportion of the incident solar wind kinetic energy into electromagnetic energy (*Koskinen and Kilpua, 2022*). Following the bow-shock, the solar wind becomes compressed, heated and increases in density while retaining the IMF as it continues to travel toward Earth in the magnetosheath. The next boundary met by the solar wind is the magnetopause; the location and shape of which is determined by the balancing of the dynamic solar wind magnetic pressure and effects of the Earth's magnetic fields including magnetic pressure (e.g., *Koskinen and Kilpua, 2022; Kivelson and Russell, 1995*). The magnetopause separates the planetary magnetic field from the solar wind, which at Earth occurs at around  $10 R_E$  along the sun-Earth line during normal solar wind conditions, though it is quite sensitive to the solar wind and can be compressed on the dayside and elongated on the nightside during geomagnetic storms (*Kivelson and Russell, 1995*).

The magnetosphere also contains populations of charged particles brought by the solar wind or from the upflows from the ionosphere which are trapped by the Earth's magnetic field. Charged particles undergo three types of motion: gyro motion around magnetic field lines, bounce motion along the field lines from mirror point to mirror point, and a drift motion around the Earth - electrons traveling eastward and protons travelling westward. The drift motion creates a current system in the magnetosphere called the ring current which influences the magnetic field at the Earth's surface.

Of particular interest for understanding the dynamics of the magnetosphere which cause GMD is the Dungey cycle. Magnetic reconnection on the day-

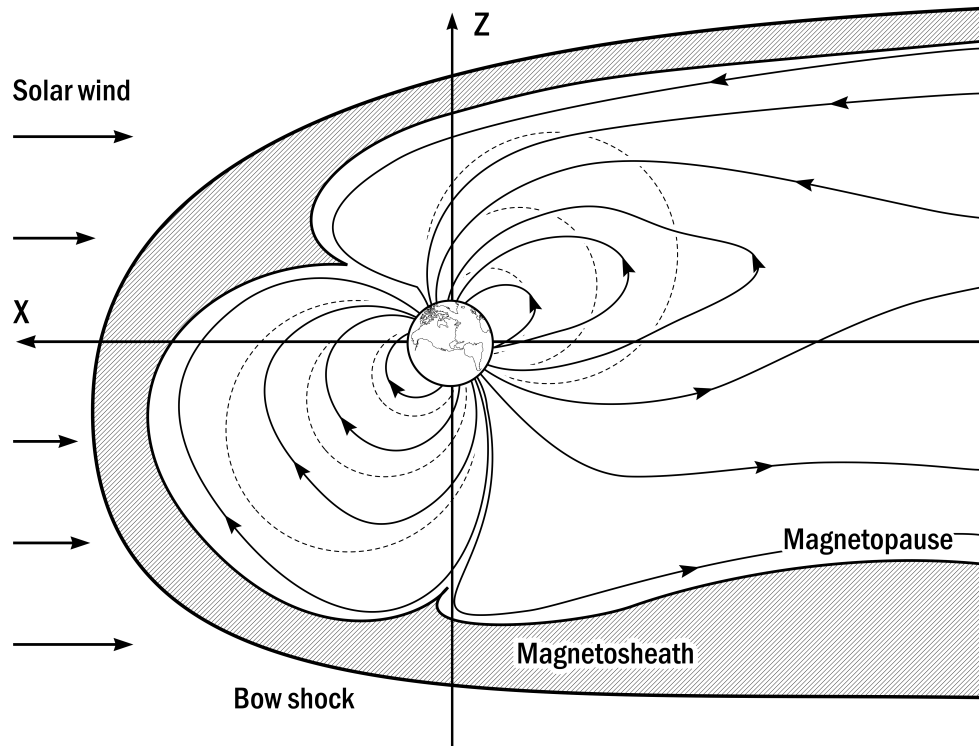


Figure 1.5: A schematic representation of the magnetic field in the magnetosphere shows the solar wind, incoming from the left distorting the Earth's magnetic field lines under normal solar conditions (solid) and a magnetic dipole (dotted) for comparison. Some regions of the upstream of magnetosphere are shown. Image credit: Andy Kale.

side occurs when a southward directed IMF brought by a CME or the solar wind interacts and merges with the northward geomagnetic field creating open field lines extending far past Earth. They are swept nightward and enter the magnetotail where two open field lines, one from each hemisphere in the north region and the south region of the magnetotail come together forming a single closed field line through nightside reconnection (*Dungey, 1961*). The reconnected stretched field lines will then flow back Earthward transporting frozen-in plasma and travel to the frontside magnetosphere through the dusk or dawn sector to conserve magnetic flux before the dayside reconnection can begin the process of this magnetospheric convection again under the action of

ongoing periods of southward IMF (*Baumjohann and Treumann, 2012*).

## **Ionosphere**

The ionosphere defines the transition region between magnetospheric plasma and the neutral atmosphere. In this region, particle ionisation can be accomplished through two mechanisms: UV radiation from the sun, and particle precipitation into the atmosphere from the magnetosphere (e.g., *Baumjohann and Treumann, 2012*). The very low density at high altitudes allows little to no rapid recombination to take place, forming a weak plasma with typical electron densities ranging from  $10^8$  to  $10^{12}$   $\text{m}^{-3}$ . To first approximation, the ionosphere can be defined by three main layers: the D region, below 90 km, is very weakly ionized due to higher density causing recombination through more frequent electron-neutral collisions, the E region, above 90 km, with an ionization peak at 110 km, and the F layer, above 130 km (e.g., *Kivelson and Russell, 1995*). Ionospheric currents which contribute strongly to the measured magnetic field at Earth's surface, and which are of importance in the generation of GMD, include strong electrical current associated with the auroral electrojets. These electrojet currents are produced when particle precipitation in the auroral oval causes significant ionization increasing conductivity (e.g., *Baumjohann and Treumann, 2012*). Non-uniform charge distribution causes potential differences to develop across regions, resulting in current flow parallel to the surface at approximately 100 km altitude and which can also be connected to field aligned currents (FAC) systems which flow into and out of the magnetosphere. The auroral electrojets can carry currents of  $10^6$  Amperes and due to their relatively low altitude contribute most strongly to magnetic field disturbances at the Earth's surface (e.g., *Baumjohann and Treumann, 2012*). Because of this, the auroral electrojet is sometimes used for modelling GIC to first approximation (*Boteler and Pirjola, 2017*).

## Ionospheric Hall and Pedersen Currents

In the polar caps and the auroral zones, the current systems become more complex. The FAC, mentioned above, flow along the Earth's magnetic field lines towards Earth at high latitudes which serves as the primary coupling system between the magnetosphere and ionosphere (e.g., *Le et al.*, 2010). The currents in the ionosphere flow in response to the electric field. Pedersen currents flow in the direction of  $\mathbf{E}$  and Hall currents flow in the direction of  $-\mathbf{E} \times \mathbf{B}$ , perpendicular to  $\mathbf{E}$  and therefore perpendicular to the Pedersen current (e.g., *Kivelson and Russell*, 1995), as seen in Figure 1.2.2.

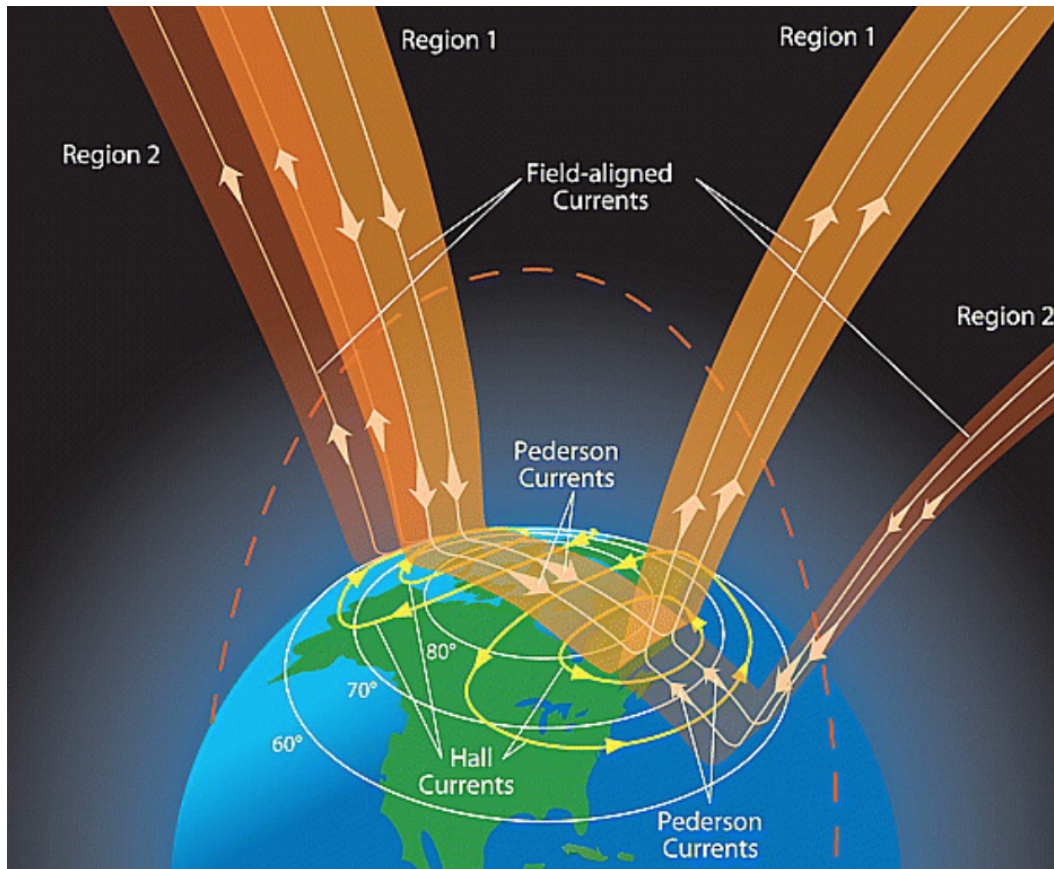


Figure 1.6: The coupling between the magnetosphere and ionosphere is shown by this schematic of the combined field align currents and the ionospheric current systems in the auroral oval (from *Le et al.*, 2010).

The variations in these currents during auroral substorms are known to be one cause of large GIC (*Viljanen et al.*, 2006, 1999). It is important to note that, by Fukushima's theorem, when the ionospheric conductivity is spatially uniform only corresponding Hall currents are revealed by ground-based magnetic measurements the combined Pedersen and field align currents cancel each other out at the ground (*Fukushima*, 1976). This has significant consequence when modelling the induction of horizontal electric fields in the Earth for use in GIC hazard analysis (e.g., *Pirjola et al.*, 2000, 2005).

### **Geomagnetic Storms and Substorms**

Geomagnetic storms are typically observed on Earth a few days after a CME. These geomagnetic storms are characterized as extended periods of geomagnetic activity that can persist for 1 - 5 days (*Kivelson and Russell*, 1995). The disturbance storm time index (Dst), which is determined using ground-based magnetometers, is a proxy for the intensity of geomagnetic storms and provides information on changes in the intensity of the ring current. Dst values become more negative as more particles are injected into the inner magnetosphere by the solar wind causing enhancement of the ring current. The initial phase lasting a few minutes to hours, is characterized by an increase in the H-component of the magnetic field strength. The main phase can last many hours and is classified by a large decrease in Dst typically reaching negative values on the order of 50 - 300 nT and in extreme cases, only a few times per solar cycle, 500 nT. Rapid recovery occurs over a period of many days as Dst values return to pre-storm levels (*Kivelson and Russell*, 1995).

Geomagnetic substorms are shorter disturbances lasting a few hours which can occur during magnetic storms or even when surrounded by ambient conditions of relative geomagnetic quiet and are more frequent than the magnetic storms described above. During these substorm events, the auroral electrojets

migrate to lower latitudes resulting in dramatic localized magnetic field variations. Like magnetic storms, substorms are described in three phases: the growth phase, the expansion phase and the recovery phase. The growth phase occurs when newly reconnected dayside magnetic flux is swept nightward by the solar wind and is stored in the northern and southern lobes of the magnetotail which stretches and thins the currents in the nightside plasmasheet. The mechanism responsible for the onset of the expansion phase remains controversial; however, it is generally agreed that near-Earth nightside reconnection subsequently causes an explosive release of energy toward Earth and also releases a plasmoid formed between the near-Earth and distant neutral lines which travels down the magnetotail (*McPherron, 1979*). This release of energy into the inner magnetosphere will cause the auroral electrojet to intensify and travel to lower latitudes resulting in a strong surface magnetic field with values reaching -200 to -2000 nT that can last 1-3 hours (e.g., *Kivelson and Russell, 1995*). Strong magnetic field disturbances observed at the surface can have a significant impact on the production of GIC during this period. Lastly, during the recovery phase, the magnetosphere relaxes and the surface magnetic field returns to quiet levels.

### **1.3 Induced Geoelectric Field**

The second to last step of the space weather chain is the induction of the geoelectric field at the Earth's surface whereby a resulting potential difference, responsible for the generation of GIC, can be produced in long conducting infrastructure at Earth's surface such as long power lines. The magnetic field is dynamic and time-varying during magnetic storms and substorms, as discussed in the previous section, which induces a geoelectric field as a result of Faraday's

law:

$$\nabla \times \mathbf{E} = -\frac{d\mathbf{B}}{dt} \quad (1.1)$$

The induced electric field then drives an electric current,  $\mathbf{J}$  inside the conductive Earth following Ohm's Law,  $\mathbf{J} = \sigma\mathbf{E}$ , and in other conductors to which this electric field is applied. The importance of the conductivity structure of the Earth,  $\sigma$ , is described in the next subsection. Although lacking information about the parameters of the power system can inhibit a proper calculation for GIC in the power network, the fluctuating horizontal electric field remains an important indicator for potential GIC indicators, specifically between the frequencies  $10^{-5}$  to 1 Hz. Frequencies larger than this are unable to couple into the power grid due to the inertial time-scale of the grounding connection, and at smaller frequencies the geoelectric field does not change on time scales quick enough to induce significant direct current (*Boteler and Pirjola, 2017*). As seen in Figure 1.7, current will begin to flow through the Earth when a large potential differential is formed. This current will pass through the grounding connections of the electrical power network and travel from one geographic area to another via electric power transmission lines.

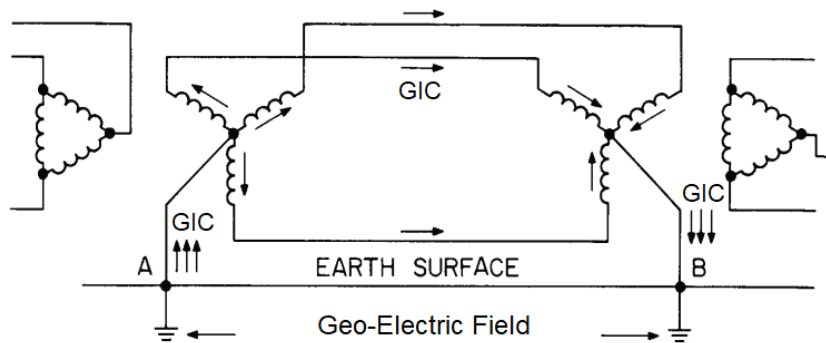


Figure 1.7: A schematic of a simple 3-phase transmission line and transformer grounding configuration illustrates the flow of GIC up through the grounding points at the transformer neutral, through the power line and back down through the second transformer into the ground (adapted from *Kappenman (2010)*).

### 1.3.1 A Simple Geoelectric Field Model

For the simplified case of a homogeneous Earth, we can illustrate the induction of currents in an overhead power line by following the description by *Boteler and Pirjola* (2017). An electromotive force,  $\epsilon$ , along a closed loop ABCD (Figure 1.8) is the negative of the time varying magnetic flux through the loop.

$$\epsilon = -\frac{d\Phi}{dt} \quad (1.2)$$

The calculation of a simple geoelectric field is done assuming the perturbed surface magnetic field,  $B_0$ , has harmonic time variation in the form  $e^{i\omega t}$ , where  $t$  is time and  $\omega$  is the frequency of the disturbance waveform. The surface field also attenuates with depth,  $z$ , like  $e^{-\frac{z}{\delta}}$ , where  $\delta$  is the skin depth. Assuming uniform conductivity of a 1D Earth and an incident planar electromagnetic wave, the complex skin depth describes the depth at which the surface field has been attenuated by a factor of  $1/e$  and is given by

$$\delta = \sqrt{\frac{2}{\omega\mu_0\sigma}} \quad (1.3)$$

where  $\mu_0$  is the permeability of free space. This formula determines the relationship between the penetrating depth of the signal, its frequency, and the Earth's conductivity: the lower the frequency and/or the lower the conductivity, the deeper the signal penetrates into the ground.

The magnetic flux through the loop ABCD is calculated by taking the integral of the surface magnetic field to an infinite depth and multiplying by the length of the power line,  $L$ .

$$\begin{aligned} \Phi &= \int_0^\infty B_0 e^{-\frac{z}{\delta}} dz \times L \\ &= \delta B_0 L \end{aligned} \quad (1.4)$$

Then, whereby Faraday's law states the electric field integrated around the

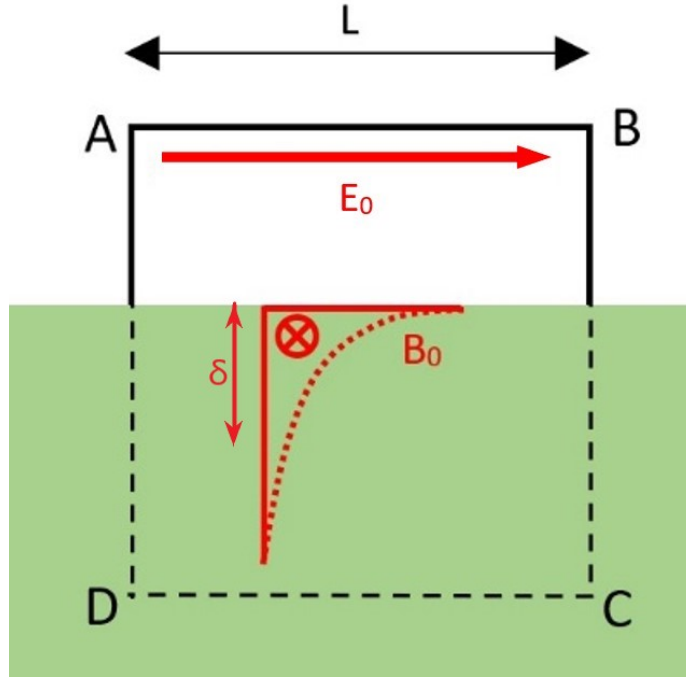


Figure 1.8: A schematic representation of magnetic induction through a loop, adapted from *Boteler and Pirjola (2017)*. The surface geoelectric field,  $E_0$ , is induced by the changing magnetic flux, where AB represents an overhead power line with length  $L$  and  $\delta$  is the complex skin depth.

loop ABCD is also given by the negative change in flux through the loop,

$$\oint_{ABCD} E \cdot dl = -\frac{d\Phi}{dt}, \quad (1.5)$$

the surface electric field can be calculated by substituting equation 1.4 into equation 1.5 and simplifying for the horizontal electric field,  $E_0$ :

$$E_0 = -i\omega\delta B_0 \quad (1.6)$$

This simple calculation of the geoelectric field highlights its dependence on the ground conductivity structure of the Earth, contained within the skin depth, and the space weather conditions.

### 1.3.2 Magnetotelluric Method

In this thesis, we adopt and use results from an application of the magnetotelluric (MT) method in which the geoelectric field is calculated and compared to the measured GIC in the electrical power network. Other methods to calculate geoelectric fields for use in GIC analysis not discussed in this thesis, but worthy to mention include the complex image method (CIM) (e.g., *Pirjola and Viljanen, 1998*) and the thin-sheet method (e.g., *Vasseur and Weidelt, 1977*).

First proposed by *Cagniard (1953)*, magnetotelluric surveys simultaneously measure the fluctuating electric and magnetic fields on Earth’s surface which are then used to calculate the impedance, which in turn describes the sub-surface conductivity structure of the Earth. MT is a passive geophysical exploration method which takes advantage of natural electromagnetic sources: at high frequencies, typically greater than 1 Hz, the source of the electromagnetic signal is global thunderstorm activity, and lower frequencies, at less than 1 Hz, the source of the signal is the interaction between the solar wind and the Earth’s magnetic field (*Naidu, 2012; Simpson and Bahr, 2005*). MT assumes the incoming electromagnetic wave is a plane wave vertically incident to a horizontally uniform Earth (*Cagniard, 1953*). MT also assumes a quasi-static approximation for the total current density meaning the displacement currents are negligible. Compared with the time varying conduction currents, the electromagnetic induction of the Earth is treated as a diffusion process (e.g., *Naidu, 2012; Simpson and Bahr, 2005*).

An MT sounding is used to provide information about the geometry of the sub-surface geology and its ability to conduct electrical current. Survey measurements relate the x and y horizontal components, northward and eastwards respectively, of the geoelectric field to the horizontal components of the geomagnetic field. A horizontal electric field,  $E_y$ , component can be represented in

terms of a perpendicular magnetic field,  $B_x$  component for a single frequency (Pirjola, 2002), where  $\omega$  is the frequency,  $\mu_0$  is the magnetic permittivity of free space, and  $\sigma$  is the conductivity:

$$E_y = -\sqrt{\frac{\omega}{\mu_0\sigma}} e^{i\frac{\pi}{4}} B_x. \quad (1.7)$$

An analogous relation exists for  $E_x$  and  $B_y$ . The relationship between the electromagnetic fields and frequency, and the penetration depth of the fields into the Earth as described by the skin depth effect (equation 1.3), permits the estimation of an apparent conductivity,  $\sigma$ . This relation is written and expressed in terms of a frequency-dependent surface impedance,  $\mathbf{Z}$ , where  $\mathbf{Z}$  has unit Ohms,  $\mathbf{E}$  has units  $Vm^{-1}$ , and  $\mathbf{B}$  has units  $T$  (Pirjola, 2002; Boteler, 1994).

$$\mathbf{E}(\omega) = \frac{1}{\mu_0} \mathbf{Z}(\omega) \mathbf{B}(\omega) \quad (1.8)$$

A series of MT surveys can be done to develop a 3-D model of the conductivity structure. This has been proven useful in characterizing the induced geoelectric field response where the conductive structure is not uniform (Cordell *et al.*, 2021; Marshall *et al.*, 2019; McKay and Whaler, 2006). For GIC related studies, this is an important element as the electrical system consists of a network which spans 1000's of kilometers with varying conductivity structures. Due to ground-based magnetic field data being relatively available and the increased effort to characterize local geological conditions, these elements can be used together to assess the geoelectric fields during extreme historical GMD events (e.g., Nikitina *et al.*, 2016; Love *et al.*, 2022; Bedrosian and Love, 2015). The three dimensional impedance tensor determined for a region in central Alberta, South-East of Edmonton, will be utilized in Chapter 5 to calculate the geoelectric field during recent geomagnetically active events for comparison against the electrical power industry GIC measurement.

## Chapter 2

# Geomagnetically Induced Currents

As discussed in the previous chapter, geomagnetically induced currents, ultimately driven by activity on the sun, can pose significant hazards on Earth in a grounded network of conductors such as those comprising the electrical power grid. GICs are low frequency,  $f < 0.01$  Hz, quasi-direct currents that flow along conductive pathways in modern technological infrastructure including oil and gas pipelines (*Pirjola, 2000*), railroad tracks (*Eroshenko et al., 2010*), and electrical transmission lines (*Boteler et al., 1998*). GIC magnitudes can range on the order of 1 – 100’s of Amperes with the largest GIC recorded in Sweden during a magnetic storm on April 6th, 2000 reaching almost 300 A (*Stauning, 2001; Pulkkinen et al., 2003*). Electrical networks, typically 50 or 60 Hz AC systems, are particularly vulnerable due to the fundamental characteristics of GIC, as will be explored in Section 2.1. Although not discussed in detail in this thesis, there is a renewed focus on developing passive and active mitigation devices and approaches to mitigate the impacts of and solve issues caused by the introduction of near-DC currents, such as the GICs causes by space weather, into the power system (*Rajput et al., 2021*).

Geophysical factors which influence GIC magnitudes are ground conductivity, emphasized in Section 1.3, and the size of the GMD which statistically

varies with latitude. At higher latitudes, close to and within the auroral oval where GMD is stronger and more frequent, there is a greater risk from GICs (Pirjola, 2000). Such studies on GIC in high latitude counties have been conducted in Norway (Myllys *et al.*, 2014), Sweden (Pulkkinen *et al.*, 2005; Wik *et al.*, 2008), Finland (Pirjola *et al.*, 2003), Russia (Sokolova *et al.*, 2019; Belakhovskiy *et al.*, 2019), and Canada (Boteler *et al.*, 1998; Bolduc, 2002, and references therein). To meet increasing global demand for reliable power generation and distribution, there is a growing trend to build long high voltage (HV) lines which are more vulnerable to GIC (Molinski, 2002; Zheng *et al.*, 2014). This in turn increases the vulnerability of lower and mid-latitudes power networks. GIC studies have also been conducted at low to mid-latitude countries including China (Zheng *et al.*, 2014; Zhang *et al.*, 2016), Japan (Fujita *et al.*, 2016), Australia (Marshall *et al.*, 2013), New Zealand (Marshall *et al.*, 2012; Mac Manus *et al.*, 2017), Spain (Torta *et al.*, 2017), the United Kingdom (Beamish *et al.*, 2002; Beggan *et al.*, 2021; Kelly *et al.*, 2017), among many others.

## 2.1 Effects of GIC in Power Systems

Transformers are used in power networks to either step-up or step-down the voltage in a power line. They are responsible for supplying transmission lines high voltage power for distribution across long distances and providing cities and residences with lower, safe, voltage levels for consumers at the receiving end of the distribution network. A simple transformer configuration consists of two coils wound around a laminated steel core. An alternating voltage is applied to the first, primary, coil which creates an alternating current and therefore an alternating magnetic flux in the core. This in turn, generates a current in the secondary coil which will either have a higher or lower voltage depending on whether the number of windings around the secondary coil is

more or less than that of the primary coil. During normal operation, transformers contain essentially all the magnetic flux within the laminated steel core; however, during GIC, the flow of quasi-DC current in the transformer winding introduces a near-DC flux in the core. Since transformers are designed specifically for 50-60 Hz AC systems, the much lower frequency of GIC,  $\lesssim 1$  Hz, can produce an offset of the magnetic flux density in the core resulting in the transformer reaching saturation in the half-cycle of the AC current (*Price, 2002; Gaunt and Coetzee, 2007*).

Saturation of transformers can lead to secondary physical and operational issues in the power system (e.g., *Molinski, 2002*). Transformer heating, often manifested as localized hot spots within the transformer, is created by improper distribution of AC magnetic flux in the core and can potentially cause permanent damage of transformer components. Deviations from the nominally sinusoidal power system current and voltage causes half-cycle saturated transformers to act as a source for even and odd harmonics in the system. Harmonics from multiple transformers have the potential to accumulate and generates total harmonic distortion (THD) (*Krarti, 2018; Lu et al., 1993*) which can trip protection and control systems in the network. Reactive power loss is also an outcome of half-cycle saturation and is a source of system disruption. Saturated transformers have higher reactive power consumption; therefore, changing the balance between real power, power available in the system, and reactive power, power fluctuating within the transmission system. The phenomenon causes system wide voltage fluctuations and instability, potentially leading to voltage collapse in the most extreme cases (*Pulkkinen et al., 2017*).

As stated earlier, GIC are only one impact to technology by space weather events. Disruptions to global positioning systems (GPS) and space-based communication systems can exacerbate emergency response in a serious power failure situation; therefore, it is important to comment that the repercussions of

a GIC event could be compounded by a series of space weather related issues occurring simultaneously.

## 2.2 Examples of Historical GIC Events and Outcomes

Historical GIC events have brought the potentially disastrous hazards posed by space weather starkly into focus and have encouraged policy makers to enact system-wide standards in the electrical power industry. One such event in the modern age was the Hydro-Québec power failure. A series of CMEs occurring from the same sunspot region were expelled towards Earth between March 6th and 12th triggering a geomagnetic storm that lasted approximately 30 hours on March 13-14, 1989 (*Bolduc, 2002*). The GICs generated in North America and Europe caused relay trips, voltage drops and transformer hot spotting; however, the worst effects were felt in Quebec where a large scale blackout affected six million people and resulted in an estimated total remediation cost of over 2 billion CAD (*Boteler, 2019; Czech et al., 1992*). Due to extensive population and industrial growth, the economic impact of an equivalent scenario today in the United States has been estimated to be approximately 40 billion USD per day (*Schrijver et al., 2014*). Other notable GIC events occurred during the Halloween storm of 2003 which left 50, 000 people without power in Malmö, Sweden (*Pulkkinen et al., 2005; Lundstedt, 2006*). Effects were also seen in China (*Liu et al., 2009*) and Russia (*Eroshenko et al., 2010*). Damage to several transformers in South Africa were also recorded (*Gaunt and Coetzee, 2007*). GIC were also observed in power systems in Europe, Africa, North America, and China (*Trichtchenko et al., 2007*) during a large geomagnetic storm on November 7-9th, 2004.

These events highlight the hazards caused by GMD and the resulting GICs, and has led to initiatives being taken by government and policy makers to pro-

tect the integrity of the power grid. Federal initiatives by the US, including an Executive Order during the Obama administration (Exec. Order No. 13744, 2016), have been taken to coordinate and prepare emergency response to space weather events. In the US and Canada, the North American Electric Reliability Corporation (NERC) has set regulations and standards for GIC mitigation, and requirements for GIC and GMD monitoring throughout the power system as outlined in the NERC standards report TPL-007 (*NERC*, 2020). The goal of TPL-007 is to characterize the GIC response for the power network across the continent during GMD events of different scales. To do so, requirements outlined in TPL-007 include measuring the fluctuating geoelectric and geomagnetic fields associated with GMD, monitoring the GIC flowing through the system, and the development of an accurate model of the grid response to different GMD events. Currently, the application of TPL-007 has not yet been introduced in Alberta by the province’s system operator, Alberta Electric System Operator (AESO). However, due to increasing pressure from the other jurisdictions in Canada and the US, there is rising interest from Alberta’s private electrical transmission companies to monitor such events and protect their own systems. Together with the existing capability in the province to measure GMD and provide ground conductivity profiles across the province, this places Alberta in an opportune position to expand research in this area.

A common existing approach to manage and mitigate the impacts of GICs in the network is to rely on geomagnetic storm forecasts, often provided by the National Oceanic and Atmospheric Administration (NOAA) Space Weather Prediction Center (SWPC) either in the form of their G-scale or through the forecasts at global activity indices such as Kp, coupled to simulations of the power network. With this approach, power system operators then determine the appropriate mitigation strategies which can involve manipulating network connections to reroute GIC away from vulnerable substations. This rudimen-

tary approach leaves the network exposed, since the intensity and localized disturbances structures are not well-described by these forecasts of large scale activity indices. Furthermore, existing mitigation strategies can only be used in limited situations and require supporting infrastructure; therefore, the development of passive and active GIC mitigation devices and methods is an active area of GIC research (*Rajput et al.*, 2021).

## 2.3 Measuring GIC

Proper assessment of space weather impacts on a power system requires measurement of GMD and the resulting GIC, and knowledge of the network connectivity to model the response to events with different characteristics and intensities. These three elements are the core requirements set by NERC in TPL-007 to provide increased reliability of the electrical network to which we deeply depend.

A common measurement method to measure GIC is to use a Hall effect sensor located on the transformer’s neutral-to-ground connection. This device provides a precise measurement of the DC component of the current flowing through the grounding wire on the opposite side of the transformer as the power line. Adding Hall effect sensors to the line-side of the transformer would improve interpretation of GIC impacts providing a more accurate representation of the DC flow in the network as has been done on some power network in Australia (Richard Marshall; personal communication). Due to the nature of this method, the installation of the sensor requires direct access to the equipment in the substation, specific safety considerations, and specialized power engineer training and time; therefore, the installation of these sensors across the network in multiple substations is not necessarily feasible and access to, and analysis of, this limited data requires close collaboration with industry.

### 2.3.1 Differential Magnetometer Measurement

An alternative approach to measure GICs is the differential magnetometer measurement (DMM) method. This method was first introduced by *Viljanen* (2009), and field tested at low latitudes by *Matandirotya et al.* (2016) on a single-phase high voltage (HV) line in Namibia and expanded to more complex HV systems at mid latitude in the UK by *Hübert et al.* (2020). As shown by these previous studies, the specific benefits of the DMM method is that it is simple, completely remote and non-invasive, and importantly, inexpensive compared to traditional methods such as installing Hall effect sensors. DMM is examined here as an economical approach with which to validate GIC models by performing temporary measurements of GIC at possibly multiple locations across the network.

The standard DMM configuration involves two fluxgate magnetometers, one placed directly underneath the power line referred to as the underline sensor, and the other placed at some distance perpendicular to the power line referred to as the remote sensor. Due to its specific placement, the underline sensor measures both the background magnetic field and the magnetic field caused by the GIC, while in the traditional configuration the remote sensor is placed far away enough as to not record the GIC produced magnetic field, but still be within proximity to measure the same fluctuating background field, and therefore serve as a base station to which data from the underline sensor can be compared. Theoretically, the difference between the measurements of the two sensors will be the magnetic field produced by the GIC,  $d\mathbf{B}(t)$ . In this case, it is assumed the near-DC component of the current flowing in the power line above is represented by a current carried by an single infinite straight wire conductor, as stated in Section 2.2(t), derived from Biot-Savart law

$$\mathbf{I}(t) = \frac{2\pi R}{\mu_0} d\mathbf{B}(t), \quad (2.1)$$

where  $R$  is the perpendicular distance to the line current, and  $d\mathbf{B}(t)$  is the magnetic field produced by the GIC.

Recent studies conducted by the British Geological Survey (BGS) expanded on the development of the DMM technique by the Namibia test-site design, and applied this method to an element of the more complex power grid system in the United Kingdom (*Hübert et al.*, 2020). Multiple DMM sites were deployed along double circuit HV power lines in the UK's highly connected system. The GIC calculated by DMM were validated against the few Hall probe measurements available. Although there was strong temporal correlation between the two measurements, there were significant differences in amplitudes. This discrepancy in GIC amplitude is addressed in our new DMM design and approach, outlined in Chapter 3, and is the focus of one of this thesis' major research topics.

# Chapter 3

## Instrumentation of Differential Magnetometer Method

Previously described in Chapter 2, the traditional approach of the DMM method involves deploying two magnetometers: one placed under the power line which measures the background magnetic field and the magnetic field produced by the quasi-direct current flowing in the power line during geomagnetically active times, and the second sensor placed in a remote location, typically 100-200 m away (*Hübert et al.*, 2020), which theoretically measures only the background magnetic field. The difference between these two measurements can then be used to calculate an inferred GIC in line overhead. This chapter will discuss the instrumentation of a proof-of-principle for a novel DMM approach in which we bring the remote sensor closer to the power line to where magnetic perturbation due to the GIC is also resolvable.

### 3.1 Benefits of the Augmented DMM Method

An alternative deployment configuration of the differential magnetometer approach is explored to address the significant discrepancies in GIC amplitude between the inferred GIC from the traditional DMM method and the neutral-to-ground current data as seen in previous studies by *Hübert et al.* (2020) and *Matandirotya et al.* (2016). In our DMM experiment, we further seek to sim-

plify the logistics of data collection. The goal of the design, developments and deployment of an improved DMM method through the research described in this thesis was to provide an accurate supplementary GIC measurement for use by the electrical power industry in Alberta. Designed for use in temporary deployments, this inexpensive and completely non-invasive method indirectly measures GIC on a segment of the power grid. The data can then be used for validation against network models and existing in-line GIC measurements using Hall effect sensor at the transformer neutral-to-ground connection, and to provide local characterization of the network response at locations where such neutral current measurements are unavailable.

Only limited GIC studies have been completed to date in Alberta due to the lack of data available, particularly the general absence to data of neutral-to-ground current measurements by industry. However, the recent installation of such sensors by AltaLink, one of Alberta's largest electricity transmission companies, provides a unique opportunity to validate and compare the industry GIC measurement and the GIC results derived using the differential magnetometer method. Installed Hall effect sensors at the neutral-to-ground connection at transformer substations at several locations across the province began operations during the spring and summer of 2021. As discussed in Chapter 2, Hall effect sensors measure the DC component of the current flowing and grounding wire of the transformer into and out of the ground. This measurement is used here to validate our inferred GIC derived from DMM calculations. Drawbacks of the Hall effect GIC measurements including the cost, the requirement for resources of specialized power engineer training and time, a limited number of sensors installations across a large network, and restricted access to industry data are addressed by the DMM method. This is strong motivation to design, test and develop a consistent and validated GIC measurement using the DMM technique, and seek to further test and optimize

it.

### 3.2 Development of a Novel DMM Approach

Here, we introduce a new variation of the traditional DMM approach. For our deployment configuration the remote magnetometer is instead placed closer to the power line; therefore, the magnetic perturbation due to the GIC,  $d\mathbf{B}(t)$ , is resolvable at both the underline and remote sensors albeit with different directions and magnitudes. The primary benefit of this strategy is that it produces two independent measurements of the GIC, one from each magnetic component orthogonal to the overhead power line, as illustrated in Figure 3.1.

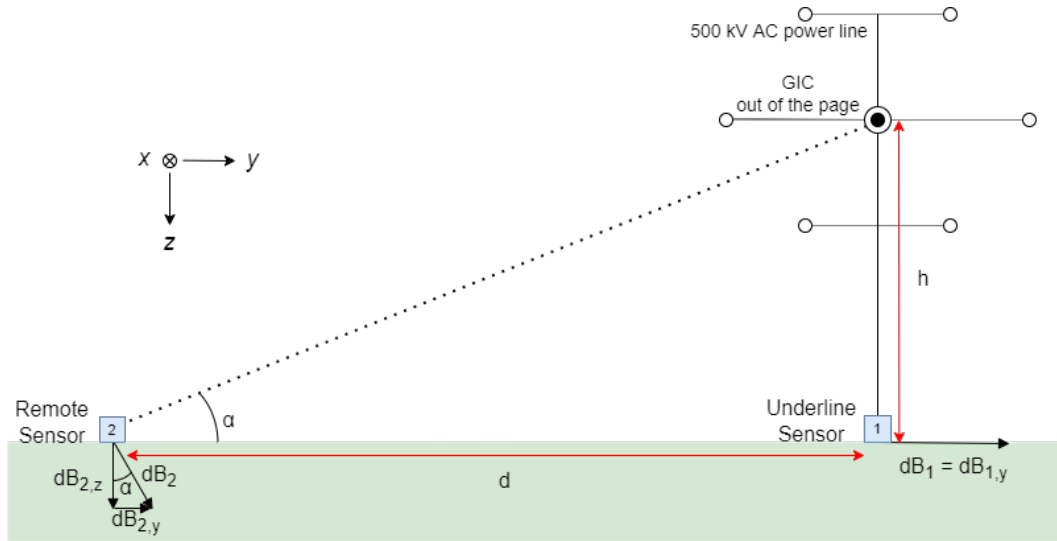


Figure 3.1: A schematic of our DMM deployment shows the relative location of each 3-axis fluxgate magnetometer with respect to the overhead double circuit power line, underline (1) and remote (2). Each magnetometer measures the background magnetic field,  $\mathbf{B}_0(t)$ , and the magnetic field from GIC in the power lines,  $d\mathbf{B}(t)$ , in the x (Northward), y (Eastward) and z (down) components.

The schematic in Figure 3.1 shows the relative distances of the sensors and overhead power line wires, and demonstrates the directions of the magnetic components produced by an assumed line current of the GIC disturbance

measured at each sensor. Since the power line segment of interest for this DMM validation runs North-South, the magnetic coordinate system used is as follows: the x component points into the page (geographic North), the y component points to the right (geographic East), and the z component points downward. On the right of this image, a phase power line carrying two 3-phase circuits is shown. Each 3-phase circuit is comprised of three wires and each wire in a single circuit carries a current with a phase difference of  $120^\circ$  from the others, hence the power line tower is shown with six overhead wires.

Information about the heights and span of the overhead wire bundles was provided by AltaLink. The conductor sag under nominal conditions is about 10m for each wire and the approximate height of the wire connections on the tower are 30 m, 40 m, and 50 m above the ground. The horizontal distances between pairs of wires are 18 m for the top and bottom rows and 30 m for the center row of wires. An important assumption worth noting is that for simplicity of algebra the GIC is calculated as a single equivalent line current flowing through an infinite conductor. This holds implications with regard to the geometry of the DMM setup. By the superposition principle, the GIC is assumed to be the sum of the quasi-DC current flowing through each wire bundle located at a height of 30 m and directly overhead of the underline sensor labelled sensor number 1; therefore, the underline magnetometer is assumed to record all of the GIC produced magnetic field in the y component, i.e.,  $dB_1 = dB_{1,y}$ , and the remote sensor records the GIC produced magnetic field in both the y and z components.

### 3.3 Deriving GIC from the New DMM Method

This new DMM deployment configuration offers the benefit of calculating two independent inferred GIC values: one derived from each perpendicular magnetic component as a result of the current flowing through the line,  $I(\Delta B_y)$

and  $I(\Delta B_z)$ . The infinite conductor assumption implies no GIC magnetic field exists in the x component parallel to the line; therefore, it is ignored.

The other unknown values are the background magnetic field in each component,  $B_{0,y}(t)$  and  $B_{0,z}(t)$  which are themselves functions of time and the space weather related GMD. Through a system of equations, we can solve for each and thereby separate  $\mathbf{B}_0(t)$  from  $d\mathbf{B}(t)$ . Where  $d\mathbf{B}(t)$  is the magnetic field produced by the GIC and is described by the Biot-Savart Law at some distance R,  $d\mathbf{B}(t) = \frac{\mu_0 \mathbf{I}(t)}{2\pi R}$ . We identify the sources of the magnetic field measured at each sensor in both y and z components and define the measured fields by the following equations. The subscripts denote the component and the sensor, where 1 is the underline sensor and 2 is the remote sensor.

$$B_{1,y}(t) = B_{0,y}(t) + dB_{1,y}(t) \quad (3.1)$$

$$B_{1,z}(t) = B_{0,z}(t) \quad (3.2)$$

$$B_{2,y}(t) = B_{0,y}(t) + dB_{2,y}(t) \quad (3.3)$$

$$B_{2,z}(t) = B_{0,z}(t) + dB_{2,z}(t) \quad (3.4)$$

Then, by taking the difference between the two sensors and solving for the GIC current inferred independently using each of the y and z components,  $I(\Delta B_y)$  and  $I(\Delta B_z)$  respectively, we obtained the following equations, where h is the height of the GIC above the ground, d is the distance between the magnetometers,  $\alpha$  is the angle at the remote sensor from the ground to the height of the GIC, and  $\Delta B_y$  and  $\Delta B_z$  are the difference in the magnetic fields measured at the two sensors in the y and z components respectively.

$$I(\Delta B_y) = \frac{2\pi}{\mu_0} \left( \frac{-1}{h} + \frac{\sin(\alpha)}{(h^2 + d^2)^{1/2}} \right)^{-1} \Delta B_y(t) \quad (3.5)$$

$$I(\Delta B_z) = \frac{2\pi}{\mu_0} \left( \frac{\cos(\alpha)}{(h^2 + d^2)^{1/2}} \right)^{-1} \Delta B_z(t) \quad (3.6)$$

This GIC estimate was validated against the neutral-to-ground current measured by AltaLink at a nearby transformer substation. Optimally, these Hall

effect sensors record with a sampling rate of 0.5 Hz, enough to measure high-frequency GIC information and for comparison against our 1 Hz magnetometer measurements.

Then, calculating the background magnetic field was achieved by subtracting the magnetic field of the inferred GIC from the total measured magnetic field:

$$B_{0,y}(t) = B_{1,y}(t) - \frac{\mu_0 I(\Delta B_y)}{2\pi} \frac{1}{h} \quad (3.7)$$

$$B_{0,z}(t) = B_{2,z}(t) - \frac{\mu_0 I(\Delta B_z)}{2\pi} \frac{\cos(\alpha)}{(h^2 + d^2)^{1/2}} \quad (3.8)$$

Data from one of the stations from an extensive magnetometer array across Canada, the Canadian Array for Real-Time Investigations of Magnetic Activity (CARISMA; *Mann et al. (2008)*), was used as a relative base station for comparison to our calculated background magnetic field,  $B_0(t)$ . The CARISMA station at Ministik lake (MSTK) was chosen as the relative base station as it was the closest to our DMM site. However, being only a distance of 48.5 km away it is closer than the height of the E-layer ionosphere carrying the ionospheric currents, and is therefore within a region where the spatial integration arising from the a Biot-Savart integration of the magnetic fields from currents in the overhead ionosphere should be smoothed out and relatively constant (e.g., *Hughes and Southwood, 1976*). Using the MSTK CARISMA station as a base station has limitations as it is not directly local to the DMM site, and thus may not provide a true representative background magnetic field. Therefore, it provides an excellent proxy for the strength and envelope of the GMD signature. CARISMA data from the MSTK station was further used for validation of the DMM method which is presented in Chapter 4, and for calculating the geoelectric field of historical storms from magnetotelluric impedance data in Chapter 5.

## 3.4 Instrumentation, Deployment, and Operation

The instrumentation used in the deployment of the differential magnetometer system was custom built in-house, using spare CARISMA magnetometry equipment including the two fluxgate magnetometers. The development of our DMM system was based on the concepts outlined by *Hübert et al.* (2020) and *Matandirotya et al.* (2016). This section examines details of the DMM equipment, deployment strategy and operations, including as described above the change to the location of the remote sensor.

### 3.4.1 DMM Equipment and Design

Two 3-axis fluxgate magnetometers were used for data collection. Three data channels, one for each component of the magnetic field, are recorded with a resolution of 25 pT at a sampling rate of 1 and 8 Hz, though the 8 Hz data is not used for analysis in this thesis as the frequency ranges of interest for GIC are lower than 1 Hz (*Boteler et al.*, 2019). Fluxgate sensors, developed by *Aschenbrenner and Goubau* (1936), are a commonly used tool for measuring fluctuating magnetic fields in the geospace environment and have many applications on ground- and space-based platforms for studying and monitoring space weather, and on Earth for geophysical surveys. The working of a fluxgate magnetometer is the direct consequence of Faraday's law. An alternating current is applied to a coil of wire called the drive coil which is wrapped around a ferromagnetic core and drives the core in and out of saturation. As the core moves out of saturation, the magnetic permeability increases concentrating the external flux created by the Earth's magnetic field through the core. The flux induces a voltage in the secondary or sense coil. The magnetic field is calculated from the induced voltage in each orientation of sense coils,

one for each component of the magnetic field (*Primdahl, 1979; Snare, 1998*). Importantly, the geometry of the fluxgate drive coils minimizes the coupling of the drive current and the sensor output.

Two 12V batteries were used and which could power our system from a fully charged state for 10-12 day intervals, then requiring site visits to replace the batteries and retrieve data. The batteries, computer, logger and GPS antenna were stored in a waterproof case (Figure 3.2). Each magnetometer was also disciplined by a GPS clock which ensured the data collection from each sensor was locked in time. Data was stored on an SSD hard drive. Power and serial cables ran out from this central box to each sensor's electronics box and sensor head. Each sensor head was encased in a box and secured with foam to reduce any possibility of shifting, as seen in Figure 3.3. A prior test deployment on a campus green space at the University of Alberta was done to ensure the sensors previously calibrated, and to ensure both field sensors and an additional backup sensor were working as expected. The system was built to prioritize mobility and ease of deployment, but to protect the components from water damage and weather. The motivation to use DMM as a temporary and supplementary GIC measurement for use by the power industry was the reasoning for these requirements.

The location of the remote magnetometer was determined by calculating the distance from the power line at which the remote sensor would record 1 nT for a GIC of 1 Amp. The optimal distance between the two magnetometers was calculated to be approximately 71 m. Limitations during field deployment of the magnetometers resulted in the exact distance between sensors being a few meters from this optimal distance.

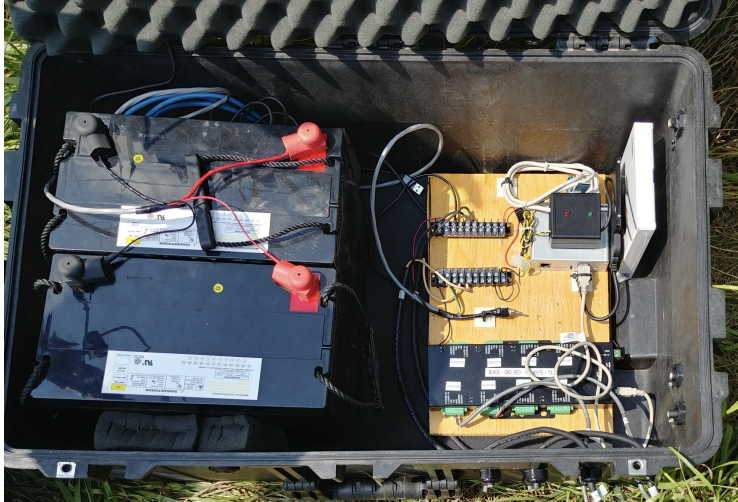


Figure 3.2: Batteries, computer, logger, and GPS antenna were stored in a waterproof container and connected to each sensor by power and serial cables.



Figure 3.3: Each three axis fluxgate magnetometer was secured and encased in a box. Horizontal coils can be seen from this top view. The boxes were then also filled with anti-static foam to secure the magnetometers orientation during field deployment.

### 3.4.2 Deployment and Operation

A deployment location was chosen based on the following requirements: the DMM system must record data for a power line segment where AltaLink had a nearby simultaneous neutral-to-ground current measurement. This industry measurement is essential for the validation of the DMM GIC values. The system must be deployed around a high voltage power line, which in the province of Alberta are either 240 or 500 kV. Long high voltage lines have been deter-

mined to be more susceptible to GICs (*Zheng et al.*, 2014). Referring to the *Hübert et al.* study as a guide for the application of the DMM method on a complex power system, we aimed to deploy around a similar double circuit power line which carries two three-phase circuits with a total of 6 wire bundles with one circuit on each side of the transmission tower in opposite phase sequence to each other. Also, the system should be placed at least 200 m from any road or railway to avoid magnetic noise sources. Lastly, the system must be placed in a secure location with a preference to deploy in a gated property to keep equipment secure from tampering or theft.

A location was chosen along a segment of the 500 kV power that runs North-South slightly East of Edmonton, Alberta. Access to, and deployment in an area of land in the back of a gated farm was generously agreed by a property owner in the area. The locations of the deployed DMM system, the industry's Hall effect sensors, and the CARISMA MSTK magnetometer station are shown relative to the 500 kV power line between the Heartland and Ellerslie substations, the North and South end of the power line, respectively, in Figure 3.4. The distance between the DMM field site and the MSTK station is 48.5 km.

The magnetometers were housed in a temporary concrete structure dug a few inches into the ground for stability against precipitation and wind. Figure 3.5 shows the how each sensor head was deployed. An approximate distance of 71 m was calculated to be the optimal distance between the magnetometers, based on which the remote sensor will measure a 1 nT change in the magnetic field due to GIC of 1 A in a power line with a height of 30 m overhead. During deployment the exact distances between the two sensors was measured to be  $73.5 \pm 0.5$  m, varying from the optimal distance due to natural obstacles on the field site. The distance was determined using a field measuring tape. Power and serial cables ran from each sensor to a box housing the magnetometer

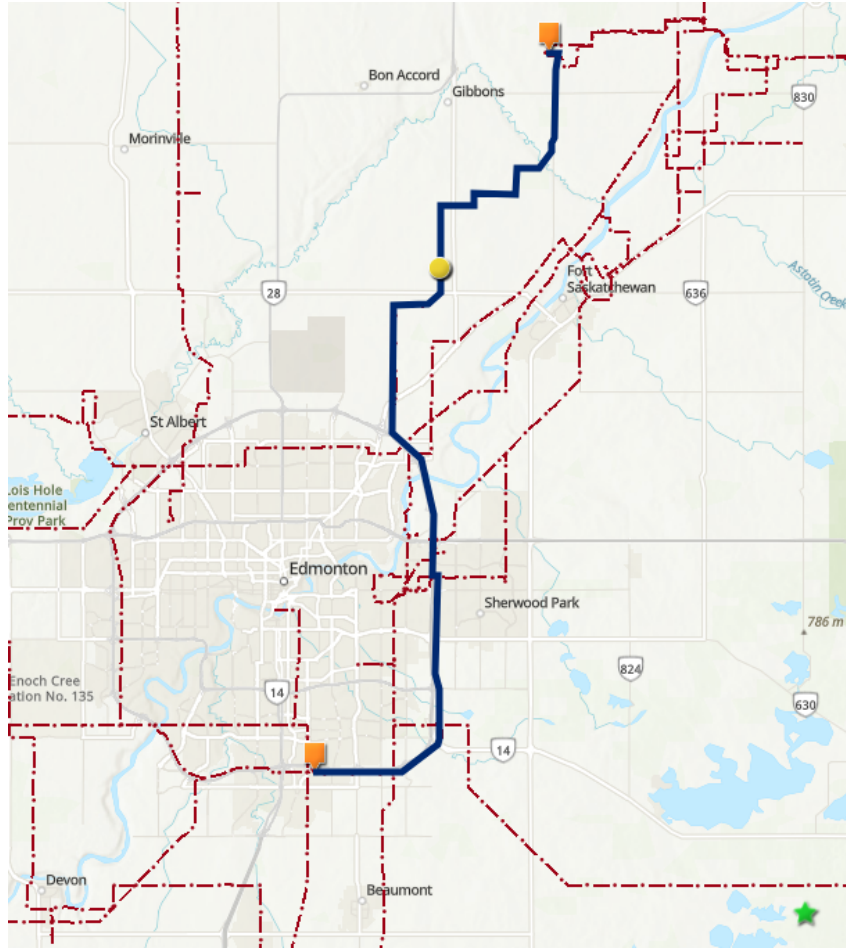


Figure 3.4: A map of the main electricity transmission lines around Edmonton and surrounding areas. The map shows the location of the 500 kV line (blue), the location of the transformer neutral current measurement (orange squares), the deployed DMM system (yellow circle), and the CARISMA station (green star). The map was created using ESRI ArcGIS software (ESRI Basemap: Topographic (2013); Government of Alberta: Powerline, utility\_access (2021); H.Parry: Power Lines and Magnetometer Locations (2021)).

electronics and then to a central box which contained the batteries, logger, computer, and GPS antenna. The magnetometers were leveled and orientated to point to geomagnetic north, and zeroed in the y component.

### 3.4.3 Uncertainties in DMM Derived GIC

Uncertainties in the DMM inferred GIC are introduced to the system from the installation including potential misalignment of the sensors, errors in the



Figure 3.5: Images of the underline sensor near the 500 kV power line. a) A concrete structure houses each magnetometer. b) A view of the inside of the concrete structure shows the fluxgate magnetometer under the power line.

distance between sensors and precise geometry, and estimating the uncertainties in distance from each magnetometer relative to the overhead wires. An absolute error of  $< 10 \text{ pT}/\sqrt{\text{Hz}}$  at 1 Hz is baseline noise of the fluxgate magnetometers. The two sensors are co-aligned by precisely leveling and zeroing the magnetic east component to within 10 nT. We estimate this is the uncertainty due to misalignment of the sensors in each the component. A total positional uncertainty is derived from the errors in estimating the distance from the magnetometer to the transmission wires for each sensor. The primary assumption of the DMM technique is the power line through which the GIC is flowing is an infinitely long straight conductor. This assumption is not perfect due to the sag present in the line, which fluctuates with the environmental conditions. The underline sensor is placed slightly displaced from the center point between the two pylons due to limitations during deployment, approximately

26 m. The typical span between the two towers is 365 m. Using the equations defined in *Grigsby* (2007, Chapter 14), a calculation of the sag above the underline sensor is 0.24 m less than the nominal sag at mid height. This is well within the error in the line height for the GIC, so we continue to assume the the GIC can be represented as a single equivalent line current flowing through a infinitely long conductor 30 m above the underline sensor. Information gathered during correspondence with AltaLink on the wiring of high voltage towers in the transmission lines informed the following uncertainties: the nominal sag in the line is approximately 10 m with a mid span height of  $30 \pm 2$  m (AltaLink engineers Colin Clark and Peter Blakeman; personal correspondence). For the remote sensor, an additional error arises from measuring the distance between sensors using a measuring tape which has an uncertainty of 0.5 m. Note of course, that for simplicity, we only assume a single equivalent current here, despite there being six overhead current lines. As discussed by *Hübert et al.* (2020), this can be addressed using more complex algebra associated with the actual pylon geometry. The percent error due to the positional uncertainty at the underline sensor for a GIC 30 m overhead is 6%, and at the remote sensor this decreases to 1%.

As an example, we determine the total error of a GIC of 20 A flowing in the transmission line modelled by a single infinite line current at the mid-span sag height, 30 m, directly above the underline sensor. A 20 A GIC generates a 133 nT magnetic field at the underline sensor and a 50 nT field at the remote sensor. The positional uncertainty, determined through error propagation methods, at the underline sensor in  $y$  is 8 nT, and the remote sensor in  $y$  and  $z$  is 2 nT and 5 nT, respectively. The root-sum-square calculation of uncertainty is calculated, and the error in each  $\Delta B_y$  and  $\Delta B_z$  is 13 nT and 10 nT, respectively. Finally, again by applying rules of error propagation to equations 3.5 and 3.6, the error for the DMM inferred GIC of 20 A in  $I(\Delta B_y)$

and  $I(\Delta B_z)$  are 3 nT and 5 A, respectively. This is higher than the error determined for the *Hübert et al. (2020)* DMM study; however, their system was more robust for permanent deployment while ours was developed with the purpose of more mobile and temporary investigations. *Hübert et al. (2020)* were able to perform a more rigorous positional determination; therefore, the positional uncertainty arising from the distance between the sensors and the distance between each sensor and the power line was smaller.

### 3.5 Upgrades for Future Deployments

Ongoing work is being done to improve our DMM set up and deployment strategy. The primary difficulty from the first deployment in the summer of 2021 was the frequency in which site visits needed to be performed. The use of 12V batteries as a power supply was the primary limitation, and required a battery swap every 10-12 days. During these site visits, data was also collected from the computer. To address these points, a solar panel and battery system as the power supply and a modem for sending data is now being integrated into the set up for future experimental campaigns. Using a modem to retrieve the data will be a drastic upgrade as it will make it possible to examine the data in near real time to assess whether the system is operating correctly without visiting the deployment location. Reducing the number of visits to the site will have the added benefit of decreasing possible errors resulting from human interference, for example by unintentional disturbing the sensor orientation while on site.

One issue that we did observe during the deployment campaign during early- to mid-October was heaving of the soil beneath the sensors during times of overnight freezing in the fall, causing a diurnal rotation in the x and y components as a result of the freeze thaw cycle. Reviewing temperature and weather data from a nearby Natural Resources Canada weather station, the

heaving was contemporaneous with the freezing temperatures overnight. Since the DMM equipment has been developed to be used for temporary deployments only, a full winterized kit is not available and was not required for the work we aimed to accomplish here. In attempt to resolve this, gravel will be placed under the concrete slabs to in future deployments to reduce the effects of frost heaving.

Lastly, the sources of uncertainties during the initial deployment in 2021 is dominated by positional errors which were not well-constrained, particularly the determination of the power line heights above ground. Information provided by AltaLink on the 500 kV power line circuits and towers including heights of each phase, heights of the tower connection points, a power line sag were nominal values for the specific segment of the power system on which we were measuring GIC with DMM rather than actual measured values of the towers at the DMM location. Using the given values by AltaLink is not sufficient. More precise measurements for position relative to the power lines will be done to reduce uncertainties caused by positional error.

## 3.6 Summary

In this chapter, we discuss the motivation of deploying an improved DMM system where the secondary magnetometer is deployed closer to the magnetometer directly under the power line such that both sensors can resolve the magnetic field perturbation due to the GIC overhead, although with different directions and magnitudes at each. This strategy provides two independent measurements of the GIC, one from each orthogonal magnetic component to the direction of the GIC, as illustrated in Figure 3.1. The derivation of the inferred GIC from each component is outlined and given in equation 3.5 and 3.6. The background GMD can also be calculated by removing the GIC produced magnetic field from the total measured field, as stated in equation 3.7 and 3.8.

Also, a complete and detailed discussion of the instrumentation including the equipment and design of our system, and the deployment strategy and operation is provided. The most significant errors in the system are a result of the positional uncertainties from the assumed distances between each sensor and the overhead power line. Other sources of error come from the measurement of distance between the two magnetometers and the precision achieved in leveling and alignment between the two sensors. Finally, upgrades to the system are suggested based on the initial assessment of the ease of deployment and maintenance of the system, and the sources of error.

# Chapter 4

## Validating the Novel DMM Approach for GIC Analysis on Alberta's High Voltage Network

### 4.1 Introduction

In this chapter, we present observations of the inferred GIC derived from the novel differential magnetometer method we developed and described in chapter 3. The inferred GIC was calculated from the magnetic disturbance measured by our installation of dual magnetometers in our DMM system close to a high voltage electrical transmission line in central Alberta during the interval of a moderate geomagnetic storm on October 12th, 2021. We used neutral-to-ground current data from a nearby transformer substation provided by our industry partner, AltaLink, to seek to validate this technique. Whilst the transformer neutral-to-ground current monitor does not provide a direct measurement in the power line, nonetheless and as we will show, it provided a current measurement consistent with that diagnosed using DMM. The combination of these local GIC measurements ultimately helps in understanding the response of the high voltage electrical power network in Alberta to geomagnetic activity of varying intensity during magnetic storms.

In the following sections, measurements from the differential magnetome-

ter method and the resulting inferred GIC, during a geomagnetically quiet time and a geomagnetically active time are compared. We partially validate the calculated GIC, derived from the DMM method by directly comparing the time variation of this current to the neutral-to-ground current measured at the Ellerslie transformer substation. We demonstrate, using example data from the October 12th, 2021 storm, the benefit of introducing an intermediate magnetometer placed within the region where the magnetic field produced by the GIC,  $d\mathbf{B}(t)$ , can be resolved. The y and z components of the recorded magnetic field at this intermediate location contain a component of  $d\mathbf{B}(t)$  which is perpendicular to the direction of the GIC along the power line. By taking the difference in the measurements from the two DMM sensors in each component, we demonstrate how this allows us to calculate two independent measurements of GIC,  $I(\Delta B_y)$  and  $I(\Delta B_z)$  derived using only the  $B_y$  or  $B_z$  component, respectively. An additional advantage is the ability to thereby remove the magnetic perturbation generated locally by the GIC and estimate the driving GMD from the DMM data. The background magnetic field calculated using DMM can then be compared against the magnetic field measured by a proximal base station from the CARISMA (Canadian Array for Real-time Investigations of Magnetic Activity) magnetometer array at Mistik Lake (MSTK), 48.5 km away. Overall, in this chapter we compare our modified DMM technique to the traditional DMM approach with the goal to address the discrepancies between them. Sources of error introduced by positional uncertainty and the limitations of the transformer neutral-to-ground current data for assessing GMD and GIC-related network vulnerability are also discussed.

## 4.2 Data and Methodology

Our DMM system was deployed at a field site North of Edmonton, Alberta under a North-South orientated segment of a 500 kV power line ( $53.731^\circ$  N,  $113.335^\circ$  W). GIC monitoring devices installed and continuously operated by AltaLink on both the North and South end of the power line makes this particular line an excellent candidate for demonstrating a proof-of-principle of our DMM method through a temporary field deployment at this location. Our two DMM magnetometers were deployed in July 2021 and remained in the field collecting magnetic field data until October 15th, 2021. Access to transformer neutral-to-ground current data was provided by AltaLink, one of Alberta’s largest power transmission companies. This data is used for comparison to the inferred GIC using DMM. Incomplete data from the closest neutral-to-ground current sensor at Heartland transformer substation, approximately 16 km to the DMM site, required us to instead use data from the Ellerslie substation ( $53.434^\circ$  N,  $113.460^\circ$  W), approximately 30 km away from our DMM location, for this comparison. Lastly, a proxy for the background GMD was recorded using CARISMA’s MSTK magnetometer station (*Mann et al.*, 2008) and which served as an effective base station whose data can be compared to that derived using our new DMM technique.

The differential magnetometer set up measures the overall GIC travelling through the multiple overhead power lines which comprises two 3-phase circuits for a total of six wires. Each circuit is connected to a separate transformer. The industry transformer neutral-to-ground current measurements provide the DC component of the current through the ground wire for each circuit. The neutral-to-ground current flowing through the grounding point of each circuit’s transformer at Ellerslie substation therefore needs to be considered. We assume both circuits carry the same current; therefore, the total GIC through

the system can be considered to comprise a single equivalent GIC line current which, rather than being carried in wires at different heights in the pylons, as discussed in Chapter 3, can be assumed to flow at a height of 30 m directly above the underline sensor. This assumption would not hold if the currents in the individual circuits are not balanced, which is theoretically possible as the transformer of each circuit operates independently. However, from the neutral current data provided by AltaLink, it is evident that on this day this is not the case and each transformer sees the near-DC current flowing between the system and the ground to be of nearly the same amplitude, validating this assumption (Figure 4.5).

Following the approach outlined in *Matandirotya et al. (2016)*, a rotation to the horizontal magnetic field was applied in post-processing shown by equation 4.1.

$$\begin{bmatrix} B_{x,geo} \\ B_{y,geo} \end{bmatrix} = \begin{bmatrix} \cos(\theta) & \sin(\theta) \\ -\sin(\theta) & \cos(\theta) \end{bmatrix} \begin{bmatrix} B_{x,mag} \\ B_{y,mag} \end{bmatrix} \quad (4.1)$$

Since the power line is oriented in a North-South geographic direction and the magnetic field is measured in geomagnetic coordinates, only a single rotation from geomagnetic to geographic coordinates is necessary. At the DMM field site during the time of deployment in 2021, the angle from geomagnetic north to geographic north was  $14.08^\circ$ . At MSTK station, the declination angle was  $13.85^\circ$ . The DC offset is removed from each component of the raw magnetic field data by subtracting the mean amplitude from the entire day.

Chapter 3 previously described the calculations required to obtain an inferred GIC from the magnetic field measurements and is not reviewed in detail again here. In this chapter, the processed magnetic field data for a geomagnetically quiet day, September 26th, 2021 and a geomagnetically active day, October 12th, 2021, are compared. In each case, the difference between the vector magnetic fields monitored by the remote and underline sensors in the DMM systems was determined to calculate the inferred GIC using the steps

outlined in Chapter 3.3. The GIC calculated using the DMM method is then compared to the neutral-to-ground current from the Ellerslie substation and conclusions are drawn.

## 4.3 Results

In this section, we compare the geomagnetic field measured by the DMM sensors and MSTK station for a geomagnetically quiet day on September 26th, 2021. This analysis of a quiet day is used to assess the signal to noise, and to begin to assess any error arising from the deployment of the DMM sensors, especially where their data are used differentially. Further, we use this effectively as a null event to examine whether the MSTK station can be reliably used as a remote base station. An analysis of the GMD observed during the geomagnetic storm and the inferred GIC on October 12th, 2021, is then presented. We show measurements for the magnetic field measured at each DMM sensor, the difference between each sensor, and the calculated GIC using the DMM method. Additionally, we provide a calculated background magnetic field from the system of equations outlined in Section 3.3, to assess the difference between the data during GMD inferred using the combined DMM station data and that observed directly at MSTK.

### 4.3.1 Geomagnetically Quiet Day

#### Quiet Day on September 26th, 2021

The magnetic measurements, in geographic coordinates and DC offset removed, on a quiet day, September 26th, 2021, are plotted in Figure 4.1. We see strong agreement between the data from both DMM sensors and that from MSTK station. This is expected for times with weak geomagnetic activity as the daily variations at two locations within a distance less than the ionospheric E-layer height, where the ionospheric currents are assumed to flow, should see

a similar magnetic field resulting from Biot-Savart integration and cancellation magnetic effects of the smaller scale ionospheric currents overhead (e.g., *Hughes and Southwood, 1976*). Since the GMD is also weak, any local GIC should also be small, such that all three magnetometers might be expected to record the same magnetic field.

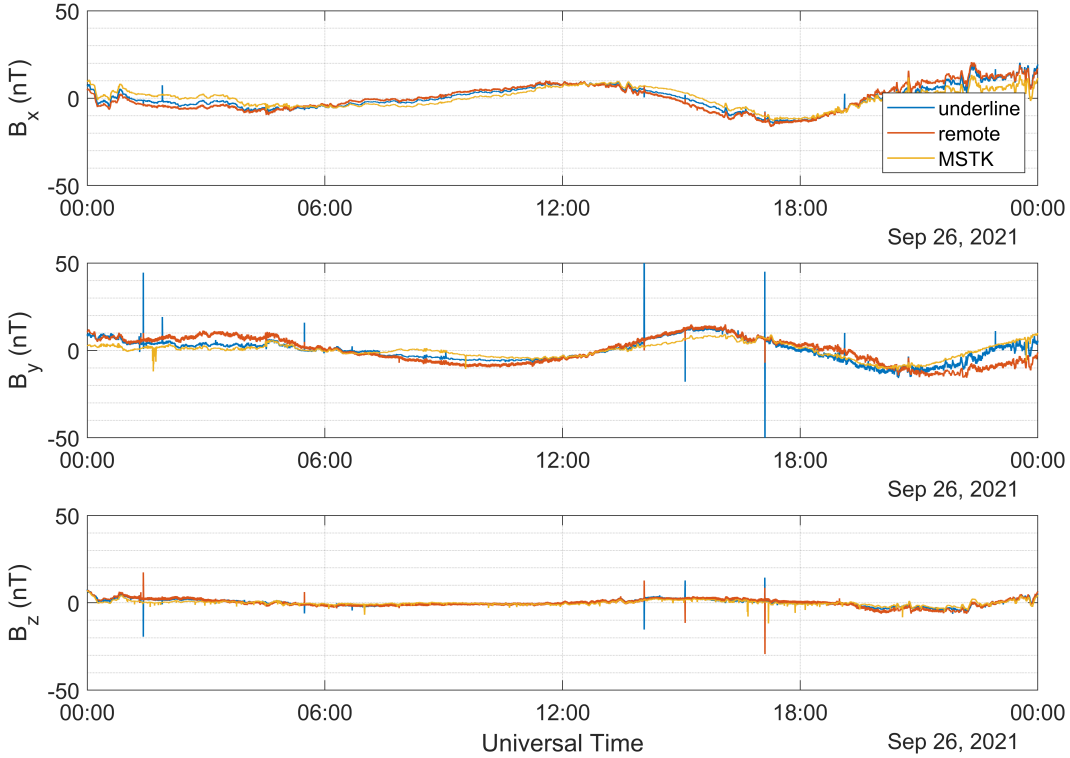


Figure 4.1: Magnetic field measured by the underline and remote DMM sensors and the MSTK base station on September 26th, 2021, a geomagnetically quiet day, in each coordinate  $x$ ,  $y$  and  $z$ , where  $+x$  is Northward and  $+y$  is Eastward, and  $+z$  is down.

The comparison between these three magnetometer data sets allows an assessment of the quality and stability of the data especially for the temporary DMM deployment. Noticeably in the  $y$  component, the two DMM sensors vary more through the day as compared to the MSTK sensor which remains more constant. The temporary design of the DMM deployment limits the stability of the structure supporting the DMM magnetometers, whereas the MSTK magnetometer is mounted on a stable concrete block intended for per-

manent deployment. If the soil underneath the two DMM sensors expands and shifts due to heating and cooling due to sunlight and weather conditions, the magnetometers will rotate and become misaligned from geomagnetic north.

The difference between the components measured by the two DMM sensors is plotted in Figure 4.2 revealing interesting daily variations between the data of the two DMM magnetometers. While the x and z component are quite consistent across both DMM sensors, the y component sees the largest variation through the day with a maximum difference of 10 nT near the end of the day. This can be reasonably ascribed to the errors identified in Section 3.4.3. This estimate is dominated by the misalignment of the sensors, 10 nT, which remains constant for all GIC magnitudes; therefore, the variation of  $\Delta B$  can be reasonably attributed to this factor. The mean deviation from the median, where the median is zero, is 1.6 nT, 2.8 nT, and 0.7 nT in the x, y and z components, respectively. Furthermore, the error estimate determined in Chapter 3 did not consider any possible shifting of the sensors due to frost heaving in the soil. This will be further investigated in the following section. Spikes in the quiet time data was identified to likely be noise from either nearby vehicles or tractors. Each spike is approximately 5 to 10 seconds long and has a bipolar signal consistent with a large metal object passing by on this timescale. These signals are also only present during local daytime hours, as local sunset and sunrise occurred at 1:22 UT and 13:28 UT, respectively. Overall, however, especially between around 6:00 - 15:00 UT, there is excellent agreement between all three magnetometer data sets to significantly less than 10 nT accuracy.

### **4.3.2 DMM Inferred GIC: October 12th, 2021**

#### **Geomagnetic Storm on October 12th, 2021**

A GIC was experienced by the high voltage electrical power network in Alberta due to a moderate geomagnetic storm that lasted 12 hours on October 12th,

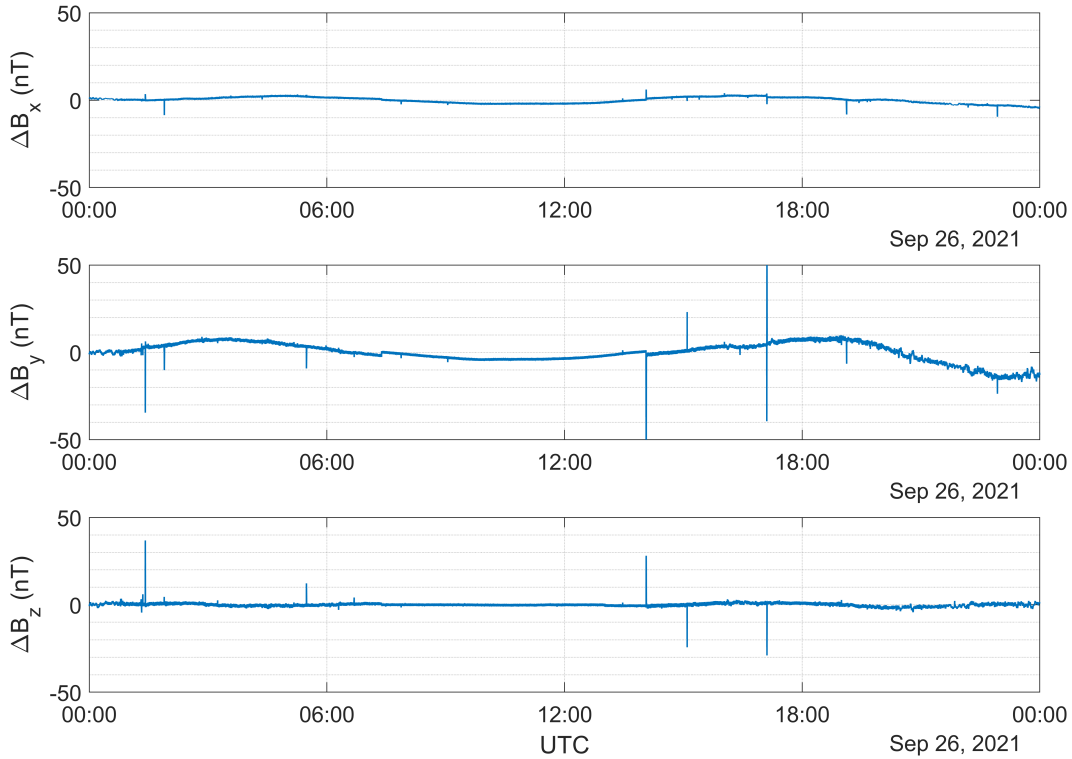


Figure 4.2: The difference between the underline and remote sensors on September 26th, 2021 in each component.

2021. The magnetic storm was triggered by a CME on the Sun two days prior on October 10th, 2021. Space weather conditions from the Space Weather Prediction Center (SWPC) at the U.S National Oceanic and Atmospheric Administration (NOAA) showed a prolonged period of southward-IMF,  $B_z$ , and a sharp drop in  $B_z$  coinciding with a 120 km/s uptick in the solar wind speed at 1:45 UTC which signalled the start of the storm. The total interplanetary magnetic field magnitude reached 17 nT and a KP index of 6 was reached. The storm double peaked in activity at approximately 6:00 UT and 12:00 UT (<https://www.swpc.noaa.gov/products/real-time-solar-wind>). The geomagnetic activity on this day produced the chain of events, as discussed in Chapter 1 and as we will show here, leading to a geomagnetically induced current in the power line. This event therefore provided an excellent opportunity to evaluate the effectiveness of our improved DMM method and validate

this technique against available industry GIC data. Figure 4.3 shows the time series of the magnetic field in the x, y, and z components in geographic coordinates as measured by the underline and remote sensors of the DMM system, and by the magnetometer at MSTK station on October 12th, 2021.

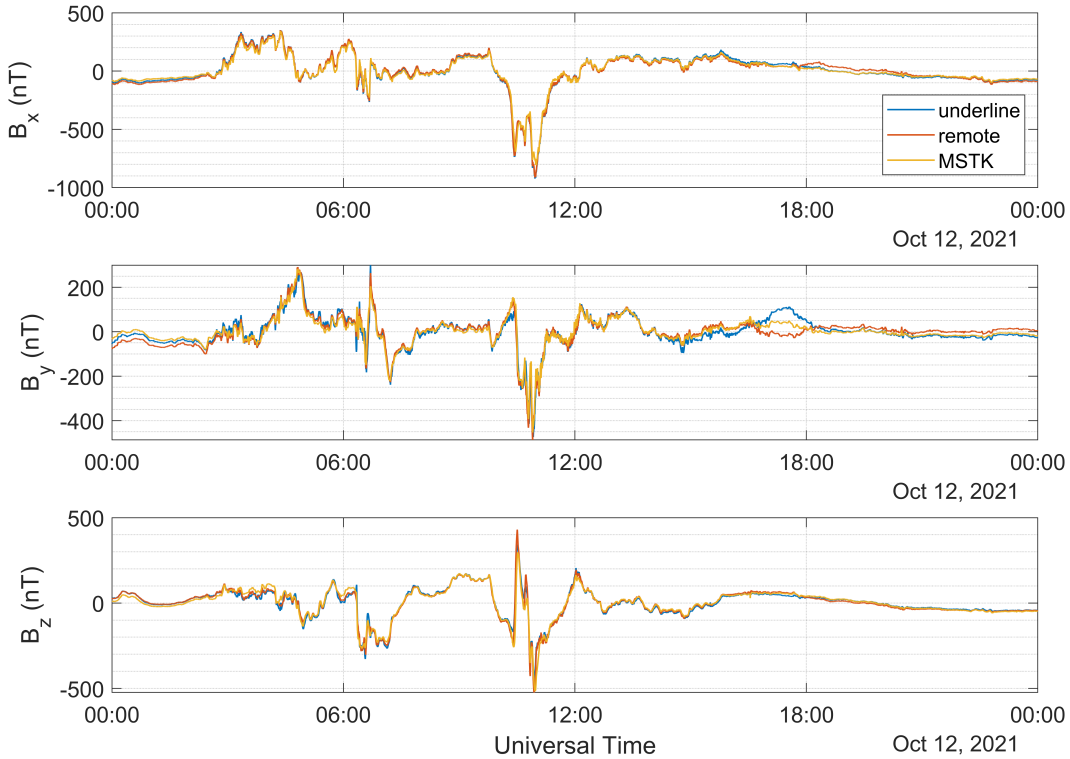


Figure 4.3: Magnetic field measured by the underline and remote DMM sensors and the MSTK base station on October 12th, 2021, a geomagnetically active day, in each coordinate x, y and z, where +x is N and +y is E in geographic coordinates.

The first obvious difference as compared to Figure 4.1 is the magnitudes of the GMD as seen by all three magnetometers. MSTK clearly provides a strong proxy for driving GMD, but its values deviate from the differential magnetometer measurements significantly, particularly in the y component around the times of the strongest magnetic disturbance, exactly as would be expected if the DMM stations are additionally measuring magnetic perturbation associated with local and overhead GIC in the power line. There also appears to be an interesting feature from around 17:00 to 19:00 UT in  $B_y$  where all

three stations have significantly different magnetic fields. There is also some baseline divergence between two DMM magnetic field, but overall the data appears amenable for DMM analysis.

### Measuring GICs Using DMM

The magnetic field in each component at the underline and remote DMM magnetometers, and the component-wise difference between the two, is shown in Figure 4.4 in the left and right columns, respectively. The peak-to-peak amplitude of the difference in the x component, the component parallel to the power line and the direction of the GIC flow, and for which we assume a perfectly straight infinite line current, is less than 20 nT, disregarding an anomaly occurring between 14:00 to 19:00 UT. This in itself is a significant result as it confirms that the difference in the magnetic field recorded by each DMM sensor in the y and z components can be predominantly associated with the GIC flowing overhead. This further confirms what we expect for the errors in  $\Delta B$  since  $\Delta B_x$  in this case is expected to be zero as a consequence of the location of the sensor and the assumed geometry of the power line. The predominant source of error in the differential magnetometer measurement,  $\Delta B_{y,z}$ , is due to the misalignment between the sensors and the positional uncertainty, as previously examined in sections 3.4.3 and 4.3.1, and was determined to be greater than 10 nT. This agrees with the variation of  $\Delta B$  in the x component.

A significant variation in magnetic field measured by the DMM sensors occurs during the late hours of the data. It is most visible in the y component around 14:00 to 19:00 UT. On October 12th, 2021, the minimum temperature reached was  $-5.9^\circ\text{C}$  at 14:00 UT and the maximum temperature was  $9.8^\circ\text{C}$  at 21:00 UT. Below freezing temperatures were maintained from 1:00 to 13:00 UTC, according to historical climate data from Environment and Natural resources Canada (<https://climate.weather.gc.ca>). The anomaly is coincident

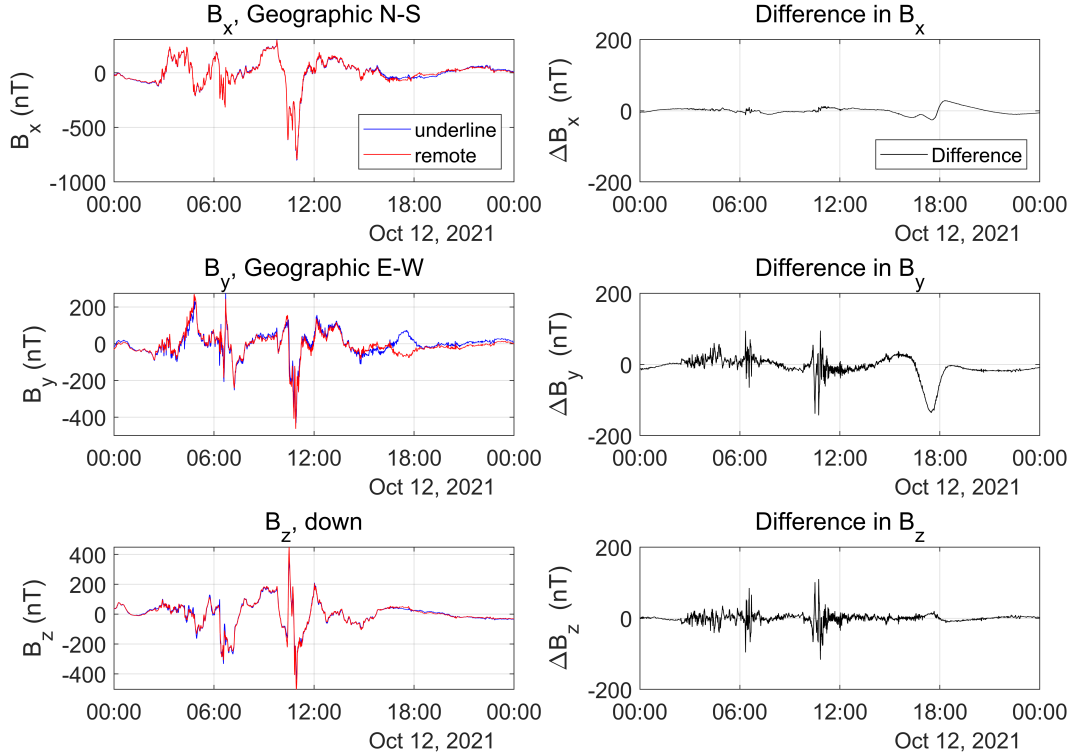


Figure 4.4: Magnetic field in geographic coordinates measured by the underline and remote sensors in each component (left) and the difference between the sensors in each component (right) on October 12th, 2021.

with the warming temperatures at sunrise (13:56 UTC) on this day. We conclude that this anomaly is due to the ground freezing and thawing underneath the DMM sensors causing a rotation and further misalignment between the two magnetometers; therefore, changing the amplitude of magnetic field data in each component. Fortunately, the temperature remains below zero degrees Celsius and the ground is frozen during the time of the geomagnetic activity providing stable magnetic field data for this time interval. The largest peak-to-peak amplitude of  $\Delta B_y$  during the first part of the geomagnetic storm at around 6:20 UT was 138 nT, and during the second part of the storm at around 10:45 UTC the peak-to-peak amplitude of  $\Delta B_y$  reached 238 nT. Similar peak-to-peak amplitudes are seen in  $\Delta B_z$ : 152 nT at 6:20 UTC and 226 nT at 10:45 UTC.

We now compare the times series of the magnetic data to the data from the transformer neutral-to-ground sensors. The 500 kV transmission line carries two 3-phase circuits for a total of six overhead wires carrying GIC. There are two transformers, one for each circuit, at the end of the power line each with a neutral-to-ground connection, referred to T1 and T2 in Figure 4.5. The neutral current measured at both ground connection points have similar amplitudes; therefore, the assumption of equal quasi-direct current in both power line circuits seems to hold. To simplify, the average of the neutral current from the two transformers is calculated and used for the following comparison against the DMM determined GIC estimate. We compare the average GIC through one circuit to half the total equivalent line current inferred using our DMM configuration assuming all the GIC in the line flows to the ground.

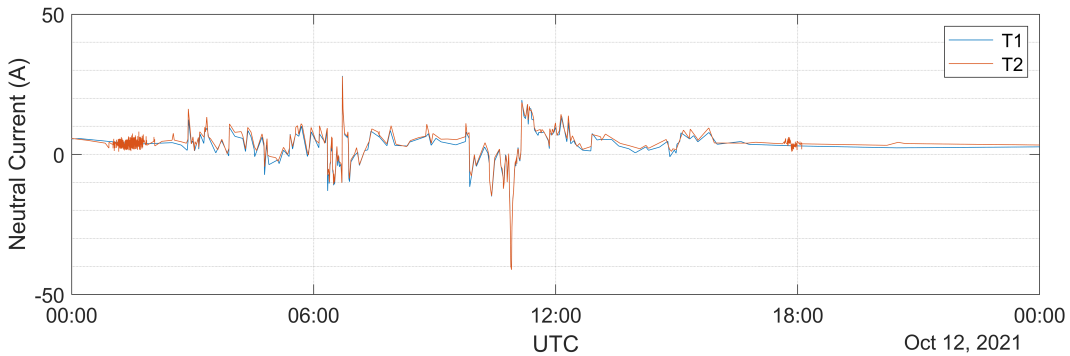


Figure 4.5: The transformer neutral-to-ground current measured on each circuit, T1 and T2, at Ellerslie substation on October 12th, 2021.

Following the methodology we provided in Chapter 3, we can derive two GIC estimates using the data in Figure 4.4 and compare it to the transformer GIC data in Figure 4.5. The two independent values of the inferred GIC,  $I(\Delta B_y)$  and  $I(\Delta B_z)$ , were hence computed using the steps outlined in Chapter 3. The inferred GIC is calculated independently from the y and z components, each providing an estimate of the GIC associated with each component of the magnetic field perpendicular to the direction of the current using equation 3.5 and 3.6. In Figure 4.6,  $I(\Delta B_y)$  and  $I(\Delta B_z)$  (top panel) are directly compared

to the neutral-to-ground current measured at Ellerslie transformer substation by AltaLink (bottom panel).

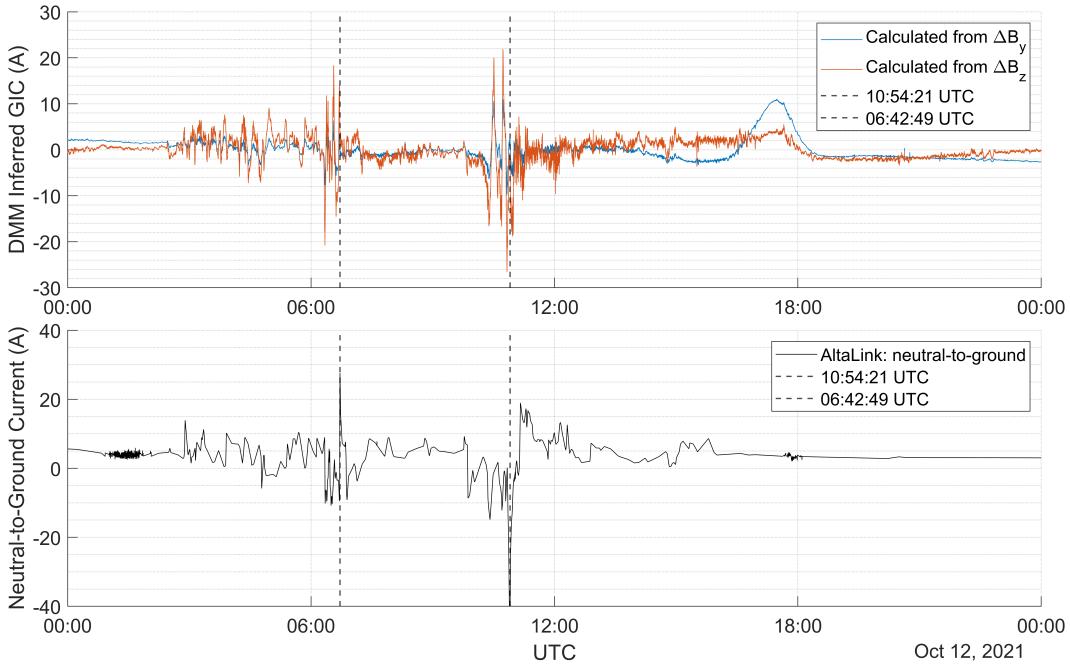


Figure 4.6: Two independent measurements for the inferred GIC calculated from each  $\Delta B_y$  and  $\Delta B_z$  components are plotted and compared to the neutral-to-ground current measurement at Ellerslie substation.

First, we compare the two DMM inferred GIC from each perpendicular component, y and z.  $I(\Delta B_y)$  and  $I(\Delta B_z)$  have excellent temporal and waveform correspondence specifically at the times of strongest geomagnetic activity, 3:00 to 14:00 UT. Between these hours, the linear correlation coefficient between the two time series is 0.89. The DMM inferred GIC calculated from the difference in the y component has a slightly smaller peak amplitude than that calculated from the difference in the z component; however, it is clear to see that the amplitude of the DMM inferred GIC agree within the error estimated for a GIC of 20 A. Therefore, it is determined that the discrepancy between the two DMM inferred GIC time series can be described by the errors introduced to the system during deployment and from assumptions made about the geometry of the power lines overhead. Further, we assume that the magnetic

signature of the GIC in the  $z$  component at the underline sensor is negligible since the GIC is estimated as an infinitely long single equivalent current directly above the underline sensor and therefore, by the right hand rule, all of  $d\mathbf{B}(t)$  is in the  $y$  component. Further, as already discussed in 3.4.3, sag in the power line is present as the underline sensor is deployed slightly displaced from the center point between the two pylons due to limitations during deployment. This challenges the infinitely long single equivalent current assumption for the GIC. Also, a single effective current is being estimated by DMM, and the height of the GIC is assumed from power line tower information provided by AltaLink and is taken to be the average height of the middle pair of wires at mid-span for the segment of the electricity transmission system we deployed under.

In the comparison between the  $I(\Delta B_y)$ ,  $I(\Delta B_z)$  and the industry GIC measurement, it is clear that the peaks in both detectors are contemporaneous. Clear peaks in the amplitude of the DMM inferred GIC are seen occurring at times of the maximum neutral-to-ground current observed at 6:42 UT and 10:54 UT, as indicated by the black dashed vertical lines in Figure 4.6. It is important to note that the under-sampled neutral-to-ground current data at Ellerslie substation fails to show some of the higher frequency information of the quasi-direct current flowing through the ground connection; therefore, this data set likely misses the true amplitude during times of greatest GIC activity, around 6:00 to 7:30 UT and 10:00 to 12:00 UT. Despite the low sample rate of the transformer neutral current data, the waveform and temporal correspondence of the GIC in the line inferred from the DMM method and transformer neutral-to-ground current measured by the the Hall probe are in good agreement. Further, their amplitudes are of the same magnitude: the maximum GIC amplitude estimated by the DMM method was 26 A, while the maximum GIC measured by the Hall probe at the transformer neutral-to-ground con-

nection was 41 A. A direct comparison of the current amplitudes is shown in Figure 4.7 which shows the neutral-to-ground current and inferred GIC determined from the difference in  $\Delta B_z$  overlaid on the same scale. In making this direct comparison we are also assuming that, at the termination of the line at Ellerslie substation, all the GIC is returned to ground which appears to be a good approximation. The discrepancy between the DMM inferred GIC measurement and that from the transformer neutral-to-ground can only be partly attributed to the positional uncertainties and sensor misalignment described in Section 3.4.3. Elements not considered in the error estimate previously and must be accounted for are the geoelectric field associated with the GIC in the Earth, and importantly, the grid topology and resistances of the transformers and power lines (e.g., *Hübert et al.*, 2020). The latter of which we do not have information from industry. These elements may play an important role in determining the true amplitude of the GIC flowing up through the neutral-to-ground connection and subsequently the transformer and power line; however, we are limited by the knowledge available to use by the power industry.

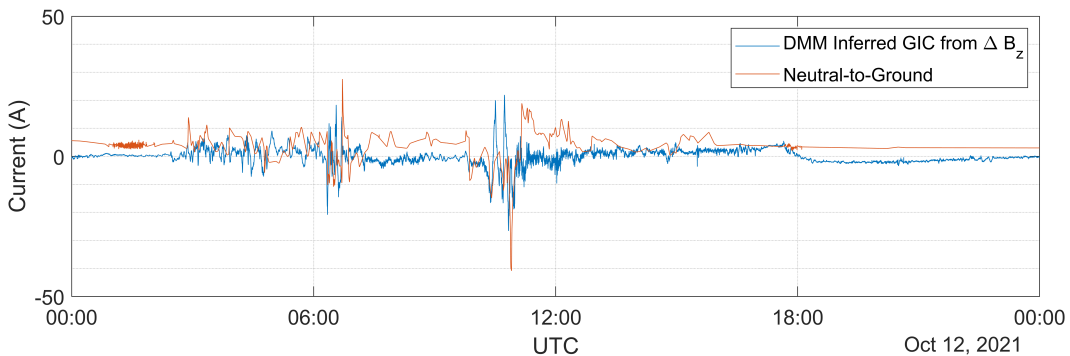


Figure 4.7: A direct comparison between the inferred current calculated using DMM from  $\Delta B_z$  and the neutral-to-ground current measurement at Ellerslie substation.

## Estimating GMD using DMM

Lastly, the background GMD can be calculated from equations 3.7 and 3.8. The magnetic field produced by the GIC is identified for each component, and the background GMD is determined by subtracting the field inferred to be related to the GIC in the power line from the total field measured for each component. This is shown in Figure 4.8 in comparison to the magnetic field measured at MSTK station in the y and z components. Figure 4.8 also shows excellent linear correlation between the magnetic field measured at MSTK and each  $B_{0,x}$ ,  $B_{0,y}$ , and  $B_{0,z}$  determined using the differential measurements. For each component, x, y, and z, the linear correlation coefficient is determined to be  $R = 0.990$ ,  $R = 0.944$  and  $R = 0.972$ , respectively. This is strong evidence again for validating the success of the new DMM method in separating the GMD from the magnetic perturbations associated with GIC. Two important points should be considered when accounting for the difference between the two measurements. Firstly, the assumption that the GMD is spatially uniform over a distance of 48 km, and secondly, there are discrepancies due to issues in proper base lining which are a result of the relative instability of the data collected at the DMM sensors. There appears to be signatures at MSTK which are not captured by the DMM and/or vice versa. Therefore, even though we have demonstrated MSTK is a good proxy for GMD strength and there is great correspondence between the data sets, the small differences between two magnetometer measurements can of course affect the magnitude of GIC values estimated by the DMM method meaning MSTK station is too far away from the DMM site to be used as a true base station.

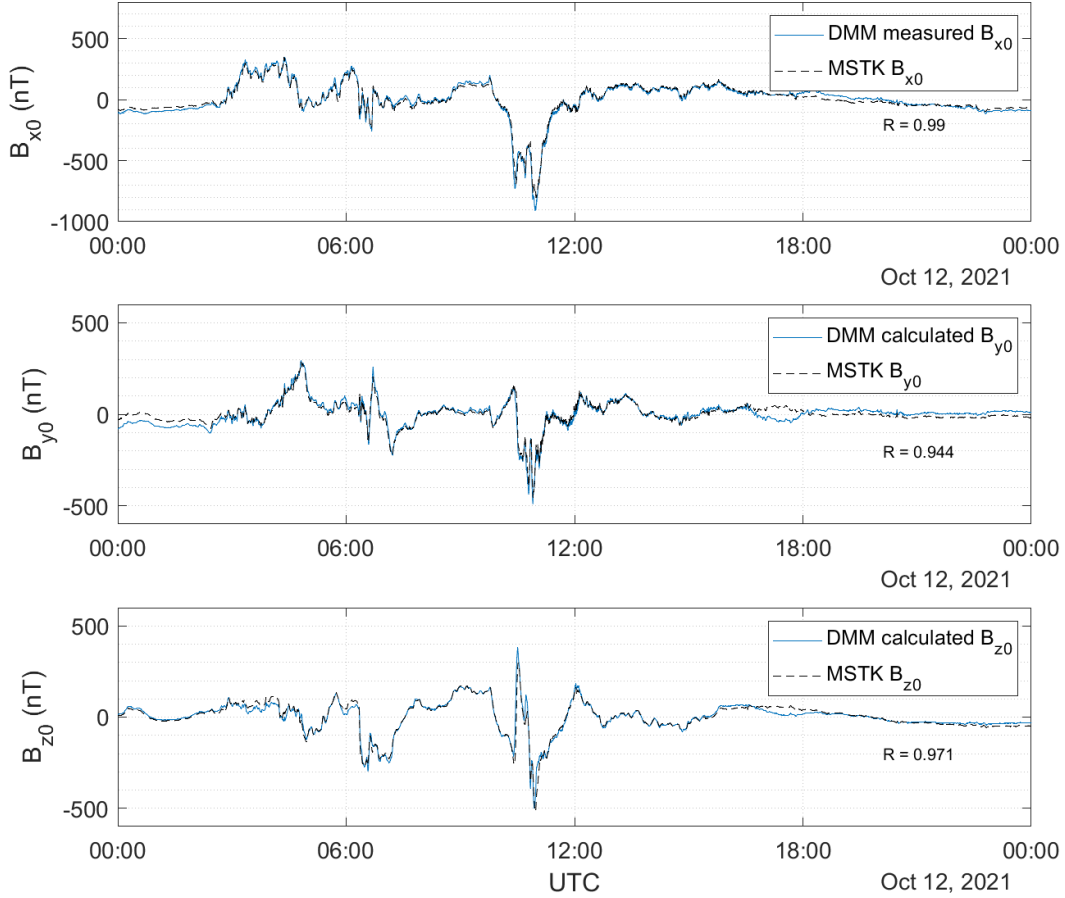


Figure 4.8: The background magnetic field determined using the DMM method is plotted in the x, y and z components. MSTK station magnetic field is also plotted in each component for comparison.

## 4.4 Discussion and Conclusions

In this chapter, we presented results derived from the deployment of a new DMM system where the two DMM magnetometers are placed closer together than in the traditional DMM setup. In this new configuration, both DMM magnetometers are now able to measure the magnetic field variations due to the GIC flowing through the overhead power line. Using the known geometry of the DMM set up, including the distance between the two sensors, and the distances between each sensor and the transmission lines overhead, we have demonstrated how we were able to separate the two sources contributing to the total field measured by each DMM sensor: the magnetic field associated

with the GIC flowing through the power line and the background GMD. The major advantage of this new method is that we can compute two independent values for the inferred GIC from the difference in each of the magnetic y and z components separately; therefore, as we have shown, through a comparison of the two DMM inferred GIC we confirmed the amplitude difference between the two estimates were attributed to the sources of error presented in Section 3.4.3 further demonstrating the intercalibration between the two DMM sensors. Also, we validated the temporal correspondence and magnitude of the two GIC estimates from DMM against the neutral-to-ground current measured by AltaLink.

Our new DMM system was deployed under a high voltage power line in central Alberta, Canada where there were two existing neutral-to-ground current measurements, one at each end of the respective power line segment. A comparative analysis of a geomagnetically quiet day provided an assessment of the errors associated with the DMM method and validates the intercalibration of the two DMM sensors and which is essential for the successful application of the DMM technique. Environmental factors, such as heating and cooling causing expansion of the soil beneath the sensors due to sunlight resulted in  $\Delta B_y$  reaching a maximum of 20 nT in the y component. The mean deviation from the median was 1.6 nT, 2.8 nT, and 0.7 nT in the x, y and z components, respectively, which is well within the errors of the system listed in Section 3.4.3. Specifically, this sets a baseline error for analyzing a moderate geomagnetic storm on October 12th, 2021. Using transformer neutral-to-ground current data collected by a Hall effect sensor deployed by AltaLink at the Ellerslie transformer substation, we validated the new DMM method by comparing the measured GIC from the Hall probe to our GIC derived using DMM during a moderate geomagnetic storm on October 12th, 2021. Although the Hall sensor GIC data is under-sampled, we demonstrate an excellent temporal correspon-

dence between the data from the Hall probe at Ellerslie substation and that from our measurement. In particular, we see contemporaneous peaks in both GIC measurements at 6:42:49 UT and 10:54:21 UT. The peak GIC flowing through the ground connection for each circuit, i.e. each transformer, is 40.8 A. This is a significant GIC value, but it is not near the threshold defined by NERC to be a GIC of concern at 75 A per phase (*NERC*, 2020). The maximum GIC values estimated using the DMM approach was 26 A. This discrepancy between the inferred GIC and the neutral-to-ground measurement can be accounted for by the misalignment and positional uncertainty introduced to the system during deployment, and the unknown resistances of the transformer and the power line itself. Missing information about the resistance parameters of the power network limits a complete comparison and is noted. However, using the new DMM approach, we achieved an improved agreement between amplitudes of the DMM GIC estimate and the industry GIC measurements than that which was determined by *Hübert et al.* (2020) on the UK power grid, where the difference in amplitude between the two GIC values was over an order of magnitude.

Further, we compared the DMM background magnetic field to the magnetic field measured at the nearby MSTK CARISMA station and see a strong correlation. We see a significant difference during large GMD which suggests large background GMD includes smaller scale currents which generates GMD with slightly varying amplitudes between MSTK station and DMM location. The background field determined at both locations has correlation coefficients greater than 0.94 in each component for the entire day. However, as the DMM results presented above show, we know small differences between two magnetometer measurements can have a significant affect on the magnitude of GIC values estimated using the DMM method; therefore, MSTK station is too far away from the DMM site to be used as a true base station or an effective third

DMM sensor, but can be used as a proxy for the driving GMD of GIC in the electrical power system. Also, this further suggests that the equations derived in Chapter 3 properly separates the two magnetic field sources measured by the DMM sensors and supports our conclusions above for the GIC determined using the new DMM method. Overall, the strengths of the new DMM method have been demonstrated by following results presented in this chapter:

- validated large  $\Delta B$ , and GIC, come from periods of large GMD
- validated independent estimates of GIC from  $\Delta B_y$  and  $\Delta B_z$  separately
- demonstrated temporal and waveform correspondence of the DMM inferred GIC and the transformer neutral-to-ground current
- estimated GIC magnitude using DMM is of the same order as the transformer neutral-to-ground current
- validated success of the DMM inferred GIC by showing the background GMD,  $B_0$ , agrees with the magnetic field at MSTK station

In the future, we recommend augmenting this DMM approach to include a third DMM sensor as a local base station, at approximately 200 m, while keeping the underline and intermediate magnetometers at the locations demonstrated in our design. This would be a similar approach to *Hübert et al. (2020)* and *Matandirotya et al. (2016)*, but would maintain the benefits of measuring two independent GIC estimates. Further improvements to the DMM system in the future will be to increase the stability of the sensors against environmental factors, including the freeze-thaw cycle. A suggestion for future work is, from the geometry, resolve the contributing factor of the GIC flowing in each wire to the total GIC magnetic perturbation measured at each sensor. This should be done to test the validity of the assumption that, by the principle of superposition, the GIC flowing through each phase is 1/6th the total GIC travelling

through the power line system overhead. This is also important to determine for the case where there is an unequal current distribution between the two circuits, which is possible since each transformer operates independently. Further comparison to an indirect measure of GIC is examined in the next chapter. We will examine the induced geoelectric fields determined using GMD data from MSTK and the surface impedance and show a direct comparison to the GIC measured at the neutral-to-ground connection for multiple geomagnetic events during the past year.

# Chapter 5

## Direct Comparisons Between an Estimated Geoelectric Field and the Power Grid Response during Recent Geomagnetic Events

### 5.1 Introduction

Geomagnetic storms can induce an electric field which can drive electrical currents in conducting paths on Earth, including Earth's crust and other conducting paths such as long distance electrical power distribution lines. The ground conductance also affects the electric fields at the Earth's surface, affecting the size of the fields and their impacts as they couple into electrical power networks, potentially causing interference to the system's performance and possible damage for example through transformer heating or affecting the phase of the power system (*Molinski, 2002*) (see Chapter 1). Appropriate consideration of the role of the Earth's conductivity structure is crucial for developing an accurate understanding of the inductive response for GIC hazard assessments. The fundamental theory of geomagnetic induction has been understood since the early work of *Cagniard (1953)*, *Price (2002)*, and *Wait (1962)* (see also e.g., the review in *Boteler, 1994*). In this chapter, we ap-

ply the mathematical approach and concepts from the geophysical discipline of magnetotellurics (e.g., *Chave and Jones, 2012; Simpson and Bahr, 2005; Pirjola, 2002*), as described earlier in Section 1.3.2 and further discussed in Section 5.2, to study the generation and impacts of the induced geoelectric field due to GMD as it relates to GIC hazards on the electrical power system.

The amplitude, phase and polarization of the induced electric field can be altered or distorted by the three-dimensional conductivity structure of the Earth (e.g., *Love et al., 2022*). Recent studies have proven the utility and importance of using the 3-D surface impedance to estimate the geoelectric field, highlighting the importance of not only the geomagnetic conditions but also the Earth’s crustal conductivity structures for producing GIC and therefore assessing risk to electrical power systems (e.g., *Bedrosian and Love, 2015; Cuttler et al., 2018; McKay and Whaler, 2006; Zheng et al., 2013; Cordell et al., 2021*). In particular, *Cordell et al. (2021)* highlights the importance of using 3-D impedance datasets at locations where the subsurface geology contains a discontinuity in the conductivity structure. Such structures can have a profound effect in the amplitude and polarization of the induced geoelectric field. Introduced and defined in Section 1.3.2, the impedance tensor,  $\mathbf{Z}(\omega)$ , is a frequency-dependent complex tensor which describes the ability of the Earth’s crust to conduct current.  $Z$  is defined as the ratio between the horizontal electric and magnetic fields measured during magnetotelluric surveys, and is defined in the frequency domain by the following, where  $\mathbf{E}(\omega)$  has units V/m,  $\mathbf{Z}(\omega)$  has units of Ohms, and  $\mathbf{B}(\omega)$  has units of T:

$$\mathbf{E}(\omega) = \frac{1}{\mu_0} \mathbf{Z}(\omega) \mathbf{B}(\omega). \quad (5.1)$$

In the work to be presented here, the geoelectric field is calculated by a convolution between the spectral content of the geomagnetic field,  $\mathbf{B}(\omega)$ , derived from the time series data at the CARISMA MSTK station, and the transfer

function,  $\frac{1}{\mu_0}\mathbf{Z}(\omega)$ , where  $\mathbf{Z}(\omega)$  has been previously determined from MT measurements collected by the University of Alberta geophysics group led by Prof. Martyn Unsworth. Note that each must be taken to connect the appropriate components of  $\mathbf{E}(\omega)$  and  $\mathbf{B}(\omega)$ , as shown below in equations 5.2 - 5.4.

The impedance varies depending on the rock properties, including mineralogy, temperature, and fluid content (e.g., *Love et al.*, 2022, and references therein). Most of the province of Alberta is characterized by a conductive sedimentary basin. In North-East Alberta, the conductive sedimentary rock meets the much more resistive crystalline igneous rock of the Canadian Shield resulting in a large conductivity gradient; therefore, increasing GIC risks due to strong geomagnetic induction in this region (*Cordell et al.*, 2021). For the location of this study, and where we have used data for the MSTK station in the CARISMA network at 53.351°N and 112.974°W, the 3-D impedance tensor is relatively uniform. This offers an opportunity to assess the direct impact of the horizontal geoelectric field components across the length of a specific power line segment.

In this chapter, we directly compare the calculated geoelectric field derived from GMD measured at MSTK station to the neutral-to-ground current measured at the transformer substation at Eilerslie and discuss the spatial and frequency variations of the source GMD and the impedance transfer function. In particular, we investigate whether the frequency dependent response of the electric field are dominated by the frequency dependence of the impedance tensor or the driving GMD magnetic field due to space weather, or a combination of both, and under what conditions would the latter apply. As suggested in *Love et al.* (2022, and references therein), the affect of the latitudinal dependence of the GMD is seen to be much weaker than the location specific geographic variations due to surface impedance. This has very important implications about the significance of conductivity structure in Earth's sub-

surface for determining the strength of the coupling of GMD into resulting GIC flowing through our electrical power network.

## 5.2 Data and Methodology

Three dimensional surface impedance data for locations in Alberta were provided by Darcy Cordell, and collected by Prof. Martyn Unsworth and his geophysics group at the University of Alberta. The impedance tensors were calculated from MT data collected at locations across the province over many years of surveys. For this analysis, we use the impedance tensor matrix defined near the CARISMA magnetometer station at Ministik Lake at geographic latitude and longitude  $53.351^\circ\text{N}$  and  $112.974^\circ\text{W}$ , respectively.

Results in the following section show the geoelectric field calculated using the magnetotelluric method based on the vector  $\mathbf{B}$ . We move forward with the assumptions listed in Section 1.3.2 which is standard for the application of magnetotellurics in similar analyses determining the geoelectric field by this method (e.g., *Campanyà et al.*, 2019, and references therein). We calculate the electric field in the frequency domain through the convolution of the spectrum of the geomagnetic field,  $\mathbf{B}(\omega)$  with the magnetotelluric impedance tensor,  $\mathbf{Z}(\omega)$ , times a factor of  $\frac{1}{\mu_0}$ , where  $\mu_0$  is the magnetic permeability of free space.  $\frac{1}{\mu_0}\mathbf{Z}(\omega)$  will be hereby referred to as the transfer function and is given in units mV/km/nT (e.g., *Boteler*, 1994). The surface impedance is expressed as a  $2 \times 2$  complex tensor and is expressed in matrix form:

$$\begin{bmatrix} E_x \\ E_y \end{bmatrix} = \frac{1}{\mu_0} \begin{bmatrix} Z_{xx} & Z_{xy} \\ Z_{yx} & Z_{yy} \end{bmatrix} \begin{bmatrix} B_x \\ B_y \end{bmatrix}. \quad (5.2)$$

Expanding this matrix we obtain,

$$E_x = \frac{1}{\mu_0}(Z_{xx}B_x + Z_{xy}B_y) \quad (5.3)$$

$$E_y = \frac{1}{\mu_0}(Z_{yx}B_x + Z_{yy}B_y). \quad (5.4)$$

For the 1-D Earth model, where the conductivity only varies with depth, the diagonal elements,  $Z_{xx}$  and  $Z_{yy}$ , are equal to zero and the off diagonal elements have the same magnitude, but have different signs; therefore, in the frequency domain the geoelectric field will be orthogonal to the variable magnetic field. The 2-D case is used to model a conductive discontinuity in a single horizontal direction, like a geological fault. In this case,  $Z_{xx}$  and  $Z_{yy}$  are again equal to zero and the off diagonal elements,  $Z_{xy}$  and  $Z_{yx}$ , are of different magnitudes defined by the E-polarized (TE) and B-polarized (TM) transverse modes, respectively. The TE mode corresponds to the E-field being polarized parallel to strike direction, and analogously, the TM mode corresponds to the B-field being polarized parallel to the strike direction (Naidu, 2012). Lastly, in the 3-D Earth case where the conductivity varies with depth and in both horizontal directions, x and y, the impedance matrix is no longer symmetric and depends on the proximity to different conductive regions. Each element of the impedance tensor is defined as  $Z_{i,j} = \frac{E_i}{B_j}$ , where  $i, j = x, y$ , and is determined independently using MT sounding data. Where the diagonal components of the impedance tensor ( $Z_{xx}$  and  $Z_{yy}$ ) are very small, this is an indication that the conductivity distribution of the subsurface is close to 1-D Earth case. Conversely, if  $Z_{xx}$  and  $Z_{yy}$  are larger this indicates the conductivity has a more three dimensional distribution.

The steps taken to calculate the time series of the geoelectric field during a geomagnetic event are shown by equations 5.5 to 5.7. First, a fast Fourier Transform ( $\mathcal{F}$ ) is applied to the time series magnetic field data. The geoelectric field in the frequency domain is calculated from the convolution between the magnetic field in the frequency domain and the transfer function containing the frequency-dependent impedance tensor determined by MT. Finally, an inverse fast Fourier Transform of the frequency domain geoelectric field is done to

obtain the time domain geoelectric field.

$$B_{y,x}(\omega) = \mathcal{F}\{B_{y,x}(t)\} \quad (5.5)$$

$$E_{x,y}(\omega) = \frac{1}{\mu_0} Z(\omega) B_{y,x}(\omega) \quad (5.6)$$

$$E_{x,y}(t) = \mathcal{F}^{-1}\{E_{x,y}(\omega)\} \quad (5.7)$$

Realistic estimates of the geoelectric field in the horizontal components as a function of time,  $E_x(t)$  and  $E_y(t)$ , is obtained and directly compared to neutral-to-ground current data for recent moderate geomagnetic storms. Case studies of three geomagnetic events on October 12th, 2021, November 4th, 2021, and February 3rd, 2022 are shown in Figures 5.6, 5.7, and 5.8. The geoelectric field is obtained using the magnetic field and surface impedance data at Ministik Lake. The neutral current data is provided by AltaLink from Ellerslie substation. MSTK station and Ellerslie substation are located approximately 33.5 km apart. Neutral current data from the first event, October 12th, 2021, was collected by AltaLink during the commissioning phase of the deployment of the Hall effect sensors. For this event, the data samples are not constantly spaced in time; however, in the subsequent events, the data capture is improved.

Further, analysis on the level of agreement between the geoelectric field and the resulting GIC is done with the current data collected for the largest GIC event captured on November 4th, 2021. On this day the Hall effect sensor recorded data with two second cadence. A linear correlation between the calculated horizontal geoelectric fields and the transformer neutral-to-ground current is calculated during each two hour interval for the November 4th, 2021 event (see Figure 5.9). To further examine the correlation between the E-field and the transformer neutral-to-ground current, we examine the estimated combined E-field along the length of the power line as defined by the geometric configuration the local N-S and E-W segments of the power line: where 74% is

in the N-S direction, and 26% is in the E-W direction. This particular power line segment extends from Ellerslie substation, south of Edmonton, Alberta, to Heartland substation, near Fort Saskatchewan, Alberta, as seen in Figure 5.1. We approximate the power line as being comprised of two major sections: starting at Ellerslie substation the approximated transmission line travels 16.5 km East and 46.5 km North, respectively. We assess the roles of  $\mathbf{B}(\omega)$  and  $\mathbf{Z}(\omega)$  as potentially dominant driving elements of the GIC through the convolution of  $\mathbf{B}(\omega)$  with the impedance transfer function in terms of frequency and direction, as well as comment on the spatial scale of the local GMD and its potential effect on the induced current in the power line.

## 5.3 Results and Discussion

### 5.3.1 Spatial and Frequency Dependence of MT Transfer Functions

To investigate the spatial and frequency dependence of the calculated geoelectric field, we first examine the variation of the amplitude and polarization of the magnetotelluric transfer functions. Figure 5.2 is taken from *Love et al. (2022)* and shows the transfer function amplitude and polarization as ellipsis for a discrete set of frequencies from  $10^{-4}$  to  $10^{-1}$  Hz at 1253 MT survey sites across the contiguous United States. Here, *Love et al. (2022)* follows the mathematical approach described in *Berdichevsky and Dmitriev (2008, Section 1.4.2 and Equation 1.91)* to calculate and plot the E-polarized impedance,  $Z_E$ , for period variations at (a) 120 s and (b) 1200 s. The radius and colour of the ellipse illustrates the amplitude of the transfer function, and the azimuthal angle of the ellipse illustrates the polarization of the geoelectric field, which ultimately is dependent on the polarization of the variable magnetic field (*Berdichevsky and Dmitriev, 2008*). It is important to note, for the polarization solution a  $90^\circ$  ambiguity exists, so the polarization is either parallel or perpendicular

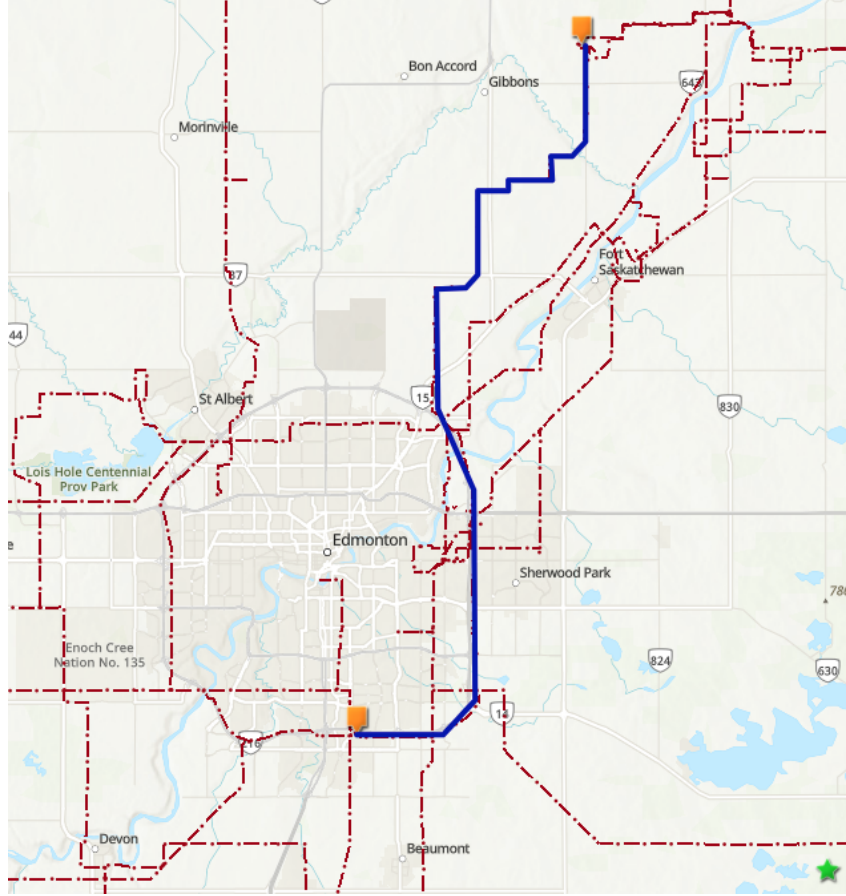


Figure 5.1: A map of the main power lines around Edmonton and surrounding areas shows the location of the 500 kV power line (blue), the transformer neutral-to-ground current measurements at Ellerslie and Heartland substations (orange squares), and the CARISMA station at MSTK (green star). The map was created using ESRI ArcGIC software (ESRI Basemap: Topographic (2013); Government of Alberta: Powerline, utility\_access (2021); H.Parry: Power Lines and Magnetometer Locations (2021)).

to the semi-major axis of the ellipse. More information on the subsurface geology at each site is needed to resolve this. From this map, it is evident that regions of high amplitude are highly polarized and analogously, regions with low amplitude are not strongly polarized (*Love et al., 2022*). Figure 5.2 also illustrates the geological boundaries between conductivity structures and its relation to the transfer function amplitude. In particular, a conductivity gradient is visible between regions of electrically resistive rock near the great lakes (high transfer function amplitude and more polarized) and regions com-

posed of conductive rock to the west, in North Dakota and South Dakota, and the Eastern portion of Montana (low transfer function amplitude and less polarized).

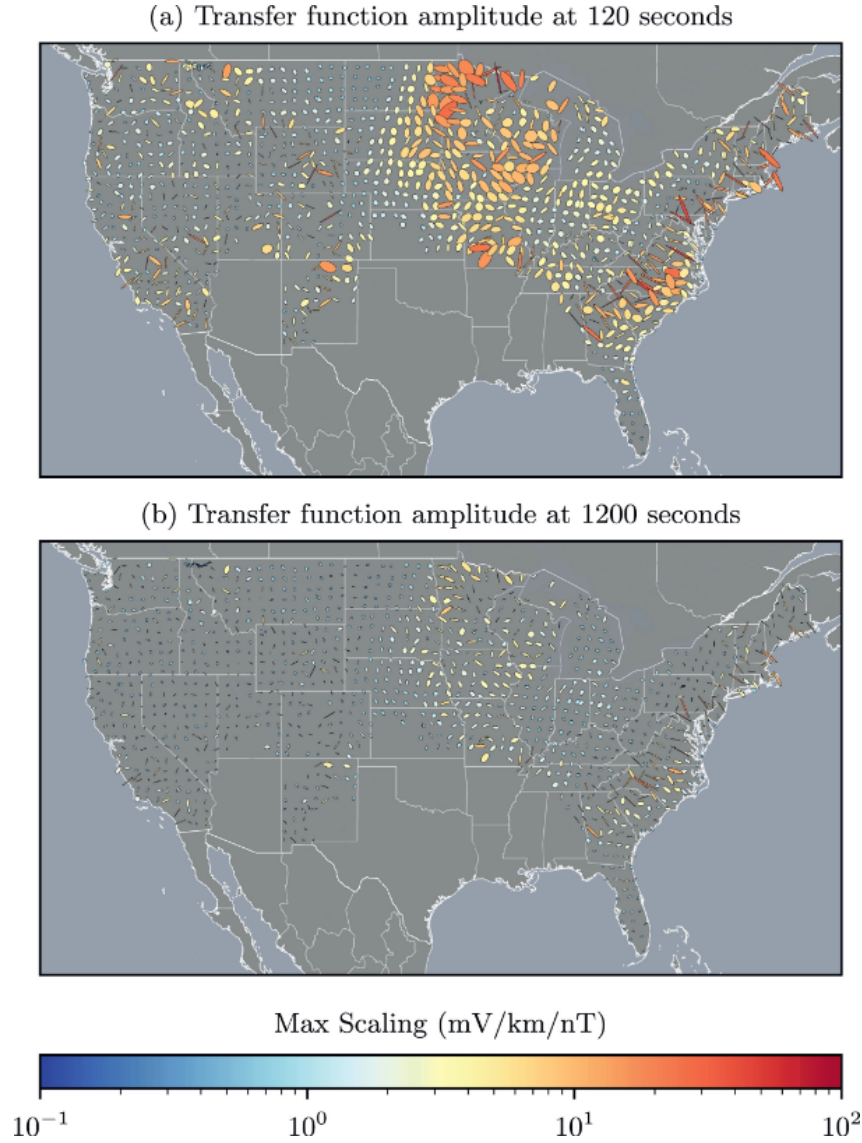


Figure 5.2: From *Love et al.* (2022), the amplitude of the long-period impedance transfer function,  $\frac{Z}{\mu_0}$  (mV/km/nT), at each magnetotelluric survey site in the continental United States is plotted as a function of the geoelectric polarization for two discrete periods: (top panel) 120 s and (bottom panel) 1200 s.

We repeat the same analysis for Alberta (Figure 5.3, courtesy of Darcy Cordell), and see a similar result in the majority of the province to that of

the North-central US as expected since they share a region of conductive sedimentary basin rock. In Figure 5.3 variations at 130 s (left) and 1300 s (right) are shown. Although MT data coverage is relatively poor in the North-East part of the province, a steep conductivity gradient can still be seen around Fort McMurray (indicated by the black circle). Four of the top ten maximum impedance amplitudes in Alberta occur at MT sites around Fort McMurray with maximum amplitudes of approximately 10 mV/km/nT at a 130 s period. Large amplitudes are also seen in the central West portion of the province, near the towns of Jasper and Hinton in the Rocky Mountains. Overall, the direction for the impedance is roughly NW-SE across much of the province which is in agreement with *Cordell et al.* (2021). Near Edmonton (indicated by the black triangle), the maximum amplitude is very low, approximately 1 mV/km/nT at 130 s period. For longer period variations, e.g. at 1300 s, the transfer function amplitudes are lower. Note the difference in scale between the two panels. The maximum-to-minimum ratio measured across the US is 546 (*Love et al.*, 2022). This is a substantial variation in the impedance tensor highlighting its contribution to the generation of large amplitude geoelectric fields. In Alberta, a much smaller geographic region, we might expect the impedance variation to be smaller. At 130 s and at 1300 s, the maximum-to-minimum ratio is approximately 10. This is much smaller, but still significant when we examine the spatial variation of impedance across the length of a long transmission line. Again, this emphasizes at both short and long periods, the induced geoelectric field is strongly dependent on the amplitude of the frequency-dependent impedance which changes by at least an order of magnitude across the province. This agrees with *Love et al.* (2022), who concluded that the magnitudes of the E-fields are more dependent on the frequency response and the variation of the amplitude of Z and that it is the spatial variation of the impedance that can dominate over the latitudinal variation of dB

in the generation of GIC in electrical power systems.

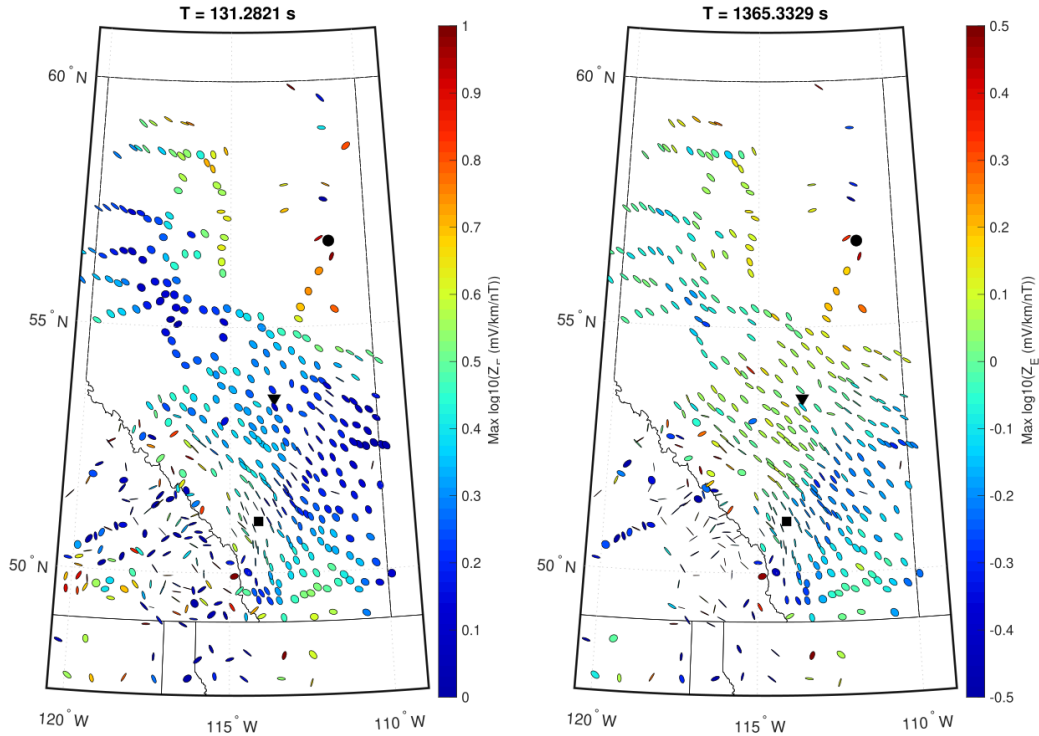


Figure 5.3: The impedance transfer function,  $\frac{Z}{\mu_0}$  (mV/km/nT), at each magnetotelluric survey site in Alberta is plotted as a function of the geoelectric polarization for two discrete periods: (left panel) 130 s and (right panel) 1300 s. Note the different scale for the impedance amplitude for each frequency [Courtesy of Darcy Cordell, after *Love et al.* (2022)].

The impedance calculated at MSTK, for a set of discrete frequencies between  $10^{-4}$  to  $10^{-1}$  Hz, is interpolated onto the same set of frequencies as the B-field. Figure 5.4 plots the interpolated real and imaginary parts of each impedance matrix element. In both the real and imaginary parts, the impedance values are small, on the order of  $10^{-3}$  Ohms. The impedance tensor at MSTK is also nearly 1-D, since the diagonal elements,  $Z_{xx}$  and  $Z_{yy}$ , are very small and the off-diagonal elements are nearly the same magnitude and are of opposite sign. The matrix elements plotted here will be used in the convolution with the magnetic field measured at the MSTK location to obtain

an estimate for the geoelectric field.

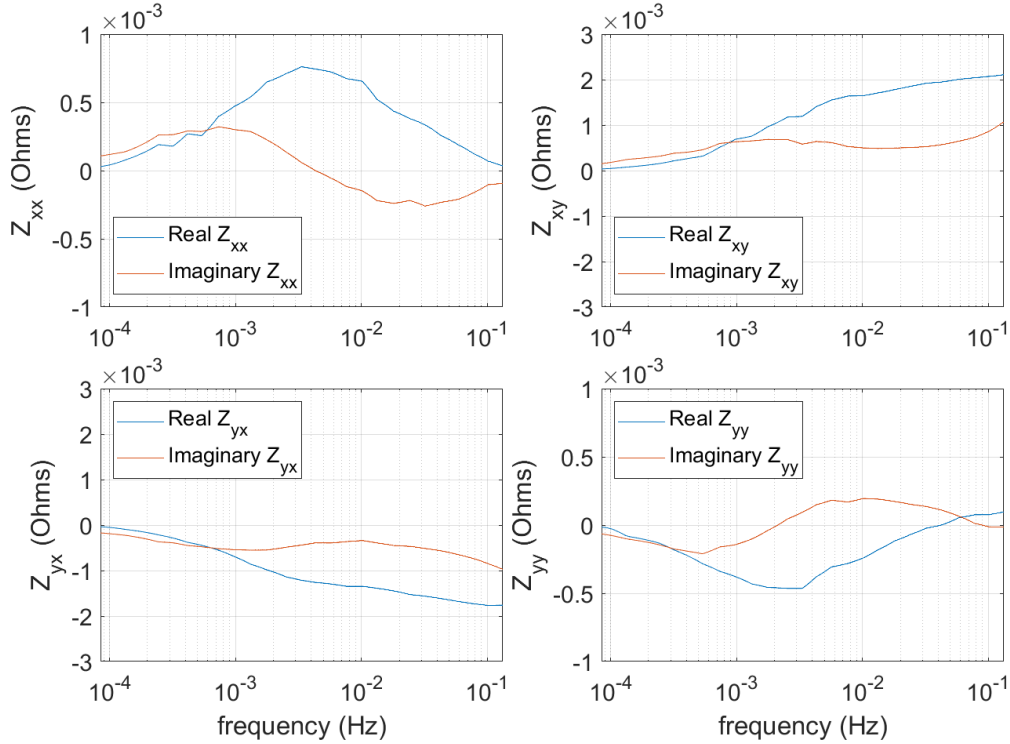


Figure 5.4: The amplitude of each real and imaginary component of the three dimensional complex impedance tensor,  $xx$ ,  $xy$ ,  $yx$ , and  $yy$ , at Ministik Lake is plotted in the frequency band from  $10^{-4}$  to  $10^{-1}$  Hz.

In Figure 5.5, the source magnetic fields from MSTK and the resulting E-field in the frequency domain from the convolution in Equation 5.2 are shown for the events on November 4th, 2021. These values were computed using the built-in unwindowed FFT function using MATLAB software. Here, the characteristic drop off in the magnetic field amplitude with frequency for geomagnetic field variations is seen in the top left and right panels,  $B_x(\omega)$  and  $B_y(\omega)$ , respectively, across the frequency band from 0 – 0.12 Hz. The resulting spectra of the E-field derived using  $\mathbf{Z}(\omega)$  and the MT method are plotted in the bottom left and right panels,  $E_y(\omega)$  and  $E_x(\omega)$ , respectively, and show similar spectral shape to that of the magnetic field over the same frequency range. The amplitude of the spectral density of the electric field decreases from  $10^6$

to  $10^2$  mV/km/Hz. This is expected due to the impedance at this location being approximately one dimensional with a small amplitude, around  $10^{-3}$  Ohms; therefore, suggesting that a region with higher impedance amplitude at a range of frequencies would result in significant spectral components at these frequencies.

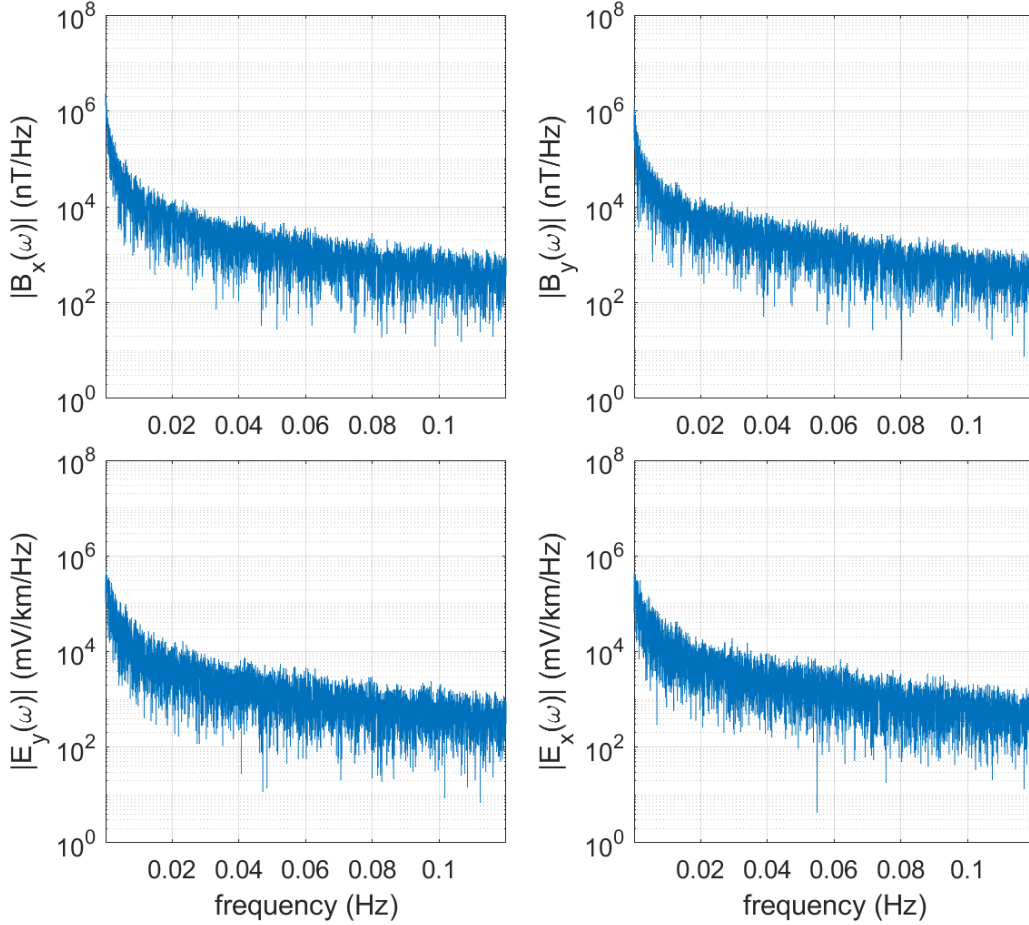


Figure 5.5: Electromagnetic field spectra are plotted in the frequency domain for the whole frequency range of Z,  $10^{-4}$  to  $10^{-1}$  Hz derived from MSTK on November 4th, 2021: (top row) the frequency spectrum of the Northward (left) and Eastward (right) components of the magnetic field in nT,  $B_x(\omega)$  and  $B_y(\omega)$ , and (bottom row) the frequency spectrum of the Eastward (left) and Northward (right) geoelectric field in mV/km,  $E_y(\omega)$  and  $E_x(\omega)$ .

From this analysis, we can state that the amount of  $E_x$  and  $E_y$  generated from  $B_y$  and  $B_x$  is dependent on a combination of the variation of the magnetic field is in each and, importantly, what the transfer function looks like at

different frequencies. A portion of each  $B_x$  and  $B_y$  may add to both  $E_x$  and  $E_y$  depending on the characteristics of the tensor. The magnitude of each is dependent on the crustal geology, so the transfer from B to E may be weak in some locations and in other regions it may be much stronger. In the region near Edmonton, the impedance transfer function is weak across a large range of frequencies (see Figure 5.4) and polarized in the NW-SE direction (see Figure 5.3). It can also be seen that both the real and imaginary parts of the impedance tensor elements vary smoothly over the frequency range from  $10^{-4}$  to  $10^{-1}$  Hz. This implies that at this location, where the impedance tensor is relatively constant and resemblant of a 1-D crustal conductivity structure, the frequencies of the derived electric field is dominated by the frequencies of the GMD. The impedance tensor does not have a significant frequency dependence, but holds specific consequence regarding the amplitude of the resulting geoelectric field and the induction of GIC in the electrical power system.

To investigate this further we examine data from a specific point in the electrical power network in central Alberta using transformer neutral-to-ground Hall probe data from Ellerslie substation, and compare this against the estimated time-domain geoelectric field to test if we can verify GIC in the power line using the convolution of measured GMD and the impedance tensor.

### 5.3.2 Derived Geoelectric Field Comparison to GIC

We investigate the relationship between the derived geoelectric field time series and the measured GIC from the transformer neutral-to-ground at Ellerslie substation in the electrical power network during three geomagnetic events in the past year: October 12th, 2021, November 4th, 2021, and February 3rd, 2022. As outlined in Section 5.2, the geoelectric field in the time domain is calculated by convolving the frequency dependent impedance transfer function with the measured magnetic field from MSTK in the frequency domain. The

inverse fast Fourier transform is performed to obtain the time variation of the electric field. The horizontal geoelectric field components are plotted and directly compared to the transformer neutral-to-ground current measured at Ellerslie substation for these three events in Figures 5.6, 5.7, and 5.8.

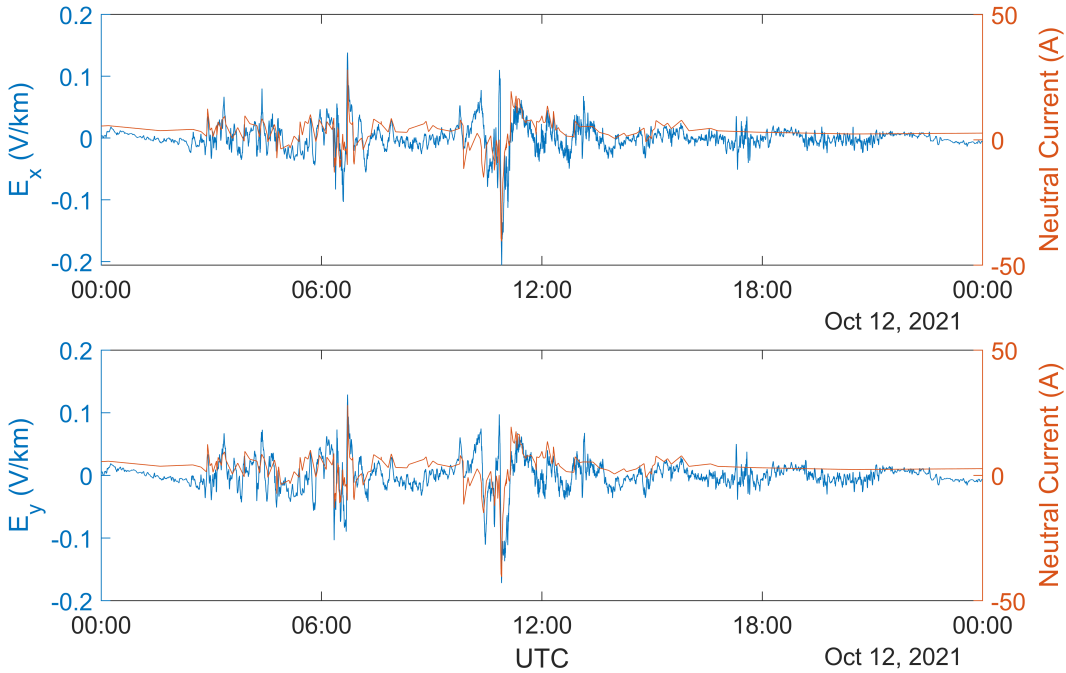


Figure 5.6: Comparison between the horizontal geoelectric field in V/km at MSTK magnetometer station (blue) and the transformer neutral-to-ground current in Amps at Ellerslie substation (orange) on October 12th, 2021.

The plotted transformer neutral-to-ground current is that which travels through one circuit which has 3 phases. A grounding connection exists for each circuit, i.e each transformer. A single circuit is comprised of three wires, each wire carries a current with a phase difference of  $120^\circ$  from the others; therefore, the Hall probe GIC is divided between the three phases. It is important to note that the benchmark for an event of concern in the power network, as defined by NERC, is a GIC of 75 A per phase, i.e 75 A through each of the 3 wires in a single 3-phase circuit like that with which we study here. The current measured at the transformer neutral-to-ground is the combined GIC flowing through all three phase.

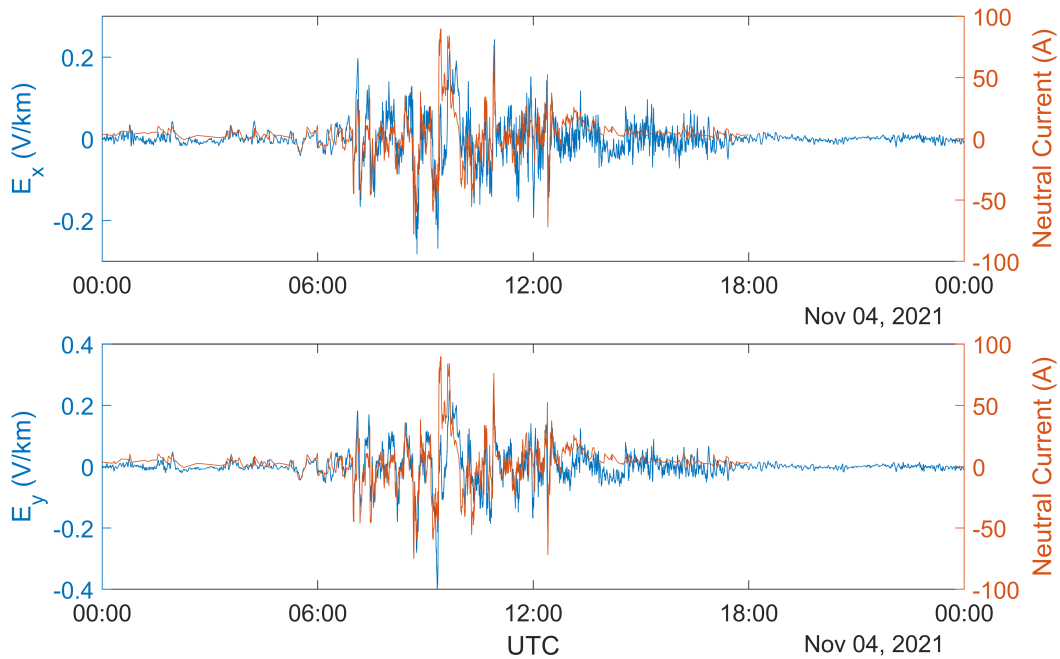


Figure 5.7: Comparison between the horizontal geoelectric field in V/km at MSTK magnetometer station (blue) and the transformer neutral-to-ground current with improved resolution in Amps at Ellerslie substation (orange) on November 4th, 2021.

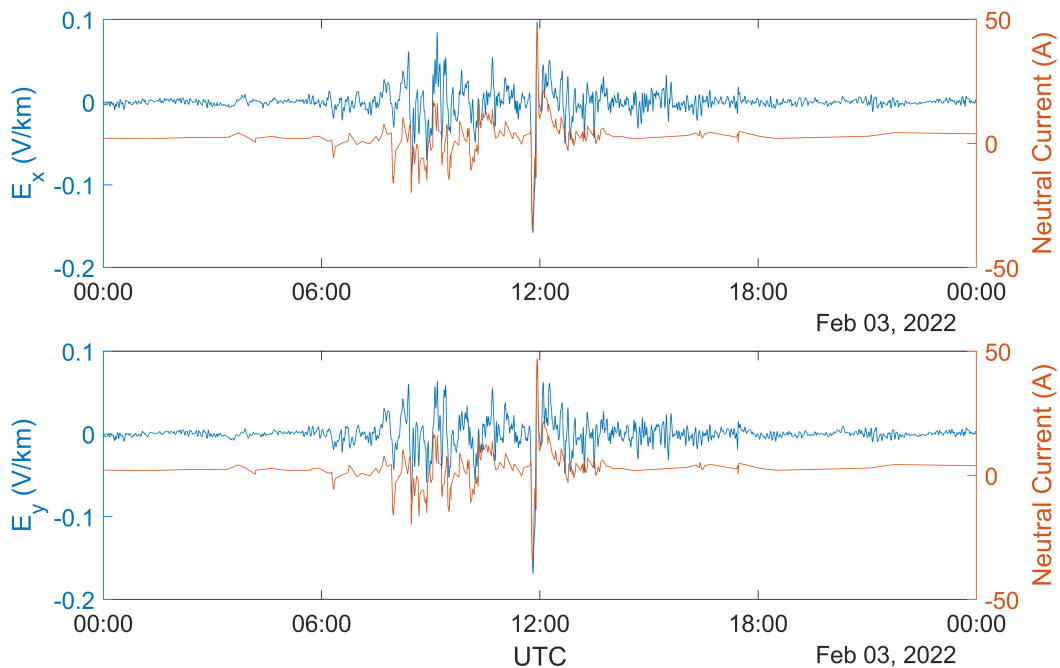


Figure 5.8: Comparison between the horizontal geoelectric field in V/km at MSTK magnetometer station (blue) and the transformer neutral-to-ground current in Amps at Ellerslie substation (orange) on February 3rd, 2022

For the October 12th event, the peak of the derived geoelectric field occurs at 10:54 UT with a value of  $-0.19$  V/km in the x component and  $-0.16$  V/km in the y component. The strongest GMD of the three events occurs on November 4th, 2021. During this particular event, the geoelectric field peak amplitude reaches  $0.27$  V/km and  $-0.43$  V/km in the x and y components, respectively. The neutral-to-ground current recorded  $80$  A on a single circuit, equivalent to approximately  $27$  A per phase. On February 3rd, 2022, the peak geoelectric field values are  $-0.16$  V/km and  $-0.17$  V/km in x and y, respectively. For all three cases, both the E-field and GIC time series show very strong correspondence in time and the waveform of both variations is very closely matched. Notably, the fluctuations of the neutral current closely match both small and large E-field variations. This is seen particularly well on November 4th at 5:30 - 6:00 UT and 12:15 - 12:45 UT. It is clear the calculated geoelectric field is directly related to the current flowing through the neutral-to-ground connection at the transformer substation. This is further verified quantitatively in the following section.

The largest differences between the measured GIC and the derived electric field occurs during times of largest geoelectric field variations, likely emphasizing the importance of the frequency dependence and the spatial scale of the GMD for driving GIC in the power line. The geoelectric field is calculated using GMD data measured approximately  $33$  km away from the transformer neutral-to-ground current measurement. The integration over the entire length of the power line may result in small spatial-scale elements of the geoelectric field inducing current in the power line not being seen the data at MSTK. Furthermore, the plane wave approximation adopted in the MT approach used to estimate E from B and Z (equations 5.2 - 5.4), may not be entirely valid during strong geomagnetic storms resulting in a discrepancy between the estimated E-field using the impedance matrix and the true electric field applied

to the power line (cf., *Campanyà et al.*, 2019, and references therein). As the neutral current and E-field match well in both horizontal components, it is evident that both provide a contribution to the potential across the length of the power line, and therefore to the GIC. In Subsection 5.3.3, an exercise in quantifying this relationship through correlation comparisons is done and an attempt to identify the role of each source component in driving GIC is completed.

### 5.3.3 Linear Correlation Comparison Between Geoelectric Field and GIC

Analysis in the previous subsection shows extremely clearly that space weather is driving GIC in the Alberta electrical power network. Here, we further quantify the relationship between the GMD and the resulting GIC on the Alberta power grid by looking at the correlation between each horizontal component of the geoelectric field as a function of time and the transformer neutral-to-ground current measured by AltaLink at the Ellerslie transformer substation. A moving average with a two minute sliding window is applied to both time series. The linear correlation coefficient is then determined for windows of two hour intervals on November 4th, 2021. From the three cases examined above, this event had high resolution data and, fortunately, the highest neutral-to-ground current amplitude compared to other very recent events.

Further, we investigate the neutral current’s correlation to an estimated combined E-field along a segment of the power line as defined by the geometric configuration of the N-S and E-W segments of the line from a region of approximately 60 km: where 74% is in the N-S direction associated with  $E_x$ , and 26% is in the E-W direction associated with  $E_y$  corresponding to power line lengths of 46.5 km and 16.5 km, respectively. The constant and relatively 1-D nature of the impedance tensor allows us to look at the combined

E-field as it should apply along this combination of two segments of the power line as there are no large or significant conductivity gradients in this region. This holds if we assume the geoelectric field is spatially uniform at each point along the power line.  $E_x$ ,  $E_y$ , and the combined E-field,  $0.74E_x - 0.26E_y$ , are plotted in Figure 5.9. The linear correlation between the transformer neutral-to-ground current and each of  $E_x$ ,  $E_y$ , and  $0.74E_x - 0.26E_y$  for the entire day of the November 4th, 2021 event are 0.563, 0.597, and 0.581, respectively. The linear correlations for two-hour intervals are shown in Figure 5.9.

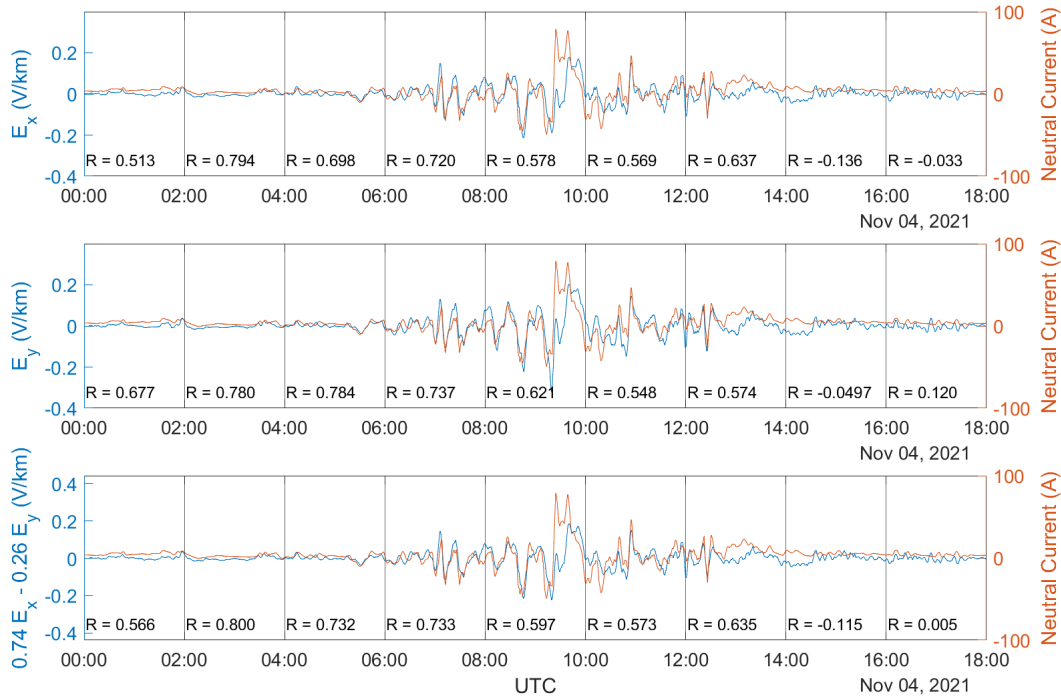


Figure 5.9: Quantitative comparison between the neutral current and the horizontal geoelectric field after a two minute moving average is applied: (top)  $E_x$ , (middle)  $E_y$ , (bottom) a combination of  $E_x$  and  $E_y$  based on the ratio of N-S and E-W elements of the power line. The linear correlation is found and stated for each 2 hour interval on November 4th, 2022.

For all three electric field time series the linear correlation is highest,  $R \gtrsim 0.7$ , and immediately before the very largest GIC and E-field fluctuations from 2:00 to 8:00 UTC. During periods of largest GIC, from 8:00 to 12:00 UTC, the correlation decreases slightly. The spatially uniform geoelec-

tric field assumption may not hold over the length of the power line, and any spatial variation in  $E$  during this period of large GMD could impact the correspondence of the time series, and therefore the correlation. This exercise of combining E-field components improves the correlation between times 2:00 to 4:00 UTC, and 10:00 to 12:00 UTC. To first approximation, this shows that considering the geometry of the power line may be necessary to properly estimate the GIC in the power line as a result of the geoelectric field which can drive current along both elements along the lengths of the power line in both the  $x$  and  $y$  directions. To do so, the E-field must be integrated along the whole of the power line to derive an accurate line potential difference which drives GIC. However, this requires knowing the E-field polarization and power line orientation at all points along the length of the line where the GIC is being driven. An approximation using a nearby E-field measurement is the best that can be done at this time due to the current spatial density of data available from local magnetometers. Regardless, an interpretation of the the dominant source of the GMD can be made from this comparative data analysis. An interesting result to note here is that there is no correlation near the end of the day from 14:00 to 18:00 UTC. There are small high-frequency variations in the E-field, but this does not lead to significant GIC being recorded by the Hall effect sensor. This is may be due to local GMD recorded at MSTK that does not occur across the entire length of the power line, 33 km to the North-West such that when these small scale electric fields are integrated along the line they do not produce significant line voltages which are needed to drive GIC. At this time, the geoelectric field varies within the range  $-20$  and  $20$  mV/km.

## 5.4 Conclusions

The contemporaneous and well correlated temporal signatures of the geoelectric field and the neutral-to-ground current with very similar waveform pre-

sented here are compelling proof of GMD causing GIC on the Alberta electrical power grid. We examined the spatial dependence of the impedance tensor magnitude and polarization on the calculated E-field across Alberta by plotting an impedance map, courtesy of Darcy Cordell, similar to that shown in *Love et al.* (2022) for the continental United States. The region around Edmonton where we have availability of both transformer neutral-to-ground current data from AltaLink and local GMD measurements with which to derive the geoelectric field data, there is a relatively constant and stable impedance tensor with no large conductivity gradients for which cause strongly polarized E-fields, This makes this an excellent region for examining the connection between the driving GMD and the resulting GIC in the power grid. This is relative uniformity of the impedance tensor is expected for a region of a sedimentary basin like that which covers the majority of Alberta. In the North-East portion of the province, where there the conductive Alberta Sedimentary Basin meets the resistive crystalline rock of the Canadian Shield, there are large values of strongly polarized impedance, as expected from *Cordell et al.* (2021), and which suggests these specific regions with large gradients in conductivity increases the likelihood of space weather hazards relating to GIC. We also examined the frequency dependence of the impedance tensor in the context of GIC risk, particularly for regions in central Alberta. As seen in Figure 5.4, the impedance remains small,  $-1.8 \times 10^{-3} < Z(\omega) < 2.1 \times 10^{-3}$  Ohms, in all components and for all frequencies in that region suggesting no frequency between  $10^{-4}$  and  $10^{-1}$  Hz significantly dominates, and that the region near Edmonton, Alberta has a smooth, relatively 1-D, impedance matrix. This implies that the frequencies of the derived electric field is dominated by the frequencies of the GMD.

This study then estimated the geoelectric field for three geomagnetic events during the past year, October 12th, 2021, November 4th, 2021, and February

3rd, 2022, and compared the calculated E-field derived from GMD data from the MSTK magnetometer station to the transformer neutral-to-ground current at the nearby transformer substation at Ellerslie. The three events have geomagnetic signatures of different magnitudes and temporal signatures; however, the transformer neutral-to-ground current measured on the power grid shows a very strong correspondence with the E-field for all three cases. The largest of the three events on November 4th, 2021, was caused by a moderate storm, but still generated an induced current of over 80 A in a single circuit, representing approximately 27 A per phase.

The linear correlation between the GIC measured by AltaLink and the derived geoelectric field is calculated on this day, where we also have high temporal resolution GIC data. For each of  $E_x$ ,  $E_y$ , and a combined E-field,  $0.74E_x - 0.26E_y$ , the correlation is highest, reaching values above  $R = 0.7$  around 2:00 to 8:00 UTC, immediately before the very largest GIC and E-field fluctuations seen on this day. The correlation decreases slightly for the hours of 8:00 to 12:00 UTC,  $R \sim 0.5 - 0.6$ , remains high during this time period of largest GIC. The assumption of a spatially uniform geoelectric field, and estimated from a single magnetometer station, may not apply over the entire length of the power line at this time. Further, only weak or no correlation is seen during the latter hours of the day, from 14:00 to 18:00 UTC. Small high-frequency variations in the E-field at this time do not generate GIC, which could be the result of a localized GMD at the MSTK magnetometer site, 33 km away, not being representative of the disturbances at all points along the power line. The E-field fluctuations, approximately  $\pm 20$  mV/km, during this period may also be too small to induce a significant current measurable by the Hall effect sensors as the power grid response, or they could have small spatial scales such that the integral of E does not result in a significant potential difference along the power line. Furthermore, the resistances of the

transformers, and the total resistance of the power line is unknown, but may play a role in inhibiting the GIC flow when  $E$  is small.

This study of recent geomagnetic events has clearly shown that the Alberta electrical power grid is impacted by GIC caused by small and moderate GMD events. By investigation the MT impedance tensors at regions in Alberta, particularly in central Alberta near Edmonton, we have examined the frequency and spatial dependence of the conductivity structure on inducing current in the electrical power system. By using the impedance tensor to calculate the geoelectric field we have shown through direct comparison the relationship between the driver electric fields and the grid GIC response during GMD events. We have shown that the calculated geoelectric field is demonstrably associated with GIC flowing through the transformer substation's ground connection, confirming that the measured neutral-to-ground current is GIC caused by GMD. We plan to use the higher resolution data provided by AltaLink for continued analysis of recent GMD events in future work.

# Chapter 6

## Conclusions and Future Work

### 6.1 Summary and Conclusions

This thesis was focused on the characterization and assessment of geomagnetically induced currents (GICs), with a view to future monitoring and assessment of their impacts. In Chapter 1, we reviewed the solar drivers of GICs and their generation in coupled geospace system and presented methods for estimating the geoelectric field using the magnetotelluric (MT) method. We briefly outlined the Sun-to-Earth processes causing GIC in grounded electrical transmission systems in the space weather chain. In Chapter 2, we continued with further background on the effects of GIC presenting examples of historical GIC events, and approaches for measuring GIC in electrical power networks, including the differential magnetometer measurement (DMM) method.

In Chapter 3, we presented the design and instrumentation for a new DMM method using a revised placement of sensors, and which was tested as a proof-of-concept in this thesis. The new DMM design is an expansion of the traditional DMM methods introduced by *Viljanen (2009)*, and developed and tested by *Matandirotya et al. (2016)* and *Hübert et al. (2020)*. We changed the placement of the second magnetometer to be closer to the power line such that it can also resolve the magnetic field produced by the GIC. The primary ben-

enefit of this new and novel approach is the ability to calculate two independent measurements of GIC derived from each of the magnetic field components in the y and z directions, perpendicular to the flow of GIC in the power line,  $I(\Delta B_y)$  and  $I(\Delta B_z)$ . The new measurement for the derivation of the DMM inferred GIC and the reconstruction of the clean driving geomagnetic disturbance (GMD) is also outlined in Chapter 3. Another benefit of the new DMM method is the simplification of data collection logistics and ease of deployment. The sources of uncertainties during the initial deployment are dominated by positional errors, specifically those resulting from the determination of the height of the power lines, and from the alignment, and stability of the alignment, of the sensors. Suggested upgrades to any future deployments include performing precise measurements for the power line heights above the DMM system, stabilizing the magnetometer orientation and deployment against the rotation due to soil heaving and or the freeze-thaw of dew close to or around the sensors, and integrating a solar panel and battery system for power supply and modem for data retrieval to reduce the frequency of site visits.

In Chapter 4, the DMM approach outlined in Chapter 3 is tested and validated by comparison with GIC data collected by a Hall effect sensor at the transformer neutral-to-ground connection deployed by AltaLink at the Ellerslie substation in the power line being monitored with our DMM system. We presented a comparative analysis from a geomagnetically quiet day on September 26th, 2021, which provided an assessment of the errors associated with the DMM method, and validated the cross-calibration between DMM sensors. Observations during a recent moderate geomagnetically storm on October 12th, 2021 showed excellent temporal correspondence between the Hall probe data at Ellerslie substation and the DMM inferred GIC. Contemporaneous peaks in both GIC measurements occur at 6:42 and 10:54 UT and are of the same magnitude. The GIC magnitude of the transformer neutral-to-ground mea-

surement reached 41 A in a single 3-phase circuit, while the DMM inferred GIC reached an estimate of 25 A in a single 3-phase circuit considering errors arising from the uncertainties in the relative distances between each sensor and the power lines and the misalignment between the sensors. The disagreement can be ascribed to positional errors introduced during deployment, and the unknown resistances in the power line and transformer ground connection. Regardless, this was also an improvement over previous studies (e.g., *Hübert et al.*, 2020) where a order of magnitude discrepancy existed between the two measurements. We were successful in demonstrating a proof of principle, using a prototype system in a temporary deployment of our new DMM method to measure local GIC on the electrical power grid. This could be used for temporary field assessment by the power industry, with opportunity to be expanded with upgrades as suggested in Section 3.5.

Lastly, in Chapter 5, a detailed analysis of the role of the local ground conductivity structure in the induction of geoelectric fields and therefore the generation of GICs on the Alberta electrical power grid was performed. Frequency and spatial variation of the impedance tensor amplitudes, shown in Figure 5.3, highlight the North-Eastern portion of the province of Alberta as an area of enhanced risk for GIC, supporting the results in *Cordell et al.* (2021). In central Alberta, the impedance tensor remains small and relatively constant, on the order of  $10^{-3}$  Ohms, over the frequency band of interest for GICs,  $10^{-4}$  to  $10^{-1}$  Hz. A comparative analysis between the geoelectric field and the transformer neutral-to-ground current during three recent geomagnetic events on October 12th, 2021, November 4th, 2021, and February 3rd, 2022, each with GMD of differing magnitudes and temporal signatures, showed excellent agreement with the simultaneous transformer neutral-to-ground measurement. The linear correlation over two hour intervals between each component of the E-field,  $E_x$  and  $E_y$ , and a combined E-field determined based on the power line geometry,

$0.74E_x - 0.26E_y$ , with the GIC Hall probe measurement reached values above 0.7 from 2:00 to 8:00 UT during a moderate geomagnetic storm on November 4th, 2021. It was evident that both small and moderate GMD produced GIC on the Alberta electrical power grid. Continued analysis of these and other events should be done in future work using the Hall probe data collected by AltaLink at other locations across the province including southern Alberta. An assessment of the regional variations in the geoelectric field could hence be investigated.

## 6.2 Future Work with Industry Partners

During this thesis, we have worked in close collaboration with AltaLink, one of Alberta's largest regulated electricity transmission companies. Through an informal partnership, AltaLink provided transformer neutral-to-ground data used for the validation of the DMM inferred GIC (Chapter 4) and comparison to the estimated geoelectric field (Chapter 5). In the near future, we will be seeking to pursue a formal partnership between academia (University of Alberta), industry (AltaLink, ATCO Electric), and the Alberta Electric Systems Operator (AESO), to study space weather impacts on the Alberta electrical power grid. Bringing together members from these organizations will be key in establishing continuous GIC data capture across the province of Alberta with appropriate scientific and engineering interpretation, with the goals of developing province-wide models of the electrical power network to understand its vulnerability to space weather events, and defining improved approaches to GIC mitigation and risk reduction. To do so, we will attempt to leverage grant support through academia-industry grant opportunities, such as the Natural Sciences and Engineering Research Council (NSERC) Alliance program.

Near-term goals will be to establish formal industry partnerships through

which we can provide assistance in meeting the regulatory requirements defined by the National Electric Reliability Corporation (NERC) in TPL-007 (*NERC*, 2020), and which we expect will be ultimately be implemented by the AESO in Alberta. These requirements include measuring and characterising GMD, monitoring and assessing GIC effects on the electrical grid, and validating the grid response through a high-fidelity model. The ultimate objective of future collaboration would be to expand this research as an operational service based on a validated model of the grid response. This would be used in developing data products for situational awareness, forecasting mitigation measures, and developing actionable protocols in the Alberta power grid with a view to the potential subsequent use in other provinces and jurisdictions later. Overall, the compelling results presented in this thesis have shown the particular benefit of utilizing transformer neutral-to-ground current data collected by industry in validating an improved DMM method to monitor GIC and characterize the grid GIC response due to driving geoelectric fields as a result of GMD. Importantly, our results provide excellent opportunities for continued and future academic-industry partnerships to mitigate the effects of space weather on the Alberta power grid.

# Bibliography

- Aschenbrenner, H., and G. Goubau (1936), Eine anordnung zur registrierung rascher magnetischer störungen, Hochfrequenztech, *Elektroakust*, 47(6), 177–181.
- Baumjohann, W., and R. A. Treumann (2012), *Basic Space Plasma Physics*, Imperial College Press, doi:10.1142/p015.
- Beamish, D., T. D. G. Clark, E. Clarke, and A. W. P. Thomson (2002), Geomagnetically induced currents in the UK: geomagnetic variations and surface electric fields, *Journal of Atmospheric and Solar-Terrestrial Physics*, 64(16), 1779–1792, doi:10.1016/s1364-6826(02)00127-x, publisher: Elsevier BV.
- Bedrosian, P. A., and J. J. Love (2015), Mapping geoelectric fields during magnetic storms: Synthetic analysis of empirical United States impedances, *Geophysical Research Letters*, 42(23), 10,160–10,170, doi:10.1002/2015GL066636.
- Beggan, C. D., G. S. Richardson, O. Baillie, J. Hübert, and A. W. P. Thomson (2021), Geoelectric field measurement, modelling and validation during geomagnetic storms in the UK, *Journal of Space Weather and Space Climate*, 11, 37, doi:10.1051/swsc/2021022.
- Belakhovsky, V., V. Pilipenko, M. Engebretson, Y. Sakharov, and V. Selivanov (2019), Impulsive disturbances of the geomagnetic field as a cause of induced currents of electric power lines, *Journal of Space Weather and Space Climate*, 9, A18, doi:10.1051/swsc/2019015.
- Berdichevsky, M. N., and V. I. Dmitriev (2008), *Models and methods of magnetotellurics*, Springer, New York.
- Bittencourt, J. A. (2004), *Fundamentals of plasma physics*, Springer Science & Business Media.
- Bolduc, L. (2002), GIC observations and studies in the Hydro-Québec power system, *Journal of Atmospheric and Solar-Terrestrial Physics*, 64(16), 1793–1802, doi:10.1016/S1364-6826(02)00128-1.
- Boteler, D. (1994), Geomagnetically induced currents: present knowledge and future research, *IEEE Transactions on Power Delivery*, 9(1), 50–58, doi:10.1109/61.277679.
- Boteler, D. H. (2001), Space Weather Effects on Power Systems, in *Space Weather*, pp. 347–352, American Geophysical Union (AGU).

- Boteler, D. H. (2019), A 21st Century View of the March 1989 Magnetic Storm, *Space Weather*, *17*(10), 1427–1441, doi:10.1029/2019SW002278.
- Boteler, D. H., and R. J. Pirjola (2017), Modeling geomagnetically induced currents, *Space Weather*, *15*(1), 258–276, doi:10.1002/2016SW001499.
- Boteler, D. H., R. J. Pirjola, and H. Nevanlinna (1998), The effects of geomagnetic disturbances on electrical systems at the Earth’s surface, *Advances in Space Research*, *22*(1), 17–27, doi:10.1016/s0273-1177(97)01096-x, publisher: Elsevier BV.
- Boteler, D. H., R. J. Pirjola, and L. Marti (2019), Analytic Calculation of Geoelectric Fields Due to Geomagnetic Disturbances: A Test Case, *IEEE Access*, *7*, 147,029–147,037, doi:10.1109/access.2019.2945530.
- Cagniard, L. (1953), BASIC THEORY OF THE MAGNETO-TELLURIC METHOD OF GEOPHYSICAL PROSPECTING, *GEOPHYSICS*, *18*(3), 605–635, doi:10.1190/1.1437915.
- Campanyà, J., P. T. Gallagher, S. P. Blake, M. Gibbs, D. Jackson, C. D. Beggan, G. S. Richardson, and C. Hogg (2019), Modeling Geoelectric Fields in Ireland and the UK for Space Weather Applications, *Space Weather*, *17*(2), 216–237, doi:10.1029/2018SW001999.
- Campbell, C. G. (2018), *Magnetohydrodynamics in Binary Stars*, *Astrophysics and Space Science Library*, vol. 456, Springer International Publishing, Cham.
- Chave, A. D., and A. G. Jones (2012), *The Magnetotelluric Method: Theory and Practice*, Cambridge University Press.
- Chisholm, W. A. (2018), Lightning Protection, in *Electric power generation, transmission, and distribution: The electric power engineering handbook*, edited by L. L. Grigsby, pp. 17–1, CRC Press.
- Cordell, D., M. J. Unsworth, B. Lee, C. Hanneson, D. K. Milling, and I. R. Mann (2021), Estimating the Geoelectric Field and Electric Power Transmission Line Voltage During a Geomagnetic Storm in Alberta, Canada Using Measured Magnetotelluric Impedance Data: The Influence of Three-Dimensional Electrical Structures in the Lithosphere, *Space Weather*, *19*(10), e2021SW002,803, doi:10.1029/2021SW002803.
- Cuttler, S. W., J. J. Love, and A. Swidinsky (2018), Geoelectric hazard assessment: the differences of geoelectric responses during magnetic storms within common physiographic zones, *Earth, Planets and Space*, *70*(1), 35, doi:10.1186/s40623-018-0807-7.
- Czech, P., S. Chano, H. Huynh, and A. Dutil (1992), The Hydro-Québec system blackout of 13 March 1989: system response to geomagnetic disturbances., in *Geomagnetically Induced Currents*, pp. 1–19.
- Dungey, J. W. (1961), Interplanetary Magnetic Field and the Auroral Zones, *Physical Review Letters*, *6*(2), 47–48, doi:10.1103/PhysRevLett.6.47.

- Eroshenko, E., A. Belov, D. Boteler, S. Gaidash, S. Lobkov, R. Pirjola, and L. Trichtchenko (2010), Effects of strong geomagnetic storms on Northern railways in Russia, *Advances in Space Research*, 46(9), 1102–1110, doi:10.1016/j.asr.2010.05.017.
- Fujita, S., R. Kataoka, I. Fujii, A. Pulkkinen, and S. Watari (2016), Extremely severe space weather and geomagnetically induced currents in regions with locally heterogeneous ground resistivity, *Earth, Planets and Space*, 68(1), 51, doi:10.1186/s40623-016-0428-y.
- Fukushima, N. (1976), Generalized theorem for no ground magnetic effect of vertical currents connected with Pedersen currents in the uniform-conductivity ionosphere, *Report of Ionosphere and Space Research in Japan*, 30, 35–40.
- Gaunt, C. T., and G. Coetzee (2007), Transformer failures in regions incorrectly considered to have low GIC-risk, in *2007 IEEE Lausanne Power Tech*, pp. 807–812, doi:10.1109/PCT.2007.4538419.
- Grigsby, L. L. (2007), *Electric Power Generation, Transmission, and Distribution*, CRC press, doi:10.1201/9781420009255.
- Hughes, W., and D. Southwood (1976), The screening of micropulsation signals by the atmosphere and ionosphere, *Journal of Geophysical Research*, 81(19), 3234–3240.
- Hübert, J., C. D. Beggan, G. S. Richardson, T. Martyn, and A. W. P. Thomson (2020), Differential Magnetometer Measurements of Geomagnetically Induced Currents in a Complex High Voltage Network, *Space Weather*, 18(4), e2019SW002421, doi:10.1029/2019SW002421.
- Kappenman, J. G. (2010), Low-Frequency Protection Concepts for the Electric Power Grid: Geomagnetically Induced Current (GIC) and E3 HEMP Mitigation John Kappenman, *R 322*, MetaTech, Goleta, CA.
- Kappenman, J. G. (2012), Geomagnetic Disturbances and Impacts upon Power System Operation, in *Electric Power Generation, Transmission, and Distribution: The Electric Power Engineering Handbook*, 3 ed., CRC Press.
- Kelly, G., A. Viljanen, C. Beggan, and A. Thomson (2017), Understanding GIC in the UK and French high-voltage transmission systems during severe magnetic storms, *Space Weather*, 15(1), 99–114, doi:10.1002/2016SW001469.
- Kivelson, M. G., and C. T. Russell (Eds.) (1995), *Introduction to Space Physics*, 1 ed., Cambridge University Press, doi:10.1017/9781139878296.
- Koskinen, H. E. J., and E. K. J. Kilpua (2022), *Physics of Earth's Radiation Belts: Theory and Observations*, Astronomy and Astrophysics Library, Springer International Publishing, Cham, doi:10.1007/978-3-030-82167-8.
- Krarti, M. (2018), Chapter 4 - Utility Rate Structures and Grid Integration, in *Optimal Design and Retrofit of Energy Efficient Buildings, Communities, and Urban Centers*, edited by M. Krarti, pp. 189–245, Butterworth-Heinemann.

- Lanza, R., and A. Meloni (2006), The Earth's Magnetic Field, in *The Earth's Magnetism: An Introduction for Geologists*, pp. 1–66, Springer Berlin Heidelberg, Berlin, Heidelberg.
- Le, G., J. A. Slavin, and R. J. Strangeway (2010), Space Technology 5 observations of the imbalance of regions 1 and 2 field-aligned currents and its implication to the cross-polar cap Pedersen currents, *Journal of Geophysical Research: Space Physics*, *115*(A7), doi:10.1029/2009ja014979.
- Liu, C.-M., L.-G. Liu, and R. Pirjola (2009), Geomagnetically Induced Currents in the High-Voltage Power Grid in China, *IEEE Transactions on Power Delivery*, *24*(4), 2368–2374, doi:10.1109/TPWRD.2009.2028490.
- Love, J. J., G. M. Lucas, E. J. Rigler, B. S. Murphy, A. Kelbert, and P. A. Bedrosian (2022), Mapping a Magnetic Superstorm: March 1989 Geoelectric Hazards and Impacts on United States Power Systems, *Space Weather*, *20*(5), e2021SW003,030, doi:10.1029/2021SW003030.
- Lu, S., Y. Liu, and J. De La Ree (1993), Harmonics generated from a DC biased transformer, *IEEE Transactions on Power Delivery*, *8*(2), 725–731, doi:10.1109/61.216881.
- Lundstedt, H. (2006), The sun, space weather and GIC effects in Sweden, *Advances in Space Research*, *37*(6), 1182–1191, doi:10.1016/j.asr.2005.10.023.
- Mac Manus, D. H., C. J. Rodger, M. Dalzell, A. W. P. Thomson, M. A. Clilverd, T. Petersen, M. M. Wolf, N. R. Thomson, and T. Divett (2017), Long-term geomagnetically induced current observations in New Zealand: Earth return corrections and geomagnetic field driver: Long-Term GIC Observation in New Zealand, *Space Weather*, *15*(8), 1020–1038, doi:10.1002/2017SW001635.
- Mann, I. R., D. K. Milling, I. J. Rae, L. G. Ozeke, A. Kale, Z. C. Kale, K. R. Murphy, A. Parent, M. Usanova, D. M. Pahud, E.-A. Lee, V. Amalraj, D. D. Wallis, V. Angelopoulos, K.-H. Glassmeier, C. T. Russell, H.-U. Auster, and H. J. Singer (2008), The Upgraded CARISMA Magnetometer Array in the THEMIS Era, *Space Science Reviews*, *141*(1), 413–451, doi:10.1007/s11214-008-9457-6.
- Marshall, R. A., M. Dalzell, C. L. Waters, P. Goldthorpe, and E. A. Smith (2012), Geomagnetically induced currents in the New Zealand power network, *Space Weather*, *10*(8), doi:10.1029/2012SW000806.
- Marshall, R. A., H. Gorniak, T. Van Der Walt, C. L. Waters, M. D. Sciffer, M. Miller, M. Dalzell, T. Daly, G. Pouferis, G. Hesse, and P. Wilkinson (2013), Observations of geomagnetically induced currents in the Australian power network, *Space Weather*, *11*(1), 6–16, doi:10.1029/2012SW000849.
- Marshall, R. A., L. Wang, G. A. Paskos, G. Olivares-Pulido, T. V. D. Walt, C. Ong, D. Mikkelsen, G. Hesse, B. McMahon, E. V. Wyk, G. Ivanovich, D. Spoor, C. Taylor, and A. Yoshikawa (2019), Modeling Geomagnetically Induced Currents in Australian Power Networks Using Different Conductivity Models, *Space Weather*, *17*(5), 727–756, doi:https://doi.org/10.1029/2018SW002047.

- Matandirotya, E., P. J. Cilliers, R. R. Van Zyl, D. T. Oyedokun, and J. de Villiers (2016), Differential magnetometer method applied to measurement of geomagnetically induced currents in Southern African power networks, *Space Weather*, *14*(3), 221–232, doi:10.1002/2015SW001289.
- McKay, A., and K. Whaler (2006), The electric field in northern England and southern Scotland: implications for geomagnetically induced currents, *Geophysical Journal International*, *167*(2), 613–625, doi:10.1111/j.1365-246X.2006.03128.x.
- McPherron, R. L. (1979), Magnetospheric substorms, *Reviews of Geophysics*, *17*(4), 657–681, doi:10.1029/RG017i004p00657.
- Molinski, T. S. (2002), Why utilities respect geomagnetically induced currents, *Journal of Atmospheric and Solar-Terrestrial Physics*, *64*(16), 1765–1778, doi:10.1016/S1364-6826(02)00126-8.
- Myllys, M., A. Viljanen, O. A. Rui, and T. M. Ohnstad (2014), Geomagnetically induced currents in Norway: the northernmost high-voltage power grid in the world, *Journal of Space Weather and Space Climate*, *4*, A10, doi:10.1051/swsc/2014007.
- Naidu, G. D. (2012), Magnetotellurics: Basic Theoretical Concepts, in *Deep Crustal Structure of the Son-Narmada-Tapti Lineament, Central India*, edited by G. D. Naidu, Springer Theses, pp. 13–35, Springer, Berlin, Heidelberg.
- NERC (2020), Transmission System Planned Performance for Geomagnetic Disturbance Events, *Tech. Rep. TPL-007-4*, North American Electric Reliability Corporation.
- Nikitina, L., L. Trichtchenko, and D. H. Boteler (2016), Assessment of extreme values in geomagnetic and geoelectric field variations for Canada: GEOMAGNETIC EXTREMES IN CANADA, *Space Weather*, *14*(7), 481–494, doi:10.1002/2016SW001386.
- Parker, E. (1959), Extension of the solar corona into interplanetary space, *Journal of Geophysical Research (1896-1977)*, *64*(11), 1675–1681, doi:10.1029/JZ064i011p01675.
- Parker, E. N. (1979), Sunspots and the physics of magnetic flux tubes. IX - Umbral dots and longitudinal overstability, *The Astrophysical Journal*, *234*, 333, doi:10.1086/157501.
- Pirjola, R. (2000), Geomagnetically induced currents during magnetic storms, *IEEE Transactions on Plasma Science*, *28*(6), 1867–1873, doi:10.1109/27.902215.
- Pirjola, R. (2002), Review On The Calculation Of Surface Electric And Magnetic Fields And Of Geomagnetically Induced Currents In Ground-Based Technological Systems, *Surveys in Geophysics*, *23*(1), 71–90, doi:10.1023/A:1014816009303.
- Pirjola, R., and A. Viljanen (1998), Complex image method for calculating electric and magnetic fields produced by an auroral electrojet of finite length, *Annales Geophysicae*, *16*(11), 1434–1444, doi:10.1007/s00585-998-1434-6.

- Pirjola, R., D. Boteler, A. Viljanen, and O. Amm (2000), Prediction of geomagnetically induced currents in power transmission systems, *Advances in Space Research*, 26(1), 5–14, doi:10.1016/s0273-1177(99)01019-4, publisher: Elsevier BV.
- Pirjola, R., A. Pulkkinen, and A. Viljanen (2003), Studies of space weather effects on the finnish natural gas pipeline and on the finnish high-voltage power system, *Advances in Space Research*, 31(4), 795–805, doi:10.1016/S0273-1177(02)00781-0.
- Pirjola, R., A. Viljanen, A. Pulkkinen, S. Kilpua, and O. Amm (2005), Ground Effects of Space Weather, in *Effects of Space Weather on Technology Infrastructure*, edited by I. A. Daglis, pp. 235–256, Springer Netherlands, Dordrecht.
- Price, P. (2002), Geomagnetically induced current effects on transformers, *IEEE Transactions on Power Delivery*, 17(4), 1002–1008, doi:10.1109/TPWRD.2002.803710.
- Primdahl, F. (1979), The fluxgate magnetometer, *Journal of Physics E: Scientific Instruments*, 12(4), 241–253, doi:10.1088/0022-3735/12/4/001.
- Pulkkinen, A., A. Thomson, E. Clarke, and A. McKay (2003), April 2000 geomagnetic storm: ionospheric drivers of large geomagnetically induced currents, *Annales Geophysicae*, 21(3), 709–717, doi:10.5194/angeo-21-709-2003.
- Pulkkinen, A., S. Lindahl, A. Viljanen, and R. Pirjola (2005), Geomagnetic storm of 29–31 October 2003: Geomagnetically induced currents and their relation to problems in the Swedish high-voltage power transmission system, *Space Weather*, 3(8), doi:https://doi.org/10.1029/2004SW000123.
- Pulkkinen, A., E. Bernabeu, A. Thomson, A. Viljanen, R. Pirjola, D. Boteler, J. Eichner, P. J. Cilliers, D. Welling, N. P. Savani, R. S. Weigel, J. J. Love, C. Balch, C. M. Ngwira, G. Crowley, A. Schultz, R. Kataoka, B. Anderson, D. Fugate, J. J. Simpson, and M. MacAlester (2017), Geomagnetically induced currents: Science, engineering, and applications readiness, *Space Weather*, 15(7), 828–856, doi:10.1002/2016SW001501.
- Rajput, V. N., D. H. Boteler, N. Rana, M. Saiyed, S. Anjana, and M. Shah (2021), Insight into impact of geomagnetically induced currents on power systems: Overview, challenges and mitigation, *Electric Power Systems Research*, 192, 106,927, doi:10.1016/j.epsr.2020.106927.
- Schrijver, C. J., R. Dobbins, W. Murtagh, and S. M. Petrinec (2014), Assessing the impact of space weather on the electric power grid based on insurance claims for industrial electrical equipment, *Space Weather*, 12(7), 487–498, doi:10.1002/2014SW001066.
- Simpson, F., and K. Bahr (2005), *Practical magnetotellurics*, Cambridge University Press, doi:10.1017/CBO9780511614095.
- Snare, R. C. (1998), A history of vector magnetometry in space, *GEOPHYSICAL MONOGRAPH-AMERICAN GEOPHYSICAL UNION*, 103, 101–114, doi:10.1002/9781118664391.ch12.

- Sokolova, E. Y., O. V. Kozyreva, V. A. Pilipenko, Y. A. Sakharov, and D. V. Epishkin (2019), Space-Weather-Driven Geomagnetic- and Telluric-Field Variability in Northwestern Russia in Correlation with Geoelectrical Structure and Currents Induced in Electric-Power Grids, *Izvestiya, Atmospheric and Oceanic Physics*, 55(11), 1639–1658, doi:10.1134/S0001433819111015X.
- Stauning, P. (2001), High-Voltage Power Grid Disturbances During Geomagnetic Storms, in *Proceedings of the Second Solar Cycle and Space Weather Euroconference*, vol. SP-477, pp. 521–524, European Space Agency, Vico Equense, Italy.
- Torta, J. M., A. Marcuello, J. Campanyà, S. Marsal, P. Queralt, and J. Ledo (2017), Improving the modeling of geomagnetically induced currents in Spain: Improving the Modeling of GIC, *Space Weather*, 15(5), 691–703, doi:10.1002/2017SW001628.
- Trichtchenko, L., A. Zhukov, R. van der Linden, S. M. Stankov, N. Jakowski, I. Stanisławska, G. Juchnikowski, P. Wilkinson, G. Patterson, and A. W. P. Thomson (2007), November 2004 space weather events: Real-time observations and forecasts: NOVEMBER 2004 EVENTS, *Space Weather*, 5(6), n/a–n/a, doi:10.1029/2006SW000281.
- Vasseur, G., and P. Weidelt (1977), Bimodal electromagnetic induction in non-uniform thin sheets with an application to the northern Pyrenean induction anomaly, *Geophysical Journal International*, 51(3), 669–690, doi:10.1111/j.1365-246X.1977.tb04213.x.
- Viljanen, A. (2009), Measurements of geomagnetically induced currents by using two magnetometers, in *8-th International Symposium on Electromagnetic Compatibility and Electromagnetic Ecology*, pp. 16–19, St. Petersburg, Russia.
- Viljanen, A., O. Amm, and R. Pirjola (1999), Modeling geomagnetically induced currents during different ionospheric situations, *Journal of Geophysical Research: Space Physics*, 104(A12), 28,059–28,071, doi:10.1029/1999JA900337.
- Viljanen, A., E. I. Tanskanen, and A. Pulkkinen (2006), Relation between sub-storm characteristics and rapid temporal variations of the ground magnetic field, *Annales Geophysicae*, 24(2), 725–733, doi:10.5194/angeo-24-725-2006.
- Wait, J. R. (1962), Theory of magnetotelluric fields, *Journal of Research of the National Bureau of Standards, Section D: Radio Propagation*, 66D(5), 509, doi:10.6028/jres.066D.052.
- Wang, D., Y. Li, P. Dehghanian, and S. Wang (2019), Power Grid Resilience to Electromagnetic Pulse (EMP) Disturbances: A Literature Review, in *2019 North American Power Symposium (NAPS)*, pp. 1–6, doi:10.1109/NAPS46351.2019.9000227.
- Wik, M., A. Viljanen, R. Pirjola, A. Pulkkinen, P. Wintoft, and H. Lundstedt (2008), Calculation of geomagnetically induced currents in the 400 kV power grid in southern Sweden, *Space Weather*, 6(7), doi:10.1029/2007SW000343.

- Zhang, J. J., C. Wang, T. R. Sun, and Y. D. Liu (2016), Risk assessment of the extreme interplanetary shock of 23 July 2012 on low-latitude power networks, *Space Weather*, *14*(3), 259–270, doi:10.1002/2015SW001347.
- Zheng, K., L. Trichtchenko, R. Pirjola, and L.-G. Liu (2013), Effects of Geophysical Parameters on GIC Illustrated by Benchmark Network Modeling, *IEEE Transactions on Power Delivery*, *28*(2), 1183–1191, doi:10.1109/TPWRD.2013.2249119.
- Zheng, K., D. Boteler, R. J. Pirjola, L.-g. Liu, R. Becker, L. Marti, S. Boutilier, and S. Guillon (2014), Effects of System Characteristics on Geomagnetically Induced Currents, *IEEE Transactions on Power Delivery*, *29*(2), 890–898, doi:10.1109/TPWRD.2013.2281191.